Kinetic and Structural Insights into the Growth of Two-Dimensional Conjugated Polymers with Scanning Probe Microscopy

By
Simon Wolfgang Briesenick
Department of Physics,
McGill University, Montreal

A thesis submitted to McGill University in partial fulfillment of the requirements of the degree of
Master of Science

Supervisor	Peter Grütter Department of Physics McGill University
Internal Examiner	Bradley Siwick Department of Physics McGill University

November 2024

Für meine Eltern Pia, Claus, und Andrea.

Chance favors the prepared mind.
- Louis Pasteur

Scan, when you can.
- The author

Contents

1 Introduction **1**

2 Two-Dimensional Conjugated Polymers via Ullmann Coupling **3**

2.1 Introduction 3

2.2 Synthesis 4

2.2.1 General Concepts in On-Surface Polymerization 4

2.2.2 Surface-assisted Ullmann Coupling 7

2.2.3 Insulating Substrates 12

2.3 Applications 15

2.4 Conclusion 16

3 Theory and Experimental Methods **17**

3.1 Scanning Tunneling Microscopy (STM) 17

3.1.1 Basic Principle 18

3.1.2 Tip Preparation and Calibration 19

3.2 Non-Contact Atomic Force Microscopy (ncAFM) 22

3.2.1 Basic Principle 22

3.2.2 The qPlus Sensor 23

3.2.3 CO-terminated Studies 23

3.3 Low Energy Electron Diffraction (LEED) and Auger Electron Spectroscopy (AES) 27

3.3.1 LEED 27

3.3.2 Auger electron spectroscopy (AES) 27

3.4 Sample Preparation and Synthesis of 2D Polymers 28

3.5 Precursors Investigated 30

4 Elucidating Reaction Kinetics and Edge Chemistry of 2D Polymers **31**

4.1 A Kinetic Monte Carlo Model to Simulate Polymer Synthesis in Two Dimensions . 31

4.1.1 Model Description 33

4.1.2 Network Quality Dependence on Energetic Barriers 35

4.1.3 Conclusion 38

4.2 The Role of Edge Terminations of Active 2D Polymers 39

4.2.1 CO-terminated Measurements 40

4.2.2 Comparison with Density Functional Theory (DFT) 44

4.2.3 Conclusion 49

4.3 Lateral P^2(TANG-TANGO) Heterojunctions 51

5 Conclusion and Outlook **55**

A Au$(1\,1\,1)$ Kink Sites as Nucleation Sites for 2DCPs and Observation of new Surface Reconstruction **58**

B The Wasserstein Metric of Two Discrete Distributions **61**

List of Figures

2.1 Step Edges as nucleation sites. 5
2.2 Reaction pathway on different coinage metal surfaces. 9
2.3 Network Quality Dependence on Diffusion and Coupling. 11
2.4 Porphyrin precursors with one, two, or four bromine substituents. 12
2.5 Halogen Substitution Pattern Determines Topology of Covalent Networks. 13
2.6 Electronic decoupling approach via deliberate iodination. 14

3.1 UHV system utilized in this thesis. 18
3.2 SPM studies of a single pentacene molecule on a NaCl/Cu(1 1 1) island. 20
3.3 Sensors used in this work. 20
3.4 STM Tip Conditioning. 21
3.5 Amplitude and phase characteristic for a standard qPlus sensor at 10K. 24
3.6 Time trace of the z-piezo extension during controlled CO pickup. 26
3.7 STM scans of CO molecules on Cu(1 1 1) with CO-decorated tip. 27
3.8 Typical low energy electron diffractogram recorded after sputter-annealing a Cu(1 1 1) single crystal. 28
3.9 Three-dimensional render of STM scan of Au(1 1 1) after ion bombardment without the subsequent annealing step. 29
3.10 Brominated three-fold symmetric precursors TBTANG and TBTANGO polymerize into networks with hexagonal pores. 30

4.1 Kinetic Transitions in the kMC Model. 34
4.2 Interplay between Diffusion and Coupling in the Quality of the 2D Networks. . . . 36
4.3 Workflow to Extract Network Quality from Experimental STM Images. 37
4.4 2D Contours of the Wasserstein matrix for different slices of the rotational energy barrier. 38

4.5 Organometallic Intermediary Formation on Cu $(1\,1\,1)$. 40
4.6 P^2(TANG)/Au$(1\,1\,1)$ Contrast Formation as a function of tip-sample separation. . . 41
4.7 Statistical analysis of molecular bond lengths based on 273 measurements from 20 STM images. 42
4.8 Highly defective region of P^2(TANG)/Au$(1\,1\,1)$. 43
4.9 DFT Optimized Geometries for two potential candidates of the TES termination identity. 45
4.10 Potential identities of terminations of TES. 46
4.11 Comparison between experimental and simulated contrast of TES for Br-terminated TANG. 48
4.12 Quantitative agreement between experimental FES Δf maps to gas phase hydrogenated TANG molecules. 49
4.13 Comparison between simulated and experimental contrast of Br/Au$(1\,1\,1)$ system. . 50
4.14 Interactions between partially dehalogenated P^2(TANG) cluster and partially dehalogenated single molecule might reduce the coupling rate and enhance network quality. 51
4.15 Idealized schematic of core-shell geometry of 2D block copolymer via sequential exposure of the surface to molecularly isostructural precursors. 52
4.16 P^2(TANG-TANGO) Heterojunctions. 54

A.1 Object classification analysis of ~ 0.4 ML P^2(TANG) islands on Au$(1\,1\,1)$ using ilastik. 59

List of Tables

3.1 Simplified parameters for a three-cycle sputter-anneal process. The sputtering current collected by the whole sample plate assembly was kept constant at $\approx 4\ \mu$A. 29

4.1 Overview of Properties of Monopolymer P^2(TANG) and P^2(TANGO) on Au(1 1 1). 53

List of Abbreviations

0D, 1D, 2D Zero-, One-, Two-Dimensional

2DCBC Two-Dimensional pi-conjugated Block Copolymer

2DCP Two-Dimensional pi-conjugated Polymer

DFT Density Functional Theory

FES/TES Featureless Edge State/Terminated Edge State

kMC/MC Kinetic Monte Carlo/Monte Carlo

LDOS/DOS Local Density of States/Density of States

LEED Low Energy Electron Diffraction

ML Monolayer

ncAFM Non-contact Atomic Force Microscopy

OM Organometallic

ppafm Probe-particle Atomic Force Microscopy

P^2(TANG)/P^2(TANGO) Poly(trioxaazatriangulene)/Poly(trioxoazatriangulene)

SPM Scanning Probe Microscopy

STM Scanning Tunneling Microscopy

STS Scanning Tunneling Spectroscopy

TBTANG/TBTANGO Tribromotrioxaazatriangulene/Tribromotrioxoazatriangulene

UHV Ultra-high Vacuum

Abstract

One of the holy grails of nanoscience is the realization of electronic devices, only a few atomic layers thick. Graphene presents a promising candidate for the continued miniaturization demands of the semiconductor industry for its exceptional optoelectronic properties. However, its lack of an intrinsic electronic bandgap has limited the use in semiconductor applications, where precise control over electronic properties is essential. While various strategies, such as heterostructuring and chemical doping, have been explored to induce a bandgap in graphene, achieving uniformity and scalability remains a significant challenge.

2D conjugated polymers (2DCPs) are a novel class of materials that offer an alternative approach through the bottom-up synthesis of ordered 2D networks from single-molecule precursors. Unlike other approaches to tune the properties of graphene through the introduction of heteroatom dopants post-synthesis, the precursors can be designed to lead to nanoarchitectures with *a priori* defined properties. In particular, the on-surface synthesis of 2DCPs via Ullmann coupling reactions represents a widespread approach, as the presence of a confining surface naturally steers the dimensionality of the structures, all the while actively participating in the polymerization reaction through adatom donation, catalytic activity, and templating, among others.

This thesis explores the on-surface synthesis of 2DCPs via Ullmann coupling on coinage metal substrates and investigates their structure and growth mechanisms using scanning probe microscopy techniques, including scanning tunneling microscopy (STM) and non-contact atomic force microscopy (ncAFM). Kinetic Monte Carlo (kMC) simulations and High-resolution imaging with CO-terminated tips, supported by density functional theoretical (DFT) calculations, provides mechanistic insights into the polymerization process.

A particular focus is placed on understanding the chemical state of live edges of 2D trioxa azatriangulene (P^2TANG) polymers synthesized on Au(1 1 1). Experimental observations reveal that only a small number of monomers forming the grain boundary of oligomers have undergone complete dehalogenation. Possible explanations and mechanistic insights are extracted from this unexpected finding. Furthermore, a simple kMC model to simulate the synthesis of 2D covalent nanostructures was developed. By systematically varying the transitional energetic barriers as-

sociated with diffusion, rotation, and coupling of individual monomers, the model successfully replicated experimentally observed network structures, and hints at the possibility to qualitatively assess the magnitude of the transitional energy barriers from STM images. Lastly, the hetero-polymerization of trioxo-azatriangulene with trioxa-azatriangulene into 2D copolymer structures is surveyed, and an efficient method for differentiating between the isostructural building blocks using local density of states (LDOS) mapping presented.

Résumé

L'un des objectifs majeurs de la nanoscience est la réalisation de dispositifs électroniques ne mesurant que quelques couches atomiques d'épaisseur. Le graphène représente un candidat prometteur pour répondre aux exigences de miniaturisation de l'industrie des semi-conducteurs, grâce à ses propriétés optoélectroniques exceptionnelles. Cependant, l'absence de bande interdite intrinsèque limite son utilisation dans les applications électroniques, où un contrôle précis des propriétés électroniques est essentiel. Bien que diverses stratégies, telles que l'hétérostructuration et le dopage chimique, aient été explorées pour induire une bande interdite dans le graphène, obtenir une uniformité et une évolutivité demeure un défi majeur.

Les polymères conjugués bidimensionnels (2DCPs) constituent une classe de matériaux innovante qui offre une approche alternative grâce à la synthèse ascendante de réseaux 2D ordonnés à partir de précurseurs moléculaires uniques. Contrairement aux approches visant à modifier les propriétés du graphène par l'introduction de dopants hétéroatomiques après synthèse, les précurseurs peuvent être conçus pour conduire à des nano-architectures aux propriétés définies *a priori*. En particulier, la synthèse de 2DCPs sur surface via les réactions de couplage d'Ullmann représente une approche largement utilisée, car la surface confinante oriente naturellement la dimensionnalité des structures tout en participant activement à la réaction de polymérisation par le don d'adatomes, l'activité catalytique, le rôle de gabarit, entre autres.

Cette thèse explore la synthèse sur surface de 2DCPs via le couplage d'Ullmann sur des substrats métalliques nobles et étudie leur structure ainsi que leurs mécanismes de croissance à l'aide de techniques de microscopie à sonde locale, incluant la microscopie à effet tunnel (STM) et la microscopie à force atomique en mode non-contact (ncAFM). Des simulations cinétiques Monte Carlo (kMC) et des images haute résolution obtenues avec des pointes terminées par des molécules de CO, soutenues par des calculs de théorie de la fonctionnelle de la densité (DFT), fournissent des informations mécanistiques sur le processus de polymérisation.

Un intérêt particulier est porté à l'état chimique des bords vivants des polymères trioxa-azatriangulène (P^2TANG) synthétisés sur Au(1 1 1). Les observations expérimentales révèlent qu'un petit nombre de monomères formant la limite de grain des oligomères ont subi une déshalogénation complète.

Des explications possibles et des informations mécanistiques sont extraites de cette découverte inattendue. De plus, un modèle kMC simple pour simuler la synthèse de nanostructures covalentes 2D a été développé. En faisant varier systématiquement les barrières énergétiques de transition associées à la diffusion, à la rotation et au couplage des monomères individuels, le modèle a réussi à reproduire les structures de réseaux observées expérimentalement et suggère la possibilité d'évaluer qualitativement l'amplitude des barrières énergétiques de transition à partir des images STM. Enfin, l'hétéro-polymérisation du trioxo-azatriangulène avec le trioxa-azatriangulène dans des structures copolymères 2D est étudiée, et une méthode efficace pour différencier les blocs constitutifs isostructuraux en utilisant la cartographie de densité d'états locaux (LDOS) est présentée.

Acknowledgements

Few people get the chance to spend their days immersed in science without worrying about finances, and I feel incredibly lucky and grateful to the Canadian taxpayers for making this journey possible.

- Peter, thank you for being such a fantastic supervisor. Your insights and wisdom have guided me through research and beyond, and I've always felt encouraged to chase my own ideas. I couldn't have asked for a better mentor and example.

- Wyatt, you've been an incredible mentor and friend. We've spent so many hours in the lab – discussing measurements, troubleshooting, and just keeping each other sane. If there's one thing you've truly taught me, it's not to be *hasty* – a lesson I'll carry with me. This thesis would not have been possible without your help.

- I'm grateful to Dima Perepichka for providing the molecules that made this project possible. Working with you as a collaborator has been a privilege, and I've always felt taken seriously and respected.

- Many people in the broader science community have offered guidance and help along the way. Special thanks to Nata and Nick from the Grutter group, Pascal and Marc from the Machine Shop, Brandon, John Smeros, Juan Gallego, and Robert Gagnon from the Physics Department, as well as Gianluca Galeotti and Sarah Burke, whose expertise in surface science helped me tremendously. Thanks to Ruben Perez, Pablo Pou Bell, and Manuel Lastre, who we recently started collaborating with. I would like to thank Valentina (Cooke Lab), and Shuaishuai (Guo Group) for supporting me with my DFT calculations. Thanks also to Bradley Siwick, who agreed to be my external examiner.

- Finally, to my family, and my friends, here and abroad – thank you for being there every step of the way. My partner, Renée, has been a constant source of encouragement. Adam, *Christien*, and Rodrigo made Montreal feel like home with their humor, friendship, and memorable hangouts. And to Hasan and Niklas, two lifelong friends back home who've

been there for me in difficult times. Homesickness, I've realized, is more about missing people than places, and you two remind me of that often. My intramural football team friends, though we never won anything. But it was always the refs fault.

Chapter 1

Introduction

Prior to the experimental isolation of single layer graphene in 2004 by Novoselov and Geim [1], the scientific consensus was that strictly two-dimensional (2D) atomic crystals were unstable at finite temperatures. This belief was largely based on the Mermin-Wagner theorem, which states that long-range order in low dimensional ($d \leq 2$) systems cannot exist at $T > 0$ K due to thermal fluctuations driving the system towards a state of increased entropy [2, 3]. While the underlying physical phenomena are very different, the coiling of headphone cables in one's pocket can be seen as an everyday classical analogue for the 1D case. However, the isolation of graphene does not contradict the Mermin-Wagner theorem. In 2007, again by the group of Geim and Novoselov, freely suspended graphene crystals could be shown to exhibit elastic deformations into the third dimension on the order of 1 nm [4]. When supported by a substrate, however, interfacial bonding reduces the thermal instability, thus highlighting the need for on-surface polymerization, as compared to solution-based approaches [5].

Shortly after the Nobel Prize winning discovery of graphene, interest in other 2D materials surged for their massive range of properties ranging from the extremely insulating to the exceedingly conductive, from the stiffest to the softest. Transition metal dichalcogenides (TMDs), hexagonal boron nitride (h-BN), as well as 2D polymers, are just some of the members of the ever-growing family of two-dimensional materials. It follows that 2D heterostructures of two or more different layers of such materials offer even greater tunability for designing novel devices. The first designs have started to appear little over a decade ago with very promising characteristics, such as a graphene-based field effect tunneling transistor [6, 7, 8].

The remarkable electronic properties of graphene are owed to its fully π-conjugated network, which gives rise to ballistic (i.e. weakly interacting with lattice) [9] and viscous (strongly electron-electron correlated) [10] charge transport with measured room-temperature mobilities close to $\mu = 250{,}000$ cm^2 (Vs)$^{-1}$ [9], two orders of magnitude larger than in intrinsic Si ($\mu \leq 1{,}400$

$\mathrm{cm}^2\,(\mathrm{Vs})^{-1}$). While graphene has been termed a "miracle material" for it's extraordinary properties, some issues in it's incorporation into functional devices persist. The largest obstacle for graphene is the absence of a bandgap and lack of control over the Fermi level, which makes the material unusable in most semiconductor applications, where electronic bandgaps and Fermi levels can be fine tuned through e.g. controllable introduction of dopants into the bulk structure, thereby vastly changing the properties of the product. Interestingly, the first workaround for this issue was reported in 2002 even before the work of Novoselov and Geim, where it was found that a h-BN/Ni$(1\,1\,1)$ substrate to a graphene top layer led to a band gap opening of 500 meV [11]. Another approach is chemical substitution doping which is conceptually similar to semiconductor doping, but uniformly doping large areas has so far proven difficult [12]. 2D π-conjugated polymers (2DCP), are atomically thin, organic polymers that could mitigate this issue [13]. This is because the overall properties are determined by the used monomer and can thus easily be tuned to fit a wide range of technological applications. There are several synthesis pathways to obtain such polymers, but by far the most common is *Ullmann coupling*. This reaction consists of two steps that make use of the catalytic activity of the underlying transition metal substrate, to (i) dehalogenate aryl halide precursors, and (ii) subsequently couple the radicals into polymers [14].

Despite significant progress in the synthesis of 2D networks via surface-assisted Ullmann coupling, they remain a victim of high defect densities, hindering their technological application. Particularly the interplay of the fundamental building block with the substrate, and with other oligomers remains inadequately understood. This research is focused on addressing these questions, both from an experimental point of view by utilizing Scanning Tunneling Microscopy (STM), and non-contact Atomic Force Microscopy (ncAFM), as well as from a theoretical perspective via Density Functional Theory (DFT), and kinetic Monte Carlo (kMC) modeling. Specifically, it seeks to elucidate how substrate interactions and polymerization dynamics influence defect formation and network order, as well as study the chemical state of live 2D polymer edges. **Chapter 2** provides a summary of the current literature on Ullmann coupling, and motivates the research presented in this work. **Chapter 3** focuses on the methodology, and prepares the reader to interpret the data presented in **Chapter 4**. In **Section 4.1**, a kinetic Monte Carlo model to simulate the network quality of 2D polymers on fcc $(1\,1\,1)$ surfaces is discussed in dependence of energy barriers of kinetic transitions, and related to experimental networks in an effort to extract physical reaction parameters. In **Section 4.2**, the edges of 2D polymers are studied via Scanning Tunneling Microscopy and CO-terminated non-contact Atomic Force Microscopy and compared to theoretical models based on Density Functional Theory. **Section 4.3** briefly addresses an efficient method for differentiating between isostructural monomeric building blocks in 2D block-copolymers, namely local density of states (LDOS) mapping.

Chapter 2

Two-Dimensional Conjugated Polymers via Ullmann Coupling

2.1 Introduction

Two-Dimensional covalent polymers are a novel class of materials with unique structure and properties, not accessible in solution synthesis. They are typically synthesised using surface-assisted Ullmann coupling since great control and repeatability over the reaction product can be achieved. Upon deposition of halogenated precursors onto solid surfaces, typically coinage metals, the halogen substituents are catalytically abstracted from the monomer, generating activated species in the process. Confined to the surface, the surface-stabilized radicals can diffuse and combine, forming C−C bonds. The architecture (dimensionality, structure and composition) of the synthesised covalent network can be creatively tuned by the right choice of the halogen substitution pattern from dimers to linear chains, macrocycles, and two-dimensional networks. The role of the surface is to act as a *reactive workbench* and a delicate interplay of kinetics and thermodynamics of the monomer + substrate system has to be struck for a reduction in topological defect density.

Unfortunately, ultra-high vacuum (UHV) conditions are necessary for the synthesis of almost all 2DCPs obtained thus far. Additionally, the films suffer from small domain sizes and high defect densities, as revealed by Scanning Tunneling Microscopy (STM), making them so far unsuitable for the incorporation into functional devices[15, 16]. In 2020, a breakthrough was achieved in the collaborative research groups led by Perepichka and Rosei in their synthesis of π-conjugated P^2(TANG/TANGO) polymers with domain sizes $\sim$ 100 nm and much reduced defect densities due to a self-correcting "hot dosing" approach[17]. With this approach, the ordered network reached a critical size and for the first time allowed the direct observation of a Dirac cone in 2D organic materials by angle-resolved photoelectron spectroscopy (ARPES)[17].

In this chapter, current knowledge is summarized and important studies synthesising 2DCPs via on-surface Ullmann coupling are discussed, highlighting the difficulties for their application in devices, and potential solutions thereof. Finally, an outlook for the future of this field is provided. Several excellent reviews have served as inspiration for this chapter and can be consulted by the interested reader [5, 14, 18, 19, 20, 21, 22, 23].

2.2 Synthesis

2.2.1 General Concepts in On-Surface Polymerization

Before discussing specifics of covalent on-surface polymerization, some general on-surface chemistry concepts, such as adsorption, monomer kinetics and thermodynamics need to be resurveyed in the presence of a confining surface[24]. Most attempts in the creation of two-dimensional polymer films have been performed under ultra-high vacuum (UHV) conditions due to the inherently low interactions of the monomer with contaminants and high surface cleanliness, but polymerization on a liquid-solid interface has also been proposed[13]. In the following, only gas-solid inter-facial polymerization is discussed.

Adsorption refers to the process by which molecules adhere to a surface. Two adherence categories are normally distinguished: chemisorption and physisorption. In chemisorption, adsorbates form chemical bonds with the surface via hybridization of substrate electronic states and molecular orbitals (i.e. charge transfer). Weaker bonds, involving the polarization of both adsorbate and surface are present in physisorption, typically via van der Waals (vdW) forces.

Chemisorption is highly directional, meaning that chemisorbates stick to specific sites of the surface, that are separated by diffusion barriers. Their position and orientation with respect to the substrate strongly influence the interaction energy. At thermal energies comparable to the diffusion barriers, chemisorbates can hop between binding sites in the interaction potential, and adjust their rotation with respect to the substrate in order to minimize the interaction energy[24, 15].

In the simplest case, i.e. for spherically symmetric molecules and defect-free substrates, the interaction potential is assumed to be isotropic, and diffusion is governed by an Arrhenius diffusion equation[24]

$$D(T) = D_0 \exp\left(-\frac{E_{\text{diff}}}{k_B T}\right), \tag{2.1}$$

where D is known as the diffusion coefficient, a temperature-dependent parameter that quantifies the ease of diffusion of a monomer across the surface. D_0 is tied to the inherent mobility if

there were no diffusion barriers (i.e. $T \to \infty$), and heavily depends on the nature of the interaction (physisorbtion *vs.* chemisorption), as well as the geometry and physical size of the molecule. E_{diff} is the activation energy for diffusion. However, spherically asymmetric molecules, as well as substrate defects lead to an anisotropy of the interaction potential, i.e. $V = f(\mathbf{r}, \hat{\mathbf{v}}, \theta, \phi)$ and E_{diff} depends on the molecule's position, $\mathbf{r}$, diffusion direction $\hat{\mathbf{v}}$, as well as the rotation of the molecule, (θ, ϕ), with respect to the substrate.

An important defect-induced anisotropy is an atomic step edge between two terraces (see Fig. 2.1). The electronic structure of steps are significantly different from terraces and can lead to preferential diffusion directions. Typically, step-down diffusion between two terraces is more highly activated than step-up diffusion, due to an increased diffusion barrier, known as *Ehrlich-Schwoebel barrier*[25], E_S. Step edges can thus act as nucleation sites, since *(i)* the dwell times of molecules are much longer, *(ii)* diffusion along a step edges is enhanced, and *(iii)* monomeric species have a higher coordination number to catalyticaly active metal species.

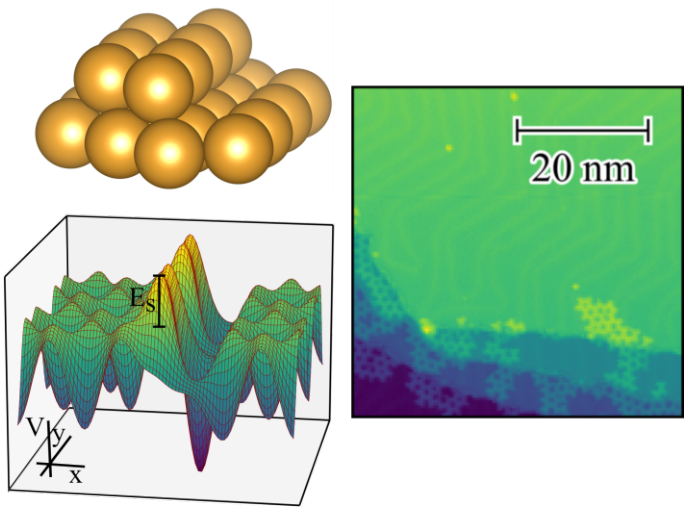

Figure 2.1: Step Edges as nucleation sites. (Left) Simplified Molecule-Surface interaction potential $V(x,y)$ in the proximity of a step edge on a fcc $(1\,1\,1)$ surface. Potential discontinuities are washed out by electron rearrangement. This leads to an increased diffusion barrier across the step and is often found to be a preferential nucleation site. (Right) STM Au(111) topograph with partial coverage of 2D trioxa-azatriangulene (discussed in more detail below) oligomers showing the preferential nucleation of the polymer at the step edges. The visibility of the $22 \times \sqrt{3}$ herringbone reconstruction demonstrates the high quality of the substrate and stability of the STM. Imaging parameters: $U = 500$ mV, $I_t = 50$ pA.

Physisorption is generally weakly directional with low molecule-surface interaction energies and can only occur at low temperatures. In fact, inert molecules (like carbon monoxide, CO) or surfaces (like hexagonal boron nitride, hBN) exclusively exhibit physisorbtion. The nature of the adsorption process strongly influences the polymerization kinetics, as weakly physisorbed molecules

typically have lower diffusion barriers, while strongly chemisorbed molecules have higher desorption temperatures.

Coverage (θ) is an important parameter for describing the adsorption of molecules to a surface and is defined as the fraction of occupied positions, N, to available positions, M

$$\theta = \frac{N}{M}. \tag{2.2}$$

The rate at which molecules are incident on a surface depends on the partial pressure of the gaseous particles, p, and is described by the Hertz-Knudsen equation

$$\frac{dn}{dt} = \frac{p}{\sqrt{2\pi k_B T}}, \tag{2.3}$$

where n refers to the number of molecules. Eq. 2.3 is often supplemented by a dimensionless prefactor, s (the *sticking coefficient*), ranging from 0 (no sticking) to 1 (every collision results in sticking), to describe the adsorption probability of the molecule to the surface. Among others, it is dependent on the cleanliness of the surface, the temperature, and the interaction between molecule and surface.

Upon adsorption, Ullmann coupling reactions take place in the 2D confinement of the substrate and fundamentally different reaction pathways occur as compared to solution, gas, or bulk environments. Due to this confinement, the reactants have fewer degrees of freedom which reduces the entropic penalty associated with the coupling reaction and the reaction product is by default restricted to be planar, which is critical for maintaining conjugation and thus for the electronic properties of the polymer. This, together with the fact that there are no solubility requirements, forms major advantages in on-surface polymerization and facilitated the synthesis of polymer structures that could not be prepared by other means[19]. This bottom-up approach of on-surface polymerization allows for great control over the formation of the polymer at a molecular level which can lead to materials with tailor-made properties.

As will be discussed below, there is an approximately linear relationship between the adhesion energy and the number of bonded monomers implying that, as the oligomer grows in size, it quickly becomes less mobile and polymerization occurs largely at the network edges with rapidly diffusing monomers. Nucleation proceeds with the initial formation of an entropically unfavoured nucleus cluster, but the subsequent addition of monomer species follows with low barriers[19]. Indeed, as evidenced in a collaborative research effort from the groups of Perepichka, Rosei and Contini,[26] a nucleation-growth mechanism model agreed well with high temporal resolution data they recorded during the polymerization process using fast X-ray photoelectron spectroscopy.

2.2.2 Surface-assisted Ullmann Coupling

Overview

The on-surface synthesis of two-dimensional polymers has been investigated by both, reversible, and irreversible bond formation between the molecular building blocks[13]. In contrast to irreversible, covalent bond formation, reversible bonds are typically better suited for low defect densities of the resulting network. However, networks that exhibit reversible bonds do not offer mechanical and thermal stability as well as high charge mobility, that are needed for the incorporation into functional devices[13]. On-surface Ullmann coupling is a two-step polycondensation process in which the advantages between the two synthesis pathways are combined: The initial dehalogenation and subsequent organometallic (OM) bond formation is reversible, and the final covalent polymerization between the monomers follows only in a separate step. The activation energy for the reaction is influenced by both the specific molecule[27] and the surface[28, 29].

The classical Ullmann reaction was first discovered in 1901 by Fritz Ullmann to produce biphenyls from aryl halides in solution, under the addition of copper powder that drives the reaction under the influence of heat[30] with CuI as a reaction product. The Ullmann reaction is thus not a catalyzed reaction in a strict sense, although it is often designated as one. On surfaces, the Ullmann reaction has been studied since 1992 by Xi and Bent,[31, 32] and has developed into the most common synthesis pathway for the formation of two-dimensional polymers on metallic surfaces[5]. Scheme 2.1 shows the initial, transition and final states (denoted as **IS, TS,** and **FS,** respectively) for halogenated trioxa-aza-triangulene monomers: The precursors are deposited on a surface, in most cases a coinage metal (Cu, Ag or Au). With an external stimulus (usually heat, but alternative pathways using an STM tip [33] or photon irradiation [34, 35, 36] have been explored as well), the halogens are catalytically abstracted and the dangling bonds subsequently stabilized, forming *surface-stabilized radicals*. A surface-stabilized radical is a molecule, whose unpaired electron level has been filled via the free electron gas of the metal surface,[15] hence the bonding character changes from physi- to chemisorbtion.

The C−C coupling between two activated monomers then follows either in a single step, or in two steps, with metastable organometallic (OM) intermediates as a sub-step, with C−C coupling following a second anneal process[14]. The emergence of OM intermediate states strongly depends on the surface and a good example of this can be found in Dong et al.[37], who deposited 1,3,5−tris(4−bromophenyl)benzene at room temperature on four surfaces (the commonly used Cu, Ag and Au $(1\,1\,1)$ facets, as well as on Ag$(1\,1\,1)$ with low external Pt adatom coverage), induced the coupling reaction via annealing and subsequently recorded STM topographs (see Fig. 2.2). With STM, the bond length between individual monomers can be accurately measured and compared to density functional theory (DFT) predictions to differentiate between C−M−C (TS)

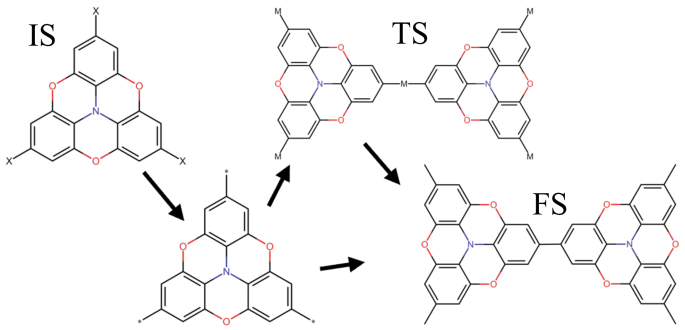

Scheme 2.1: Reaction scheme for surface-assisted Ullmann coupling of Trioxa azatriangulene precursors. Halogens X = I, Br, Cl and metals M.

or C−C (FS) bonds. Surprisingly, OM bond formation could not be observed on Au(1 1 1), which they attributed to either a short lifetime of the OM state or the C−Au−C bond being unstable.

Kinetic Models and Topological Defect Formation

Despite the dynamic (reversible) Ullmann coupling reaction, *topological defects* are still a common occurrence in the polymer. Topological defects refer to irregularities or discontinuities to the ordered network. Three-fold symmetric precursors ideally lead to a hexagonal network with hexagonal pores, but tetragonal, pentagonal, heptagonal, and octogonal pores are often observed[38, 14].

A kinetic model can help elucidate the mechanism behind the formation of 2DCPs. In an aforementioned study, Di Giovannantonio et al.[26] have proposed a nucleation-growth kinetic model and compared their prediction to experimental data that they have collected using fast X-ray photoelectron spectroscopy to precisely follow the relative fractions of **IS, TS,** and **FS**.

Role of the Halogens

Upon dissociation from the molecular precursors, the halogens adhere to the surface up to characteristic M−X desorption temperatures, which can lead to steric hindrance for the growing film. The M−X desorption temperature is typically much higher than the dehalogenation temperature [39] with equivalent energies on the order of the cohesive energies of the metals (≈ 3 eV on Au(1 1 1) for both iodine and bromine). At elevated temperatures, one might therefore expect the co-desorption of the (in the **FS**) physisorbed nanostructures with the halogens. However, as calculated in [40], this does not happen since the binding energy of physisorbed molecules is additive. For example, on Au(1 1 1), each carbon atom contributes $70-140$ meV to the overall binding energy, and hence,

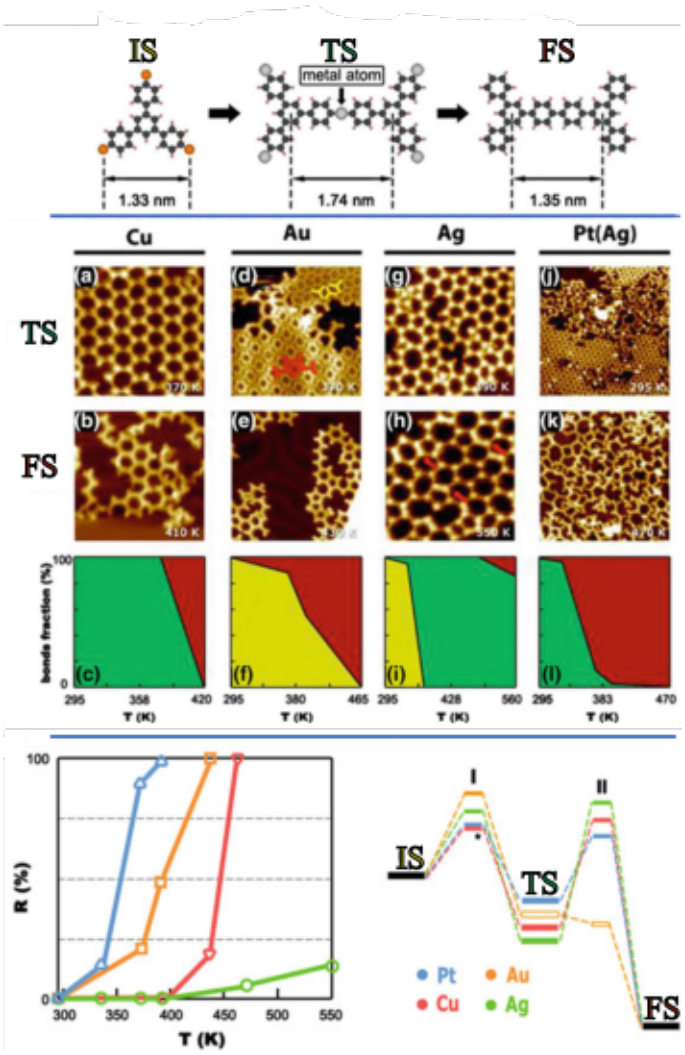

Figure 2.2: Reaction pathway on different coinage metal surfaces. Top: Reaction Scheme of 1,3,5−tris(4−bromophenyl)benzene from **IS** to **FS** over intermediate **TS** with DFT-optimized distances. Middle: STM topographs upon room temperature deposition (top row) and thermal annealing (middle row). Fraction of converted species, *R*, at different temperatures as calculated from bond length analysis (Yellow: **IS**, Green: **TS**, Red: **FS**). Bottom: Conversion ratios and schematic energy diagrams of the reaction pathway. Adapted from Dong et al.[37], Proceedings of the International Workshop On-Surface Synthesis, Springer Nature, Springer Verlag, 2016. Reproduced with permission from SNCSC.

structures with just a few tens of carbon atoms stay adhered to the surface [39, 40] even at halogen desorption temperatures. This fact has been used to synthesize the most popular 2D organic, graphene, via Ullmann coupling from hexabromobenzene monomers on Cu$(1\,1\,1)$ by keeping the surface at $\sim 570\,^{\circ}$ C during dosing and polymer growth[41]. At this temperature, the bromine adsorbates readily desorb from the surface, facilitating the growth of low defect density graphene. While this is a useful "trick", this approach does not necessarily work for every monomer species,

since many 2DCPs decompose at lower temperatures. A problem is that the relationship between defect density and halogen adsorbates is not very well understood and has not been studied in depth so far. In STM images of 2DCPs post-polymerization, the adsorbates are typically found to organize themselves into the pores of the network in energetically favourable configurations[42].

The Role of the Surface

The surface plays a multitude of roles in the facilitation of covalent polymers via Ullmann coupling, as it crucially influences the kinetics and thermodynamics of the proceeding reaction, and thereby the structure, dimensionality and composition of the polymer. An in-depth discussion can be found in an excellent review written by Grill and Hecht[19].

The choice of the substrate chiefly determines adsorption energies and catalytic activity, which influence activation and diffusion of the molecular building blocks[19, 39]. If monomer + substrate adsorption energies are too low, the monomers might desorb at temperatures lower than the dehalogenation temperature. On the other hand, diffusion barriers could be too high if adsorption is too strong leading to many nucleation sites and small domains. An good example of the interplay between adsorption and efficient diffusion can be found in Marco Bieri et al. [15]. In their study, hexaiodo-substituted cyclohexa-m-phenylene (CHP) macrocycles were deposited on the three most commonly used surfaces for covalent self-assembly, Cu$(1\,1\,1)$, Ag$(1\,1\,1)$ and Au $(1\,1\,1)$, and subsequently polymerized into polyphenylene networks. The polymer networks were then analysed using STM and compared with generic Monte Carlo simulations to uncover the relation between diffusion and coupling affinity to network quality. The resulting structures on the three substrates ranged from branched morphologies on Cu to extended, regular 2D networks on Ag (see Fig. 2.3). This result was attributed to a low diffusion barrier of the CHP surface-stabilized radicals (or low coupling affinity) on Ag, whereas the opposite is the case on Cu with Au serving as an intermediate between the two.

Depending on the crystal structure and surface orientation, any surface exhibits a certain atomic corrugation which influences molecular diffusion and orientation and thereby the polymerization reaction pathway[22, 19]. This *templating* feature of the surface has repeatedly been used to introduce a further variable to control the reaction pathway and the architecture of the reaction product. For ordered 2D networks, low index coinage metal surfaces are typically studied as substrates, as they are inherently catalytically active and enable efficient diffusion. Densely-packed $(1\,1\,1)$ surface facets, in particular, are relatively isotropic thus offering weak templating which can reduce epitaxial strain and defect density. Stepped surfaces (like $(1\,1\,0)$ or $(1\,0\,0)$), are implemented, to favour molecular diffusion along low-corrugation directions, like missing atomic rows, to achieve a preorganization of the monomers into polymerized chains or macrocycles, with a second activa-

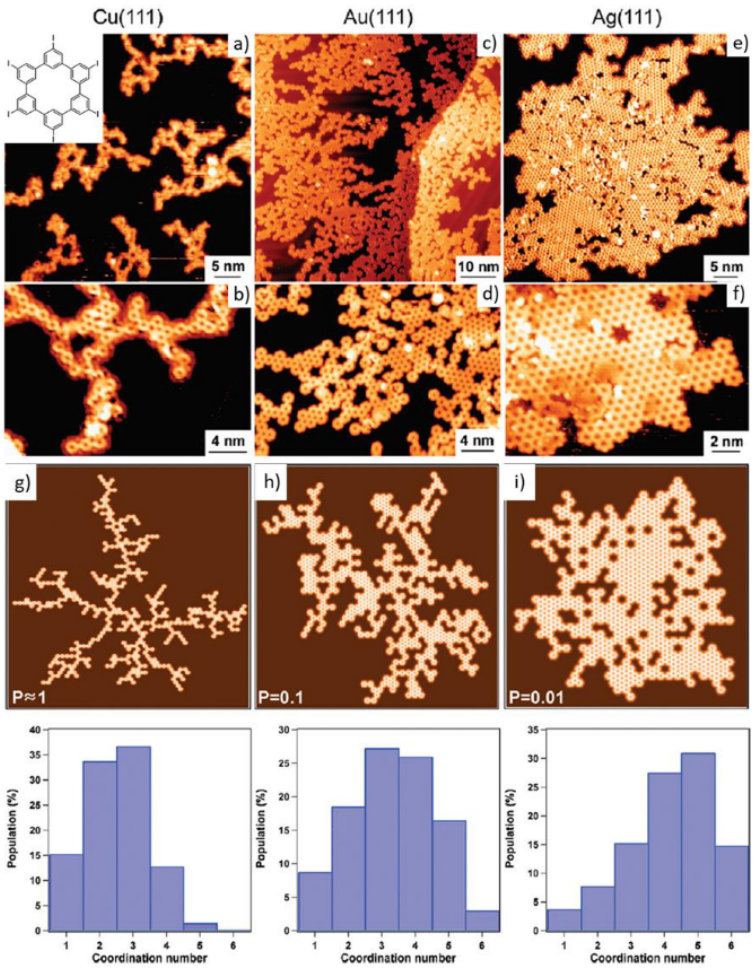

Figure 2.3: Overview and High-resolution STM images of polyphenylene networks on Cu, Au, and Ag $(1\,1\,1)$ (a)-f)) and Monte Carlo simulations of molecular network growth (g)-i)) with coupling probabilities, $P = 1, 0.1$, and 0.01, respectively. Below each simulation, the coordination number distribution for the molecules in the cluster are given. The qualitative agreement between the experimental and simulated networks is interpreted in light of classical diffusion-limited aggregation theory as differing energetic barriers for diffusion, and coupling (see text). Adapted with permission from Bieri et al.[15]. Copyright 2010 American Chemical Society.

tion step to covalently link individual structures into an ordered network. This kind of *hierarchical growth* can also be achieved by functionalizing the monomer units with two different halogen species that can be sequentially cleaved off through thermal activation[43, 44].

Possible Architectures

In 2007, Grill et al. [45] nicely demonstrated that the dimensionality of the reaction product could be controlled using tetraporphyrin precurors with varying degree of bromine substitutes. Indeed, the choice of the molecular building block, as well as halogen substituent positions determines the

architecture and can be freely tuned from dimers (0d), chains (1d) to networks (2d) (see Fig. 2.4).

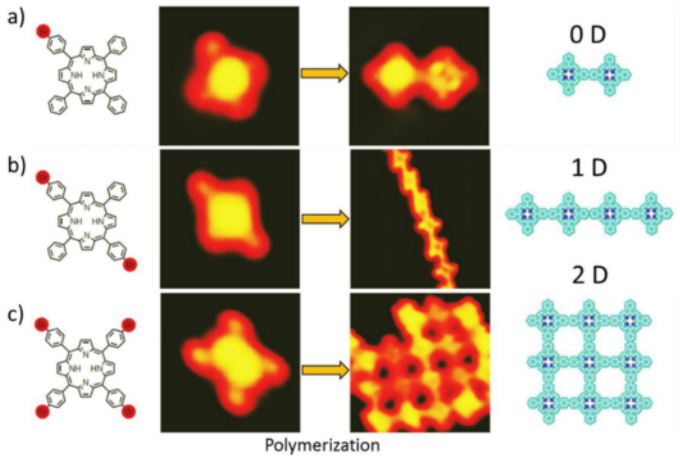

Figure 2.4: Porphyrin precursors with one (a), two (b), or four (c) bromine substituents. Depending on the number on position of the halogen substituents on the molecular building blocks zero-, one- or two-dimensional nanostructures can be polymerized. The geometries are validated using STM (middle panels). Adapted from Grill et al.[45] Nature Nanotechnology, **2**, Springer Nature, 2007. Reproduced with permission from SNCSC.

Furthermore, the symmetry of the halogen substitution pattern on the precursor molecules determines the topology of the network [14] as can schematically be seen in Fig. 2.5. While the conjugated backbone structure is not unique to 2DCPs, but can also be found in 1D chains, the regular arrangement of monomers in two dimensions leads to the emergence of unique, and, perhaps surprising electronic states and band structure that distinguishes them from conjugated 1D polymers and permits a much broader range of potential technological applications[46]. The relationship between topology and bond nature to electronic structure has been discussed in several theoretical works[46, 47]. As an example, it was demonstrated by Thomas et al.[47], that hexagonally symmetric sheets of extended 2DCPs can lead to energetic flat bands and Dirac cones in k-space. Since the mass, and thereby the mobility of charge carriers in materials is fundamentally connected to curvature of the potential energy with respect to the crystal momentum, ordered Kagomé 2DCPs exhibit both massless charge transport and very large effective masses which are useful to study highly correlated systems.

2.2.3 Insulating Substrates

This section will focus on recent attempts to electronically decouple 2DCPs that have been synthesised via Ullmann coupling from the underlying substrate. However, it should be mentioned that other on-surface reactions for the synthesis of 2DCPs on insulating substrates directly are actively explored. The interested reader is referred to recent reviews. [18, 14, 19, 20, 21]

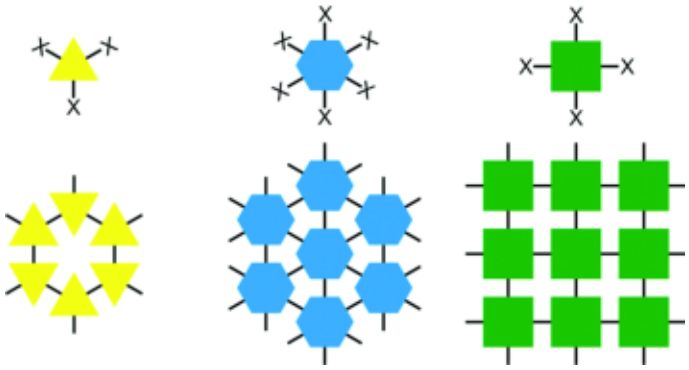

Figure 2.5: The positioning of halogen substituents (X = I, Br, or Cl) within the chosen molecular building block determines the topology of the resulting covalent network. Reprinted from [14]. Used with permission of Royal Society of Chemistry, from Surface-assisted Ullmann coupling, M. Lackinger, **53**, 56 (2017); permission conveyed through Copyright Clearance Center, Inc.

As shown thus far, metal surfaces exhibit several advantages for on-surface synthesis. The metallic free electron gas readily anchors the precursor molecules to the surface via London dispersion forces, thereby providing an ideal catalytic environment to initiate the reaction without monomer desorption. However, future technological applications demand 2DCPs to be either transferred to or directly synthesised on insulating substrates (bulk insulators, or thin film insulating layers). Most importantly, this is because there is a need to electronically decouple the polymer from the metallic substrate - Electron energy levels of the thin film can shift significantly due to screening, making investigations of the inherent properties of the polymer hard to discern from the properties of the metallic substrate. As an example, for conductivity measurements, as routinely performed for conventional semiconductor materials, the metal support offers low-resistance conduction pathways dominating measured currents.

For graphene, numerous transfer protocols have been developed, such as *template-stripping*, where a polymethyl methacrylate (PMMA), or other adhesive layer is spin-coated and the underlying metal substrate chemically removed, *viscoelastic stamping*[48] or *contact printing*[14]. These intriguing approaches have been investigated for 2DCPs by some groups[49, 50], however, they have not been too successful either because of the presence of contaminants associated with spin-coating, or because the adhesion forces of the polymer to the metal are so strong that stamping is only possible from one metal substrate to another. An open question in all transfer protocols of these materials is about their scalability to compete with industrial standards.

A more direct approach to electronically decouple a molecular monolayer from the metallic substrate has been investigated by Lackinger's group[51] who polymerized 1,3-bis(p-bromophenyl)-5-(p-iodophenyl)benzene on Au$(1\,1\,1)$, and subsequently dosed the hot polymer/metal with iodine to achieve chemisorbed iodine monolayers. The electronic decoupling could be shown in STM

images, where decoupled polymeric structures showed up with altered contrast as compared to parts of the film that were still attached to the underlying metal as a consequence of the decreased screening of the wave functions of the valence electrons of the polymer (see Fig. 2.6). This decoupling step could potentially also be implemented not only with iodine, but, depending on the metal, also with oxygen[52] or chlorine vapor to form closed, intercalated monolayers. This approach to effectively decrease adhesion between polymer and metal substrate, could potentially be combined with the transfer approaches discussed above.

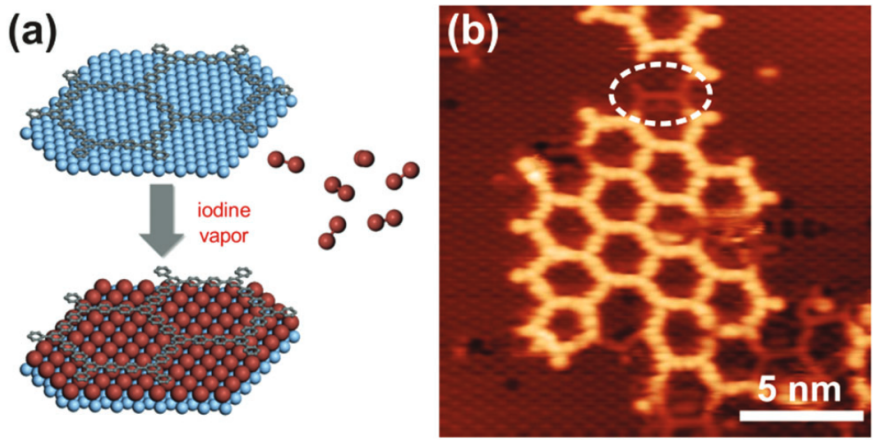

Figure 2.6: Electronic decoupling approach via deliberate iodination. (a) Schematic showing the grown molecular structure before and after iodination. The pore size of the 2DCP succesfully facilitates intercalation of iodine vapor, forming closed monolayers between. (b) STM image showcasing decoupled polyphenylene network. The broadened edges correlate with molecular orbitals of free-standing polymer. The dashed ellipse indicates a region of the polymer that is still attached to the metal. Reprinted from Rastgoo-Lahrood, et al. (2016)[14, 51] *Angew. Ch. Int. Ed.*, 55(27), 7650 –7654 with permission from Wiley-VCH Verlag.

A recent highlight to facilitate Ullmann-type coupling on an insulating substrate directly has been presented by Kittelmann et al.[53], who cleverly designed halogenated benzoic acid monomers, such that the interaction of their carboxylate side groups and a bulk insulator $(10\bar{4})$-calcite ($CaCO_3$) is increased significantly to avoid desorption at the heat-induced debromination and coupling step. With this approach, they managed to synthesize 1D conjugated chains without the need for a metal catalyst. However, the synthesis of 2D networks might not be feasible with a similar approach, since ordered 2D networks have a much higher entropic penalty than 1D chains, and, as discussed above, the presence of metal catalysts serves the additional purpose of organising the stabilized radicals into reversible coordination-networks that can self-heal structural defects.

This approach does however raise questions about the possibility of co-depositing metal adatoms with similarly functionalized monomer species on bulk insulators. So far, the role of adatoms has mainly been investigated on other metal substrates by evaporating a more reactive metal species

prior to the deposition of the precursor materials[37, 54]. In those studies it was found that dehalogenation of the precursors occurs at reduced temperatures, as compared to without the presence of external adatoms. Zhao et al.[55] have investigated the possibility of sequentially depositing first the monomeric species 1,3,5−tris−(4−bromophenyl)benzene (TBB) on a single layer of hBN and in a second step Cu and Pd adatoms. In both cases, they found that dehalogenation occurs at much reduced temperatures as compared to the no-catalyst case with different reaction pathways, however, the synthesized oligomers do not, so far, reach critical size and defect density.

2.3 Applications

The lower-dimensional parents to 2DCPs, one-dimensional π-conjugated polymers (1DCPs), have attracted great interest as semiconductor materials in (opto)electronic devices such as organic solar cells, organic field-effect transistors and organic photodetectors. While ballistic charge transport effectively occurs along the polymer backbone, interchain charge transfer represents a slower, inefficient process,[56] that ultimately limits their application and motivated the expansion of conjugated polymers into the second dimension[13].

Graphene-like 2DCPs have the potential to keep up the organic electronics momentum from 1DCPs and break the electronics=silicon association. Silicon transistors have continuously shrunk in size enabling an exponential growth of the number of transistors that can be packed in a given area (*Moore's law*). However, this miniaturization has hard physical limits[5] in both fabrication (Abbe diffraction limit for photolithography, Amdahl limit for parallel processing, etc.) and application (gate oxide thickness, current leakage, etc.). While many 2D materials-based transistor structures have been shown to exhibit some superior properties over silicon-based ones, their newness does not necessarily reflect an actual superiority over them and their disruptive potential should be critically examined[57].

Thin-film transistors (TFTs), the primary component in backplane circuitry for flat displays, are perhaps the most promising market niche for 2DCPs and other graphene-like 2D materials. This is because TFTs have generally low performance and size demands, but their fabrication with a−Si could be cheaper[57, 58]. Due to their covalent bonding nature, 2DCPs possess additionally high thermal and mechanical stability which makes them suitable candidates for flexible electronics[59].

A, so far, largely untapped potential for 2DCPs represents 2D lateral heterostructures. These block-copolymers consist of adjacent domains of chemically distinct 2D materials, seamlessly joined within the same plane. Due to their similar lattice constants, isostructural precursors are ideal candidates for this application. Such heterostructures exhibit intriguing properties, such as charge separation at the donor-acceptor interfaces, tunable bandgaps, and localized plasmonic res-

onances. These features make them attractive for applications in photovoltaics, optoelectronics, and catalysis. Moreover, the ability to pattern heterostructures using advanced lithographic or tip-based techniques opens avenues for integrating 2DCPs into more complex device architectures.

2.4 Conclusion

In conclusion, this chapter elaborates on the synthesis, characterization and applications of two-dimensional conjugated polymers (2DCPs) synthesized via on-surface Ullmann coupling. The synthesis is primarily conducted on coinage metallic substrates under ultra-high vacuum (UHV) conditions and leverages it's ideal catalytic environment for the formation of engineered 2D networks with specific topological and electronic properties. Some of the issues of 2DCPs that needs to be resolved before they can be incorporated into functional devices are[5]

- **Deeper Insight into Ullmann Reaction**: While surface-assisted Ullmann coupling is a widespread technique for realizing 2DCPs, there are still many open questions about the reaction pathway, in particular about the reaction parameters.
- **Substrate Independence**: The development of new transfer protocols of the polymer from "growth" to "host" substrate, i.e. from metal surfaces to insulators, or the direct growth of 2DCPs on bulk insulators.
- **Network Quality**: The reduction in topological defects that form during growth, as well as an increase in their domain sizes.

Chapter 3

Theory and Experimental Methods

To study nanostructures on a substrate, high-resolution surface-sensitive techniques are required. In this chapter, the main experimental methods of this thesis, scanning tunneling microscopy (STM) and non-contact atomic force microscopy (ncAFM), are introduced, along with auxiliary surface analysis techniques, such as low energy electron diffraction (LEED) and Auger electron spectroscopy (AES).

All these techniques are integrated into a custom UHV system consisting of two connected chambers: a preparation chamber and the Infinity SPM chamber. The preparation chamber houses the LEED and AES setup, along with surface cleaning and polymer growth equipment. An additional load lock connected to the preparation chamber allows for efficient sample transfer from outside the system. The Infinity SPM chamber can operate across a wide temperature range (10 K to 420 K) with a pulse tube cooler, ensuring vibration-free, stable STM and ncAFM measurements. Each chamber maintains UHV conditions through the use of an ion getter pump. A turbo pump, connected to the preparation chamber via a large gate valve, is used when the chamber pressure exceeds 1×10^{-7} mbar, such as during sputter cleaning of samples (see section 3.4). The base pressures in the Infinity SPM and preparation chambers are 1×10^{-11} mbar and 1×10^{-10} mbar, respectively. Unless specified otherwise, SPM data is taken at 10 K.

3.1 Scanning Tunneling Microscopy (STM)

The scanning tunneling microscope (STM), invented in 1981 by Gerd Binnig and Heinrich Rohrer (IBM laboratories), revolutionized surface science by enabling electronic structure imaging on the atomic scale, and atomic manipulation on conductive surfaces. A truly groundbreaking discovery, for which Binnig and Rohrer would later share the 1986 Nobel Prize in Physics with Ernst Ruska (Technical University of Berlin), who was recognized for his pioneering work on the electron

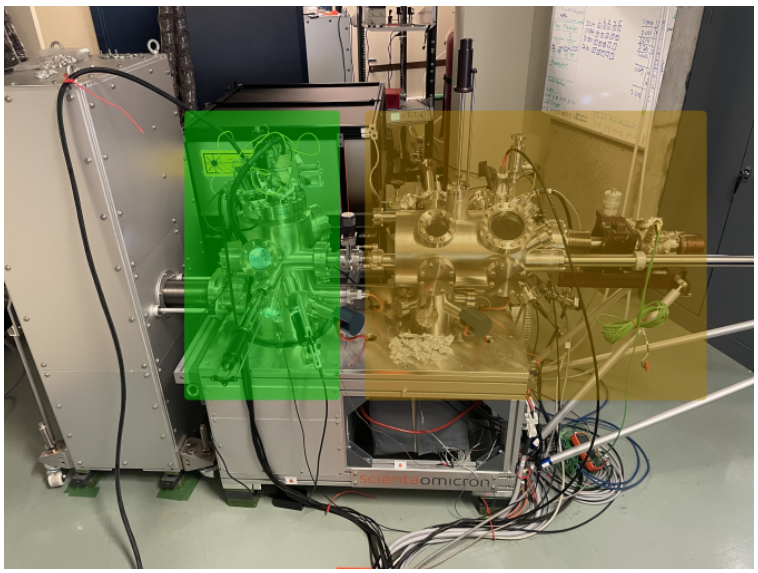

Figure 3.1: UHV system utilized in this thesis. The ScientaOmicron Infinity SPM chamber, and preparation chamber are marked in green, and yellow, respectively.

microscope. Since its inception, the STM has matured into an essential tool in nanotechnology and materials science.

3.1.1 Basic Principle

STM operates on the principle of quantum tunneling, where a sharp metallic tip is brought within a few angstroms of a conductive surface, allowing electrons to tunnel between the tip and the sample when a bias voltage is applied. The resulting current is highly sensitive to the tip-sample separation, d, which enables the STM to visualize the local electronic density of states (DOS) on the atomic scale:

$$I_t = cUe^{-2\sqrt{2m_e\Phi}/\hbar d}, \tag{3.1}$$

where c is a constant, U is the applied bias, Φ the work function difference, d the tip-sample distance, m_e the electron mass, and $\hbar$ the reduced Planck constant. A set of piezoelectric transducers (xy) raster-scan the tip over the sample in one of two principal imaging modes:

1. **Constant Current Mode**: An electronic feedback loop ensures a constant tunneling current by engaging the z-piezo to move the tip closer to/away from the surface.

2. **Constant Height Mode**: The tip-sample distance is kept constant and variations in tunneling current are recorded.

Constant Current Mode, which is the most commonly used mode, is employed in this work. The resulting map of the z-piezo extension over the scanned area is often described as the sample's *topography*. Although this map can effectively represent surface corrugations, it is important to note that the tunneling current measured by STM does not solely depend on atomic corrugations, but also on the local density of electronic states (LDOS). To gain deeper insight into the electronic properties of surfaces, scanning tunneling spectroscopy (STS) can be employed. In STS, the tip is positioned above a point of interest, while the tip-sample bias is swept and modulated with a small AC component. A lock-in amplifier singles out the modulated signal in the tunneling current for each applied bias, i.e., the local differential conductance (dI/dV) as a function of bias, which allows one to infer features related to the band structure (see Fig. 3.2). STS may be used to measure molecular energy states or semiconductor band gaps. Performing STS on each point of a grid over a region of interest allows the localization of specific features in the differential conductance.

In studies of 2DCPs, STM is primarily implemented to assess the quality of the network in-situ, i.e. immediately upon polymerization. STM topographs can provide information about surface coverage (θ), uniformity, and network quality, such as the density of topological defects. Bond lengths between monomer units can provide information about the nature of the linkage, i.e. whether it's carbon-carbon coupled (R−C−C−R) or organometallically coordinated (R−C−M−C−R), where M represents a metal (Cu, Ag, Au) atom (see also Fig. 2.2). Carbon-carbon bonds are shorter and more rigid and lead to a thermally, and chemically more stable polymer with delocalized π-electrons, whereas an organometallic linkage leads to a more flexible structure with different electronic properties depending on the coordinating material [60].

To electronically decouple single molecules from the conductive substrate, Repp et al.[62] have grown epitaxial mono- to bilayer islands of NaCl on a Cu$(1\,1\,1)$ surface and subsequently dosed the surface with pentacene molecules. After, the STM tip was placed above a single pentacene molecule and dI/dV spectra were recorded. The spectra showed peaks in the conductance at well-defined voltages, which correspond to the energy levels of the unperturbed molecule (see Fig. 3.2 b)), indicating that it was well electronically decoupled from the metal surface by the thin dielectric. For STM studies, the intermediate insulating sheet must be thin enough to achieve a tunneling current between tip and sample.

3.1.2 Tip Preparation and Calibration

All presented SPM measurements were performed with commercial tungsten tips, either mounted on tuning fork force sensors (for simultaneous STM/ncAFM measurements; See section 3.2.2), or in rigid tip carriers (for STM measurements). Out of all pure metals, tungsten has the highest tensile strength, which makes it exceedingly stable, even at very high temperatures. Furthermore,

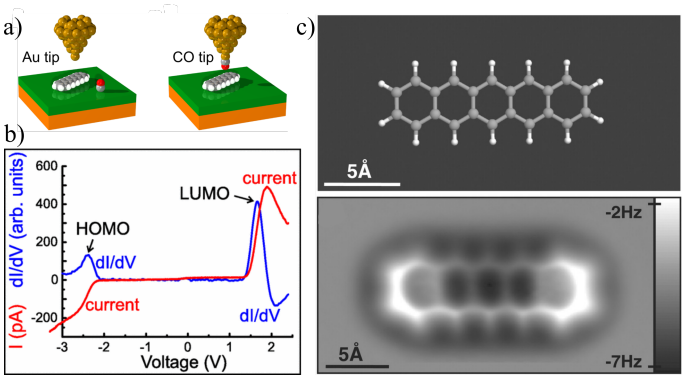

Figure 3.2: SPM studies of a single pentacene molecule on a NaCl/Cu(1 1 1) island. (a) Schematic representation of an atomically sharp Au tip before and after termination with a single CO molecule, with NaCl support (green) on a metal substrate (gold). (b) dI/dV spectroscopy of a single pentacene molecule showing well-defined peaks in the conductance corresponding to the HOMO and LUMO levels of the molecule. (c) Ball-and-stick model of free-floating pentacene (above) and Δf-map recorded with a CO-terminated ncAFM tip (below). (a) Reprinted from Mohn [61] with permission from the author. (b) Reprinted from Repp et al., *Phys. Rev. Lett.*, **94**, 026803 (2005), with permission. Copyright 2005 by the American Physical Society [62]. (c) Reprinted from Gross et al. (2009) [63]. Reprinted with permission from AAAS.

it can be etched into very sharp geometries using NaOH or KOH solution—an essential feature for achieving high spatial resolution in SPM scans.

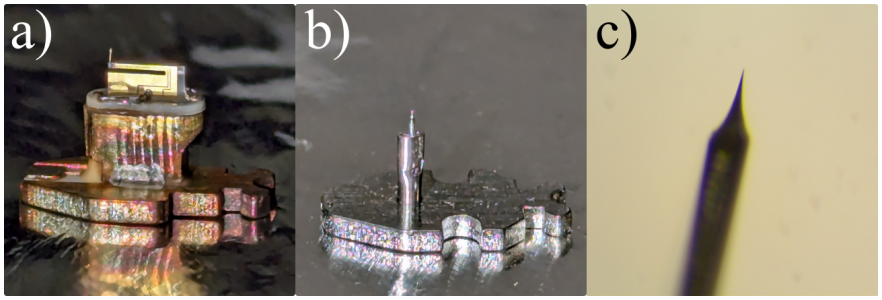

Figure 3.3: Sensors used in this work. (a) shows the tungsten tip mounted on a quartz tuning fork for simultaneous STM/ncAFM measurements. (b) shows a tip inside an STM tip carrier for STM measurements. (c) shows an optical microscope image of the tip. The tip apex radius is ≈ 10 nm.

The main drawback of these tips is their rapid oxidation when exposed to the atmosphere. Therefore, in-situ treatment is required to break the oxide layer and optimize the tip for atomic resolution imaging. This can be done by bringing the tip close to a clean metal surface with a high bias voltage ($1-10$ V) and a low tunneling current ($10-50$ pA). A series of short voltage pulses ($4-10$ V) lasting 50 ms, controlled tip diving ($1-20$ nm), or a combination of both methods can break the oxide layer and shape the tip into a high aspect ratio, ensuring only a small cluster of atoms contributes to the signal and enhancing spatial resolution. Due to the close contact of the tip

with the sample, it is likely for the tip apex to change, which can have adverse effects on the spatial resolution, in which case the tip has to be reconditioned. A common undesirable tip termination is a double, or multi-tip, in which case several locations, spatially apart, contribute substantially to the overall tunneling current. This introduces scan artefacts, like ghosting or lopsidedness of features. Tip conditioning is performed until (a) small tip pokes of ≤ 1 nm into the surface result in a small and round protrusion of it, (b) Friedel oscillations of the free electron gas on metallic surfaces can be observed on defects and step edges, and (c) the tip is stable, i.e. experiences no change in it's imaging quality, under the application of a series of small bias pulses ($3-4$ V). Since the tunneling current has an exponential distance dependence with fast decay, these conditions can generally be reached as long as there is only a single protruding atom on the tip. In ncAFM, the force gradient is detected, which generally has a much slower exponential decay by comparison, meaning that the cluster of atoms that interacts with the surface is typically larger than in STM. As a consequence, a tip that has been conditioned to result in desirable STM data quality, does not necessitate desirable ncAFM data quality. A proxy for the volume of the atomic cluster that contributes to the signal in ncAFM measurements, i.e. a proxy for the aspect ratio of the tip, are the $df(z)$ spectroscopy minima values over well-known sites on the surface. If the aspect ratio is high, the curves will have a comparatively low frequency shift minimum, while the opposite is the case if the aspect ratio is low, i.e. when the tip is blunt.

On the other hand, STS measurements require a tip with a relatively feature free DOS over the desired region in energy space to discern sample features from those of the tip.

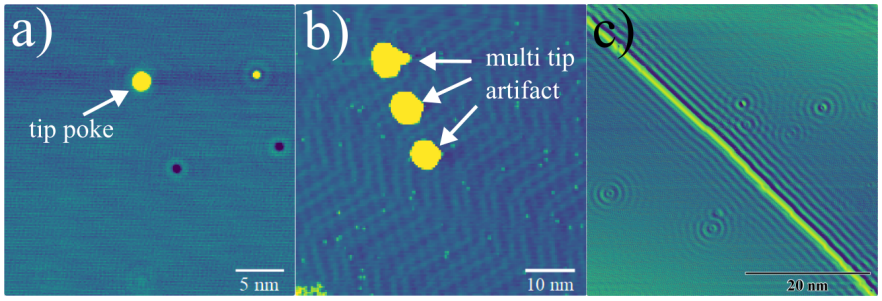

Figure 3.4: STM Tip Conditioning. (a) shows an *ideal* tip poke on a Cu(1 1 1) surface. (b) shows a Au(1 1 1) surface after a tip poke with a multi tip. (c) Flattened STM image showing Friedel oscillations on a Cu(1 1 1) surface of a step edge and various point defects. Imaging parameters: (a) $U = -500$ mV, $I_t = 50$ pA. (b) $U = 500$ mV, $I_t = 100$ pA. (c) $U = 100$ mV, $I_t = 250$ pA.

3.2 Non-Contact Atomic Force Microscopy (ncAFM)

While it's less commonly found in studies of 2DCPs, non-contact atomic force microscopy (ncAFM) has several advantages over it's cousin and historical predecessor STM, and will become increasingly valuable in future studies. The main advantage of ncAFM over STM is that it is not limited to conductive samples, while retaining, if not exceeding, the high resolution imaging capability of STM. Indeed, as will be described below, ncAFM has routinely been used to atomically resolve the fine structure of single molecules, as well as extended nanostructures. In addition, ncAFM is sensitive to the total DOS, while STM is primarily mapping the charge density at the Fermi level, making it in principle a superior imaging tool, although it requires more sophisticated control electronics.

3.2.1 Basic Principle

In ncAFM, an atomically sharp, oscillating tip is brought into close proximity with the sample surface. Depending on the interaction forces between the oscillating tip and sample, the resonance frequency shifts to smaller (attractive regime) or larger (repulsive regime) values, depending on the interaction of the tip with the sample. A general formula for the frequency shift acquired during the oscillation of the cantilever has been derived by Giessibl [64],

$$\frac{\Delta f}{f_{\text{res}}} = -\frac{1}{\pi a k}\int_{-1}^{1} F\left(z + a(1+u)\right)\frac{u}{\sqrt{1-u^2}}\,du, \tag{3.2}$$

where k is the spring constant of the cantilever, F is the interaction force between the tip and sample, f_{res} the resonance frequency of the unperturbed cantilever, Δf is the frequency shift from resonance, a the amplitude of oscillation, and z the distance of closest approach between tip and sample [65].

Similarly to STM, the tip can then be scanned across a surface, with a feedback loop controlling the piezo extension of the tip to ensure a constant frequency shift, Δf. This mode is known as constant-Δf imaging, or constant frequency shift mode. The oscillation amplitude is kept constant by an amplitude feedback loop (AFL), while a phase-locked loop (PLL) tracks the frequency shift as the tip interacts with the sample and ensures that the sensor is excited at resonance. A more detailed explanation of the role of these feedback mechanisms can be found in the works of Cowie [66] and Voigtländer [67], who provide comprehensive analyses of ncAFM systems and their controllers.

Similarly to STM, the tip can also be scanned across the surface in constant height mode, where the the z-feedback loop is disabled. Despite the inherent risk of tip crashes, constant height

mode is utilized in atomic resolution studies. This is mainly because the tip moves in a repulsive interaction regime, making the z-feedback loop inherently unstable since the objective function is non monotonous.

A recent advancement in ncAFM catapulted the achievable imaging resolution of a few Ås down to the sub-Å regime. This impressive feat is achieved by "terminating" the tip via a single physisorbed molecule, most commonly CO. The flexible, atomically sharp molecule experiences strong Pauli repulsion in close proximity to the surface and bends in the interatomic interaction potential, thereby increasing frequency contrast [68]. CO-terminated studies were first implemented in 2007 by Gross et al. [63] to resolve the structure of single molecule pentacene ($C_{22}H_{12}$) on a NaCl support.

3.2.2 The qPlus Sensor

The qPlus© sensor, developed by Franz Giessibl [69], can be operated in both STM and ncAFM modes. QPlus sensors are based on quartz tuning forks, commonly found in mechanical wrist watches, where one prong of the tuning fork is fixed, while the other oscillates with oscillation frequencies in the $20-30$ kHz range with Q-factors (Q) of $50,000$ to $300,000$, at 10 K and in UHV. The oscillation of the free prong is detected via the piezoelectric effect of the quartz during the oscillation. The sensor is said to be self-sensing for it does not need a separate oscillation detection setup (optical beam deflection, or interferometric setups), like in conventional cantilever ncAFM. A typical resonance curve is shown in Fig. 3.5. A metallic tip is glued to the end of the freely swinging prong, see Section 3.1.2. QPlus sensors exhibit very high stiffness, making them ideal candidates for stable operation at very low oscillation amplitudes, while limiting the risk of the tip snapping into contact with the surface under the influence of attractive forces. The stable operation at low oscillation amplitudes is crucial for atomic resolution imaging, since interference from long range forces is inherently reduced. Indeed, as pointed out by Giessibl et al.[70], optimal sensing in fm mode is achieved with oscillation amplitudes, A, on the order of the decay length λ of an exponentially decaying force $F(z) \propto e^{-z/\lambda}$. For short-range chemical interaction forces, the oscillation amplitude should be kept as low as possible, on the order of 1 Å [63, 71].

3.2.3 CO-terminated Studies

In 2009, Leo Gross et al. [63] achieved atomic resolution on organic molecules for the first time by functionalizing the tip with a single CO molecule (see Fig. 3.2c). Since then, the functionalization of ncAFM (and even STM) tips with a single CO molecule has become a standard for achieving high spatial resolution on molecular systems. While other terminations are actively

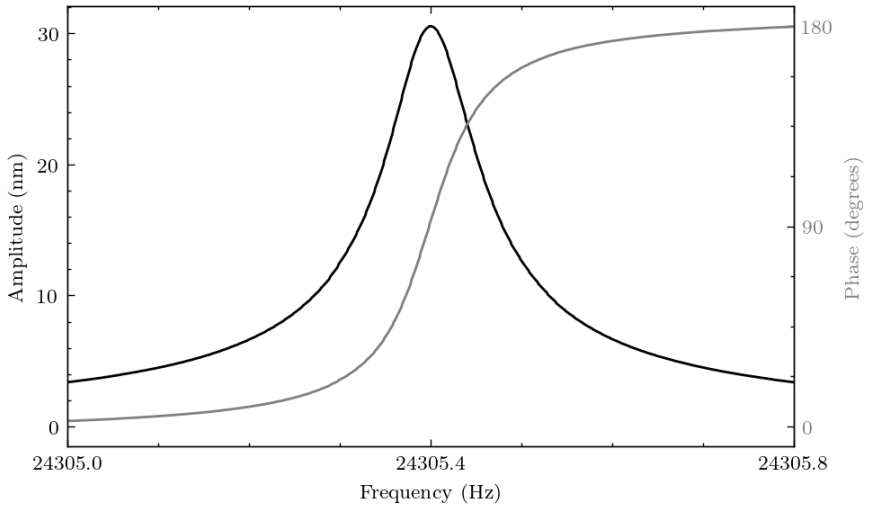

Figure 3.5: Amplitude and phase characteristic for a standard qPlus sensor at 10K. The center frequency is indicated on the abscissa at approximately 24 kHz, with a quality factor (Q) of $270,000$.

being investigated, CO molecules present themselves as ideal candidates for probing short-range repulsive interactions, such as Pauli repulsion, while minimizing the risk of chemically modifying the sample during the imaging process. This is owed to their inherent chemical inertness. With this approach, individual atoms, molecular bonds, as well as bond orders can be clearly visualized, making it an invaluable tool in surface science and nanotechnology.

However, the imaging mechanism of CO-terminated tips is a complex combination of short-, and long-range interactions, and interpretation of images obtained via CO-terminated ncAFM can be difficult, and it is important to understand the origin of the emergent contrast. Key contributors to the total interaction include van der Waals attraction, electrostatic forces, and, most importantly, Pauli repulsion, which varies with atomic resolution [72]. During the approach of the tip to a molecule, the electron wavefunctions of tip and molecule overlap, resulting in an increase in the kinetic energy due to the Pauli exclusion principle [73]. This interaction leads to a lateral relaxation of the rigid molecule in the local tip-sample interaction potential, as shown by Hapala et al. [68]. As consequence of this lateral slipping of the molecule, the tip effectively probes saddlepoints, or ridges in the interaction potential with atomically sharp edges. The origin of ridges in the interaction potential could be localized charge densities, for example due to the presence of an intermolecular bond. On top of that, the well-defined quadrupole p-wave character of the CO molecule enhances the lateral resolution, especially in molecules with pronounced electrostatic interactions [73].

A particularly valuable capability of CO-terminated ncAFM for studying aromatic hydrocarbon systems is bond-order discrimination. In such systems, bond length and electron density vary subtly. With CO-terminated tips, it has been shown that hexagon-hexagon, and hexagon-

pentagon bonds can be distinguished via sub-angstrom variations in apparent bond length in C_{60} [74]. By recording frequency shift-distance spectra at various lateral positions, three-dimensional force maps can be constructed via the following inversion of eq. 3.2, based on Sader and Jarvis [65] (under the small amplitude approximation):

$$F(z) = 2k \int_z^\infty \Omega(z')dz', \tag{3.3}$$

where $\Omega(z) = \Delta f(z)/f_{\text{resonance}}$, and k is the spring constant. Such force maps capture molecular tilt, adsorption height, and binding sites with spectacular accuracy. For example, in the breakthrough publication by Gross et al. [63], pentacene adsorbed on a metallic substrate has been shown to exhibit a non-planar adsorption geometry. Such information is crucial for understanding the interplay of organic molecules with the underlying substrate.

Complementary to traditional methods, like nuclear magnetic resonance (NMR) or mass spectrometry (MS), where spectroscopic data might be insufficient in certain systems, CO-terminated ncAFM finds increasing application for molecular identification. For instance, it has been used to identify reaction intermediates, and products of on-surface chemistry [75]. Particularly in combination with computational tools, such as density functional theory (DFT), molecular structure elucidation is enhanced further.

Tip Preparation

All CO-terminated AFM tips in this thesis were prepared using a standardized preparation procedure similar to a procedure described in Bartels et al. [76]:

1. qPlus tips are prepared in STM mode until electronic standing waves scattering from inhomogeneities in the surface are observed (so called *Friedel oscillations*, see chapter 3.1.2).

2. A CO gas tank is opened, and the gas line purged by cycles of flushing and pumping of the gas line. CO gas is then introduced to the measurement chamber through a designated leak valve. The cooling shield is then opened for 30-90 s at a partial pressure of $p_{\text{CO}} = 1 \times 10^{-9}$ mbar and permitted direct geometrical access to the tip-sample junction. The tip is retracted by $30 - 50$ coarse motor steps in the process.

3. Upon relanding, single CO molecules, as well as molecular aggregates can be identified in STM images of the surface. It is known that the molecules adsorb upright with the C end physisorbed to the metal substrate. [76, 61]

4. The tip is placed above such a molecule and lightly *dipped* towards the sample surface. The topography trace is observed simultaneously. If the z-Feedback causes the tip to move closer

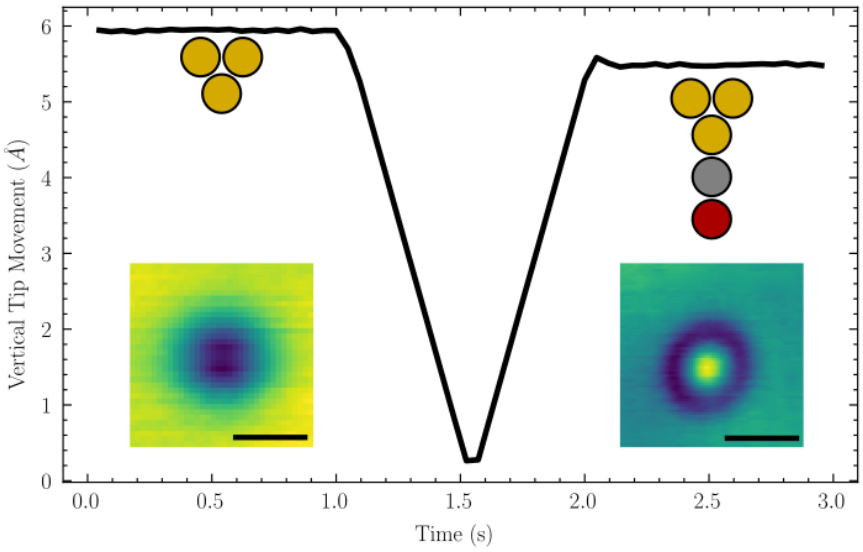

Figure 3.6: Time trace of the z-piezo extension during controlled CO pickup. The inset schematically shows the apex of the metallic tip before and after the controlled tip dive, with corresponding STM scans of other CO molecules adhered to the metal surface. The scale bar in the STM scans is 500 pm. Imaging parameters: $U = -300$ mV, $I_t = 100$ pA.

to the sample after the poke, i.e. if the apparent length of the tip decreases by 0.4 Å, a CO molecule may have attached to the tip apex with the C bonding with the metal atom (see Fig. 3.6).

5. The adsorption geometry of the CO molecule is assessed by scanning an area with physisorbed CO molecules again. Symmetrically adsorbed molecules lead to contrast inversion center within other surface-adsorbed CO molecules. The centeredness of this protrusion is compared to a database of "good" tips [77] (see Fig. 3.7). If the tip functionalization is insufficient, the CO can be removed via tip pulsing or controlled tip crashes into the surface.

Despite the successful application of this procedure, there is no guarantee of stable imaging for the duration of the scan, which lasts typically between 30 min and 5 h, depending on the size of the scan. At any time, the molecule can fall off the tip, adopt an asymmetric adsorption configuration, or collide with surface corrugations due to the disabled feedback control loop during constant height measurements. Typically, however, streaky STM imaging with a CO-terminated tip is a reliable forebode of unstable ncAFM imaging. Empirically, the success rate of reaching atomic resolution is about 30 %.

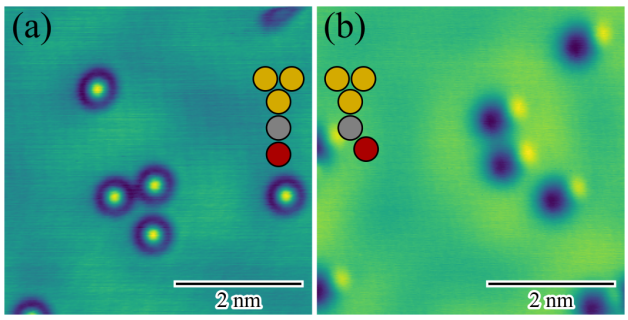

Figure 3.7: STM scans of CO molecules on Cu(1 1 1) with CO-decorated tip. (a) is indicative of a symmetric adsorption geometry of the tip-adsorbed CO molecule, while (b) shows a highly asymmetric adsorption geometry, unsuitable for CO-terminated high-resolution imaging. The cartoon insets schematically show the adsorption geometry. Imaging parameters: (a) $U = -300$ mV, $I_t = 50$ pA. (b) $U = -300$ mV, $I_t = 100$ pA.

3.3 Low Energy Electron Diffraction (LEED) and Auger Electron Spectroscopy (AES)

3.3.1 LEED

Low energy electron diffraction (LEED) is based on the quantum-mechanical wave-particle duality of the electron, as initally suggested by De Broglie and the principle of interference between two or more waves. A coherent monochromatic beam of electrons is aimed at a sample via magnetic lenses and the diffracted electrons collected with an electroluminescent collector plate. Electrons elastically scattered from the surface will constructively interfere only at specific locations on the collector plate with a symmetry pattern that is related to the crystal symmetry of the sample. From the diffraction pattern, the rotational symmetry of the 2DCP and it's alignment with the substrate, as well as the lattice constants of the polymer can be determined.

3.3.2 Auger electron spectroscopy (AES)

X-ray photoelectron spectroscopy (XPS) and, the less common Auger electron spectroscopy (AES) are two characterization tools that are, depending on the probing energy, generally considered to be non-destructive to the sample. The probe in XPS are x-ray photons, while in AES electrons are used. In both cases, the energy of ejected electrons from the samples is measured and can be used for chemical fingerprinting, i.e. retracing the chemical elements present in the material (XPS and AES), as well as bond nature of the constituents (XPS). The physical origin behind the signal in both is very different (XPS: photoelectric and AES: Auger effect), but both are based on inelastic scattering events of the probe beam with core-level electrons in the material, which leads to their

ejection with characteristic kinetic energies. As briefly mentioned above, the use of synchrotrons as very bright sources of x-rays has facilitated the real-time study of the growth of 2DCPs via *fast* XPS[14, 26], which contributes significantly to our understanding of the kinetics and reaction pathway of Ullmann coupling by monitoring the intensity fingerprinting bonds emergent in the reaction.

3.4 Sample Preparation and Synthesis of 2D Polymers

Three commercial bulk coinage metal single crystals (Cu, Ag and Au), as well as thin (200 nm) layer Au on mica, is in principle available as substrates for the synthesis of 2DCPs. However, since it has been shown that Au(1 1 1) is generally regarded as the most suitable surface for driving the assembly of 2D networks via Ullmann coupling [15] most synthesis, and experiments were performed using a Au(1 1 1) single crystal. All metal surfaces were grown and cut with the close-packing (1 1 1) surface exposed, as confirmed by low energy electron diffractograms, see Fig. 3.8.

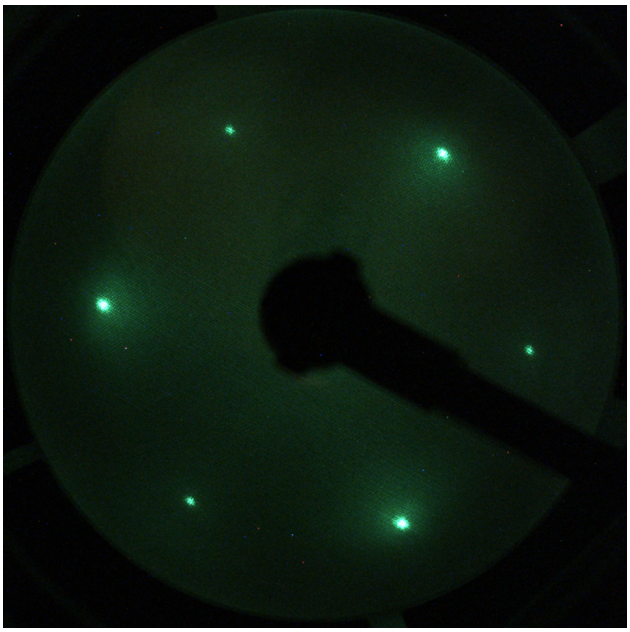

Figure 3.8: Typical low energy electron diffractogram recorded after sputter-annealing a Cu(1 1 1) single crystal. The hexagonal diffraction pattern reflects the close-packing arrangement of atoms in fcc (1 1 1) surfaces. The Diffractogram was recorded at a beam energy (E_B) of 120 eV and a beam current (I_B) of 40 mA.

Upon first introducing the samples, and prior to a new growth, the metal surfaces were treated by repeated cycles of sputtering with argon ions, followed by annealing to high temperatures. Depending on the surface contamination, two up to five sputter-anneal cycles were necessary to

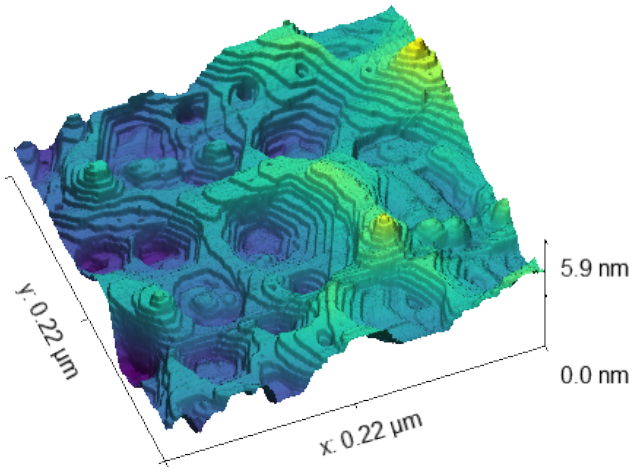

Figure 3.9: Three-dimensional render of STM scan of Au(1 1 1) after ion bombardment without the subsequent annealing step. Imaging parameters: $U = -500$ mV, $I_t = 50$ pA.

achieve a clean surface (as determined by AES) with large terraces on the order of several hundred nm. Obstinate surface contaminations could often reliably be removed by increasing the sample temperature to $200 - 350$ °C before initiating argon sputtering, termed *hot sputtering*. A typical cleaning procedure with three sputter-anneal cycles is shown in Table 3.1.

	Sputter Beam Energy (eV)	Sputter Duration (min)	Anneal Temperature (°C)	Anneal Duration (min)
#1	1000	10	450	10
#2	750	15	450	10
#3	750	10	500	10

Table 3.1: Simplified parameters for a three-cycle sputter-anneal process. The sputtering current collected by the whole sample plate assembly was kept constant at ≈ 4 μA.

The idea behind the chosen parameters is to start aggressively with high sputtering beam energies and shorter anneal times, and to end with mild sputtering and longer anneal times to allow for the sample surface to reorder and correct for sputtering damage (see Fig. 3.9). The anneal temperatures are chosen to be around $0.5 - 0.6$ of the melting point in degrees K[78].

The precursor species described in the next section are deposited on the substrates using a heated Knudsen cell. We utilize a commercial evaporator by Kentax with three cells for individual or simultaneous sublimation of organic materials up to 700 °C. A gate valve is used to isolate the evaporator from the preparation chamber, which allows for the evaporator to be removed and reattached without breaking vacuum in the preparation chamber. Crucibles containing the precursor material are warmed up to the deposition temperature prior to the deposition to allow for the equilibration of the crucible temperature and constant flux of species into the preparation chamber.

In *conventional* studies of on-surface synthesis of 2DCPs, the deposition step is often decoupled from the subsequent annealing step that induces the polymerization reaction. However, it has

been shown by Galeotti et al.[17] that a *hot dosing* approach, where the two steps are concurrent can reduce the defect density of the resulting nanostructure dramatically. This can be attributed to the fact that a third dimension is utilized, allowing monomers to access otherwise sterically hindered or unlikely-to-reach lattice sites within the growing network. All growths presented in this chapter follow the *hot dosing* approach, i.e. with the sample at elevated temperatures ($\approx 210^\circ$ C). The dosing lasted between 5 and 60 min, at a partial pressure of $P_{\text{TBTANG/TBTANGO}} = 5 \times 10^{-9}$ mbar, as recorded by an Bayard-Alpert Ion Gauge connected to the preparation chamber.

3.5 Precursors Investigated

The three-fold symmetric precursors tribromo trioxa-azatriangulene (TBTANG), and tribromo trioxo-azatriangulene (TBTANGO) are the focus of this work. Upon polymerization, these precursors arrange in two dimensions (P^2(TANG/TANGO)) into a Kagome lattice with hexagonal pores (named after a japanese bamboo basketing style, *kago* meaning basket, *me* meaning eyes, referring to the pattern of holes in a basket woven with this technique). Structurally, the precursors are oxygen-, or hydroxyl-bridged triphenylamines with bromine atoms as halogens, that cleave off in the Ullmann coupling reaction (see Fig. 3.10). The nitrogen heteroatoms serve as electron donors, while the bridge connections ensure the planarity of the molecules by preventing an out-of-plane rotation of the phenyls [5].

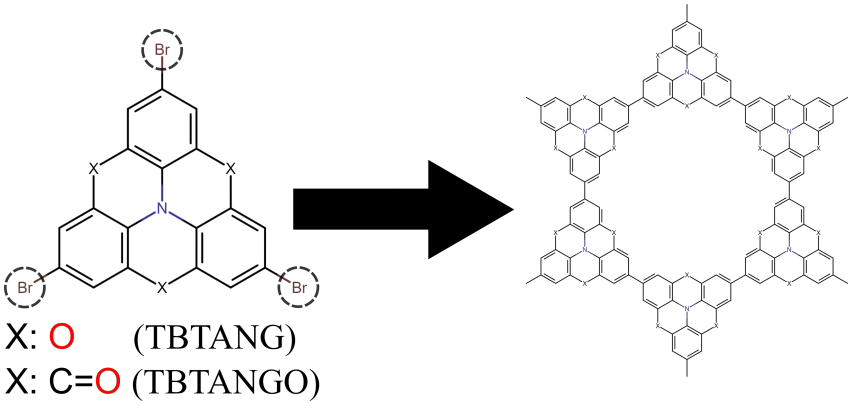

Figure 3.10: Brominated three-fold symmetric precursors TBTANG and TBTANGO polymerize into networks with hexagonal pores.

Chapter 4

Elucidating Reaction Kinetics and Edge Chemistry of 2D Polymers

In this chapter, a theoretical framework is presented for simulating the growth and network quality of 2D polymers, and compared to experimentally obtained networks of P^2(TANG)/Au(1 1 1) polymers. A comparative analysis of experimental, and simulated networks was used to gain insight into the relative energetic barriers of the kinetic steps in the reaction. The subsequent section presents a detailed study of the chemical nature of the edges of live 2D polymers. Evidence for the chemical identity of the terminations are discussed and compared with theoretical simulations from density functional theoretical models. Lastly, an efficient method for differentiating between isostructural molecular precursors in 2D block copolymer structures is briefly presented. With local density of states (LDOS) mapping at the flat conductive bands of the respective monopolymers, regions in the copolymer could easily be identified.

4.1 A Kinetic Monte Carlo Model to Simulate Polymer Synthesis in Two Dimensions

The parameter space associated with the formation of extended 2D covalent nanostructures is highly complex. To synthesize high quality graphene-like materials, it is important to have a detailed understanding of the kinetic reaction parameters that govern the on-surface polymerization reaction. Particular structural properties that need to be understood, are grain size, phase, as well as topological defects, point, and line defects, which heavily limit the effective size of the networks for technological applications. Experimentally identifying the key factors that control each attribute of the growing 2DCP is usually time-consuming. In order to overcome the experi-

mental difficulties, simulation techniques, like kinetic Monte Carlo methods, could help describe the atomic scale synthesis process of 2DCPs, and guide the design of precursors, or the exploration of new substrates for the synthesis of 2DCPs.

Indeed, Monte Carlo models have previously been used to explain certain aspects of surface-confined Ullmann coupling. Bieri et al. [15] used a simple MC model to explain the structure of polyphenylene polymers, synthesized from cyclohexa-m-phenylene macrocycles on different coinage metal $(1\,1\,1)$ surfaces (see also section 2.2.2). They found that the emerging structures could be understood from diffusion-limited aggregation (DLA) principles, where the coupling probability of their precursors, P_{coupling}, served to parametrize the system. Indeed, they discovered that the branched/fractal nature of the individual clusters could be traced back to the the relative rates, $r_{\text{c, d}}$, at which coupling and diffusion occur. Defining the coupling probability as $P_{\text{coupling}} = \frac{r_{\text{c}}}{r_{\text{c}}+r_{\text{d}}}$, they initialized a single seed molecule at the center of a hexagonal lattice. A single radical monomer species was subsequently initialized on the lattice edge, which was free to perform a random walk until reaching a coupling site. Depending on the coupling probability, the monomer subsequently couples, or back-diffuses, and continues until reaching another coupling site. Once the monomer coupled to the growing cluster, the next monomer was introduced, until an aggregation of 400 molecules was reached, at which point the simulation was terminated. This simple simulation showed structures bearing a striking resemblance to the topography observed in STM, and allowed the conclusion that on Cu$(1\,1\,1)$ diffusion is the rate-limiting process in the reaction ($r_{\text{c}} >> r_{\text{d}}$), while on Ag$(1\,1\,1)$ diffusion is enhanced compared to coupling ($r_{\text{d}} >> r_{\text{c}}$). Indeed, it has been noted by others before that the diffusion length (adhesion energy) of radical monomer species on Cu is so small (high) that nucleation often occurs homogeneously on terraces, as opposed to heterogeneously on surface defects, as often observed for Au, or Ag [79]. Vice versa, copper has also been shown to be more catalytically active, leading to comparatively lower energy barriers for the coupling reaction steps [39].

Another MC model was implemented by Eichhorn et al. [80] to explain the effect of substrate temperature, and dose rate, in direct (concurrent dosing and annealing), and hierarchal (step-wise dehalogenation, and covalent coupling via two anneal steps) polymerization of trigonal bi-brominated, mono-iodinated precursor species. To compare their MC simulations with experimental data, they identified the average pore coordination number (APCN), i.e. the average number of closed-pore neighbors per pore. Their simulated data suggests that for the direct approach, the APCN increases continually with the substrate temperature, which is not observed in experiments, where at higher temperatures, the increased density of topological defects limited the APCN. They rationalized this observation with an analogous observation common in solution chemistry: Namely, that early ring-closing reactions are mono-molecularly driven with an Arrhenius law and some energy barrier related to the molecular strain of the irregular pore, while regular

pores are bimolecularly driven with the participation of a lone nearby monomer. The temperature dependent occurrence of irregular pores, limiting the quality of the overall network has been observed by others as well [79, 17]. The discrepancy to their simulation in that regard is based on the fact that the occurrence of irregular pores was not allowed in their MC simulation.

While these models are capable of describing some kinetic aspects that lead to the observation of certain structures, other aspects are not addressed. More importantly, an important question that is not addressed is whether insight into the energetic values of the individual steps in the reaction can be obtained by comparing the experimentally observed structures to those observed in MC/kMC simulations. This model follows an object-oriented approach written in Python, and has mainly been written by the author. At time of writing, the model captures only the most rudimentary on-surface 2D polymerization chemistry. However, significant extensions are being made by Lex Rouquette, and Zach Charlesworth for their undergraduate theses under the author's supervision.

4.1.1 Model Description

Kinetic Monte Carlo (kMC) methods provide a means for exploring kinetic systems transition from one state to the next via a stochastic process. Specifically, kMC models randomly choose an *event* from a catalogue of possible events, according to particular rates of the transitions [81]. For thermally activated transitions, like diffusion, one typically describes the rate of incidence, r, for each event with an Arrhenius equation

$$r_i = \nu_{0,i} \exp\left(-\frac{E_i}{k_\mathrm{B}T}\right). \tag{4.1}$$

ν_0 is the frequency with which the particular event is attempted, typically $\nu_0 \sim 10^{12} - 10^{14}$ Hz for lattice vibrational driven dynamics. E_i is the associated energy barrier, which is compared to the thermal energy $k_\mathrm{B}T$ with Boltzmann constant, k_B, and temperature, T. It's important to note, that the the rate of each event is dependent on the local environment of each constituent, and typically, several events can occur with identical rates, i.e. a monomer with six equivalent, unoccupied, neighbouring lattice sites can diffuse to any one of these with equal probability. Anisotropic diffusion due to interactions of single species with their local environments can be implemented by utilizing different energy barriers for different crystallographic/lattice site directions. The kinetic transitions accessible to the system at every timestep of the simulation are diffusion, rotation, and coupling of each monomer on the lattice, provided these actions are possible (see Fig. 4.1).

The model adopts a fcc $(1\,1\,1)$ surface, with a hexagonal arrangement of lattice sites, each associated with a unique pair of natural numbers (n, m). Threefold symmetric radical monomer

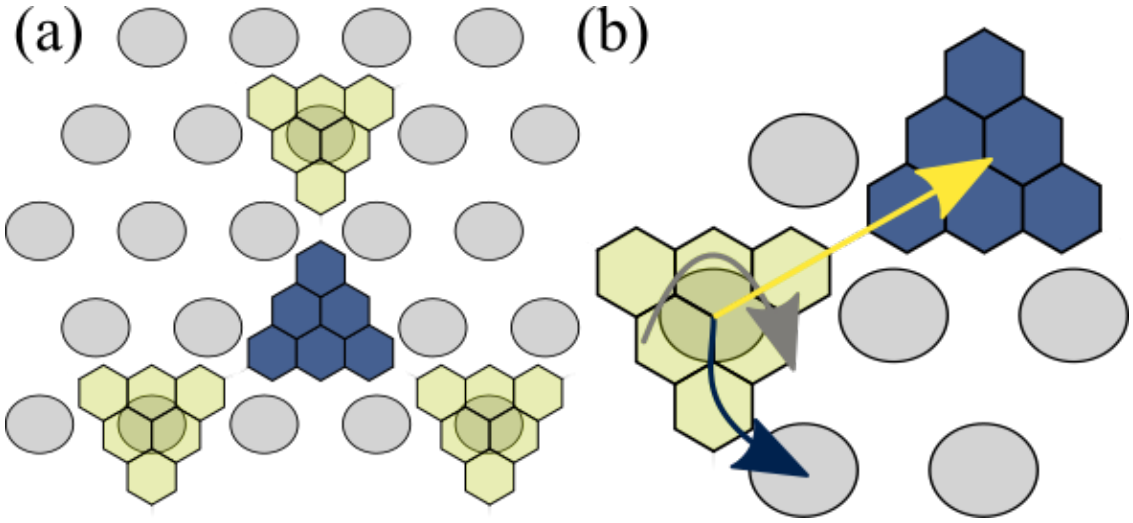

Figure 4.1: Kinetic Transitions and Setup of the kMC Model. (a) A hexagonal arrangement of lattice sites serves as geometrical foundation. Coupling is only enabled if the orientation and positioning of the participating molecules is in agreement with the Kagome symmetry of the full network. (b) Three kinetic transitions are implemented with different rate constants, r_i: Diffusion (Blue Arrow), Rotation (Grey Arrow), and Coupling (Yellow Arrow).

species are populated at random positions on the lattice. The system dynamics are then propagated with the following recipe [82, 81]

1. A random number $\rho_1 \in U[0,1)$ is drawn from the uniform distribution U. This stochastically selects an event according to

$$\sum_{i=1}^{m-1} r_i \leq \rho_1 \sum_{j=1}^{N} r_i < \sum_{k=1}^{m} r_k. \tag{4.2}$$

   In eqn. 4.2, m is the index corresponding to the chosen event, N is the total number of events of the entire system, i.e. the number of possible transitions the system can undergo, and i, j, and k are summation indices. This inequality ensures that events with a larger rate are chosen more frequently by the algorithm, as compared to those with a lower rate.

2. A second random number, $\rho_2 \in U[0,1)$ is chosen, and the simulation time is advanced according to Poisson statistics

$$\Delta t = -\frac{\ln(\rho_2)}{\sum_{i=1}^{N} r_i}, \tag{4.3}$$

   where Δt is the elapsed time between the previous event and the currently executed event. This can be seen as the average time between transitions in the system.

3. Upon executing the chosen event, the event catalogue is updated based on the new state of the system, and the event rates recalculated.

It should be noted, that topological defects cannot occur in this model as of now, i.e. coupled monomers are not allowed to rotate. Furthermore, coupled monomers are no longer mobile. Certainly a simplification, but not an uncommon one, as this has also been implemented in [80]. The physicality of this assumption needs to be critically examined, and certainly changes at elevated temperatures, where even dimers, trimers, or small oligomers should be allowed to diffuse.

4.1.2 Network Quality Dependence on Energetic Barriers

To benchmark the model, the above-described situation investigated by Bieri et al. [15] is modeled in the kMC approach: A single seed molecule is initialized on a hexagonal lattice with 100 $\times$ 100 lattice sites. Monomers are sequentially introduced on random positions of the lattice, and allowed to complete a random walk until 400 monomers have agglomerated to the seed. A principal difference between the two approaches, is that in the kMC approach used here, monomers have an orientation on the lattice, with coupling only being possible for two monomers whose reactive arms are collinearly aligned. To compare the results from this model to those from Bieri et al., an intermediate value of the rotational energetic barrier was chosen, while coupling, and diffusion barriers were set to vastly different values, such that the coupling probability, $P = r_c/(r_d + r_r + r_c)$, assumes similar values as in the simulations shown by Bieri et al.[15].

It is readily observed, that the shown networks exhibit different degrees of branchedness, or fractal order. These qualitative results agree well with those found by Bieri et al. [16]. To quantify the quality of these networks, a coordination number histogram is extracted. It has often been stated that Monte Carlo models serve primarily as a qualitative tool for qualitative explanations the quality of grown 2D networks [26, 5]. However, for simple systems and only a small number of possible transitions between thermodynamic states, it should be possible to extract energy barriers through a comparative analysis of the network quality of experimental data and data simulated for a range of different energy barriers for the set of kinetic transitions considered. For this purpose, a python-based network quality classification workflow (NQCW) has been developed, with the basic analysis pipeline showcased in Fig. 4.3 and described in the following:

1. Small oligomeric islands with ~ 60 individual monomer units are identified in STM Δz maps. These maps are converted into grayscale images.

2. A skeletonization algorithm from the python package `scikit-image` [83] makes successive passes over the image, removing pixels from the boundary of the network each iteration with-

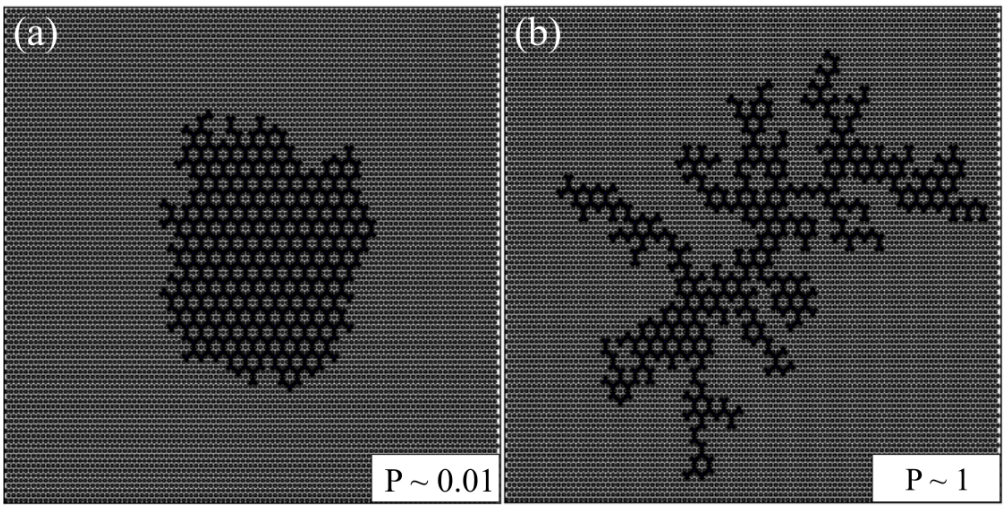

Figure 4.2: Simulated networks with the kMC approach. A single seed molecule is initialized on the lattice, and monomers added upon completing a random walk until a total of 100 monomers have coupled to the growing cluster. This highlights the interplay of Diffusion and Coupling for the 2D network quality. (a) Represents a process in which coupling is rate-limiting to the reaction, while diffusion is rate-limiting in (b).

out breaking the connectivity of the underlying topology, until a two-dimensional boolean (`True`/`False`) matrix remains that classifies pixels in terms of their affiliation to the network.

3. The skeleton is then passed through a script that checks the 8-pixel nearest neighbors of all pixels belonging to the skeleton. If, for a pixel, two or more neighbors are also part of the skeleton, it is classified as a `node`, and added to a `Graph` object (see the `networkx` package [84]). The connectivity of a node is then computed by tracing out all paths on the skeleton from itself to other nodes. A stopping condition is applied, once another node is encountered. Subsequently, the two nodes are connected via an `edge` inside the `Graph` object. Note, that these edges are not necessarily part of the skeleton matrix. Instead, they are the shortest euclidian distance between two nodes (see Fig. 4.3).

4. The `Graph` object is subsequently returned for further analysis. From this classification, the coordination of the nodes in the `Graph` are taken to be representative of the coordination of the monomers in the 2D network.

With this workflow, a large number of 2D networks can be efficiently analysed, and compared to simulated ones from the kMC model. With this approach, 10 islands, each with 60 ± 20 monomers have been identified. Following this, kMC simulations are performed. A range of expected energy barriers (E_c, E_r, and E_d) is defined, and each range iterated over, such that a list of energy triplets is passed as input to the kMC model. For each energy triplet, 10 simulations are

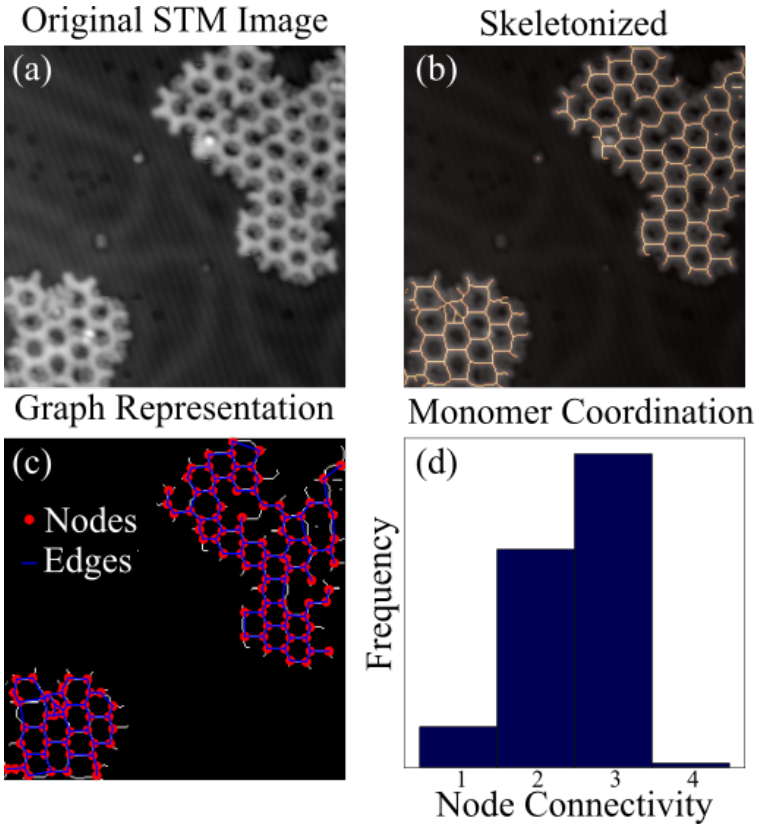

Figure 4.3: Workflow to Extract Network Quality from Experimental STM Images. (a) Exemplary STM Image in gray-scale. (b) Extracted skeletonization of the 2D network drawn over STM image. (c) Graph Representation of the skeletonized network, where nodes are assumed to be Monomers, while edges represent the linkages between individiual units. (d) Histogram of the computed node connectivity from the graph representation. This is taken to be approximately equal to the monomer coordination in the following.

performed for averaging purposes. The average coordination number frequencies are then readily calculated and collected in a histogram. The simulations are executed with a sample temperature of 210° C, and with a uniform attempt frequency for the three transitions, i.e. $\nu_0 = 10^{13}$ Hz.

These results are then compared to the results from the NQCW for the experimental images, and a similarity score assigned. The similarity score is based on the likeness of the coordination histogram. The experimental and simulated histograms are compared using the Wasserstein metric, also known as Earth mover's distance [85, 86]. The Wasserstein metric can be intuitively understood by envisioning two distributions as piles of soil. The metric quantifies the minimal amount of work needed to transform one pile into the other, i.e. the amount of soil that needs to be moved times the distance it needs to move. Hence, good agreement between two histograms implies a low Wasserstein metric. It's definition can be found in the Appendix B. It represents a transport problem, that, while not having an analytical solution can be computationally determined. Keeping

one of the three energies constant, the Wasserstein distance between the experimental islands and the simulations can be shown as a 2D contour map. Some exemplary contour plots are shown in Fig 4.4. It can be seen that several minima in the contour maps emerge for different combinations of the three energetic barriers. This indicates that the combination of barriers for achieving a given experimental network quality is not unique. However, knowing one of the energetic barriers, it might be possible to predict the others by performing kMC simulations in the parameter space neighborhood to the known barrier.

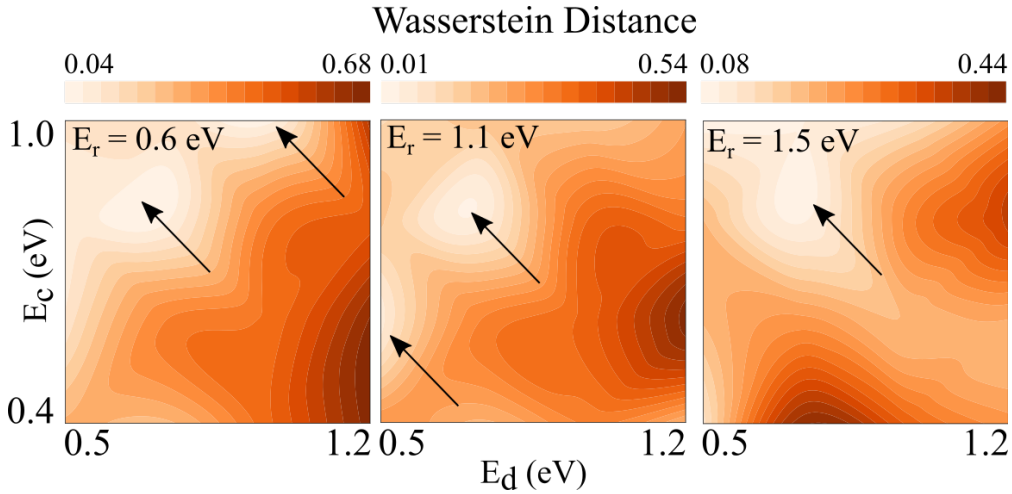

Figure 4.4: 2D Contours of the Wasserstein matrix for different slices of the rotational energy barrier. As expected, the monomers are predicted to exhibit a large coupling/low diffusion barrier. However, several minima (indicated by arrows) in the Wasserstein distance indicate that the combination of energetic barriers is not unique.

For systems with several transitions with vastly different associated rates, the model spends a lot of time executing transitions with low energetic barriers, which, while physically accurate, is computationally burdening. This issue is well-known as *timescale disparity problem*, and dynamic time-propagation algorithms are the subject of active research [82]. To explore the parameter space spanned by the Wasserstein metric in more detail, a more sophisticated time-propagation algorithm needs to be implemented for this model, as one is currently constrained to investigate systems whose kinetic rate transitions are within one or two orders of magnitude of each other.

4.1.3 Conclusion

In this chapter, a simple kinetic Monte Carlo model for simulating the synthesis of 2D polymers is presented, and compared to recorded STM images of experimentally synthesized P^2(TANG)/Au(1 1 1) islands. The experimental, as well as theoretical extraction of energy barriers for kinetic transitions, such as diffusion, rotation, and coupling proves to be difficult. In this chapter, the extraction of

these parameters by comparing the network quality from kMC models with experimental networks has been shown as proof-of-principle. To improve the quality of the extracted parameters, an improved time-propagation algorithm needs to be implemented. Additionally, it should be kept in mind, that this model simplifies the complexity of the kinetic rates of the actual on-surface chemistry, and that further additions to the model are necessary to describe the growth of 2D polymers with higher accuracy. Importantly, the model does not take non-covalent intermolecular interactions into account, which are known for driving the self-assembly of single molecules on surfaces. Additionally, since non-ideal pores are not allowed to exist, the model necessarily over-idealizes the resulting network structure.

4.2 The Role of Edge Terminations of Active 2D Polymers

The controlled assembly of 1D and 2D organic molecular structures is crucial for device fabrication [19]. Since Grill et al. [45] demonstrated the controlled covalent assembly of 2D networks via on-surface Ullmann coupling, much progress has been made in understanding the full pathway of the Ullmann coupling reaction. Ullmann coupling involves two steps, the homolytic scission of C−X bonds (X = halogen), and the coupling of adsorbed radicals to form covalent C−C bonds, potentially via a metal bridge atom forming organometallic C−M−C (M = metal) intermediate states. These states typically incorporate a surface atom, but metal adatoms have been observed as well [87, 55, 75], particularly at step edges, or defect sites, where the occurrence of adatoms is naturally high. Molecules coordinating to a surface atom generally exhibit a tilted adsorption geometry, while adatom-coordinated molecules may adopt a planar, or nearly planar adsorption geometry. A spectrum of hybrid geometries exists depending on the interaction with the unsaturated molecule(s). This can lead to subtle differences in the precise positioning of the metal atom with respect to the molecular plane. Theoretical studies, such as Zhang et al.'s work on bromobenzene on Cu, Ag, Au$(1\,1\,1)$ surfaces, revealed that the coordination of two unsaturated molecules to a surface atom can displace the atom from it's lattice site, effectively creating a vacancy [87]. Experimentally, this behaviour was confirmed by Zint et al. [75] for mono-halogenated bromotriphenylene on Cu$(1\,1\,1)$. Their work demonstrated that CO-terminated ncAFM allowed them to distinguish between adsorption geometries expected from C−M−C coordination upon comparison with expected relaxed atomic configurations based on density functional theoretical (DFT) simulations. Notably, deviations from planar adsorption of organic molecules significantly alter the contrast in CO-terminated ncAFM images, as the tip-sample interaction is highly sensitive to small changes in the tip-sample separation due to local conformational differences. This represents an important distinction to STM, which is principally sensitive to the local density of states at the Fermi level. Sample features that are visible in STM Δz maps can be absent, or appear with

inverted contrast in CO-terminated ncAFM Δf maps of the same sample region. An important example to highlight this point is given in the aforementioned study by Zint et al.. They observed that the C−M−C linkage of the organometallic intermediate led to a bright round feature between the monomers in STM images, and a line feature in CO-terminated ncAFM images. Dosing TB-TANG/TBTANGO on Cu(1 1 1), kept at 210° C, can be seen to lead to similar STM contrast with visible round protrusions between the involved monomers (see Fig. 4.5).

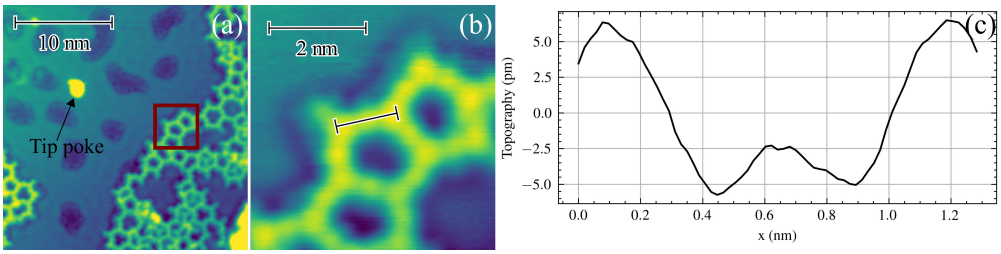

Figure 4.5: Organometallic Intermediary Formation on Cu (1 1 1). (a) 30×30 nm^2 STM image of P^2(TANGO) at ∼ 50% coverage shows disordered film. The dark islands are self-assembled, close-packing CO molecules that have adsorbed in the sample transfer process. The bright protrusion, labeled *Tip poke*, shows an artifact from a controlled collision of the tip with the sample surface. Due to the metal coordination, the strain energy penalty for forming non-ideal pores is low, leading to a predominantly 5-membered ring formation. (b) Close-up, with line profile drawn between two monomer units. (c) Protrusion between two monomers reveals metal coordination, instead of covalent bond formation. Imaging parameters: $U = -500$ mV, $I_t = 50$ pA.

Despite significant progress in understanding Ullmann coupling, the mechanism of polymerization at the grain boundary of actively growing 2D polymers remains unclear. Small differences in the energetics of reaction intermediates and barriers between all transitional steps in the reaction can lead to vastly different reaction pathways [87] on different substrates. The prevailing scientific consensus is that radical monomers are, again, primarily stabilized by surface atoms, and in some cases by surface adatoms. However, an alternative possibility is the termination of active edges with residual gases in the UHV environment. This would likely have adverse effects on the chemical activity of live edges of the growing polymer. In the following, we investigate the edge terminations of small P^2(TANG) oligomers on Au(1 1 1) after the polymerization reaction with a combination of STM, CO-terminated ncAFM, and DFT.

4.2.1 CO-terminated Measurements

Single CO molecules are picked up with the tip in STM mode, and the symmetric adsorption of the molecule verified according to section 3.2.2. Prior to constant height measurements, the surface is *leveled* over a flat, and clean region of the sample with an arbitrary Δf setpoint. This level defines the reference plane to all subsequent constant-height scans, i.e. first-order corrections

(dz/dx and dz/dy) to the z-piezoelectric extension as the tip moves across the surface. Despite this procedure, small amounts of drift in the z-piezoelectric could still be observed, moving the tip towards the surface during the constant-height scans performed here, at a rate of $dz/dt \sim 15$ pm/h. In principle, this can be accounted for, but was not done for the scans presented in the following. The experimental CO-terminated ncAFM images shown in the following lasted between 45 min., and 5 h.

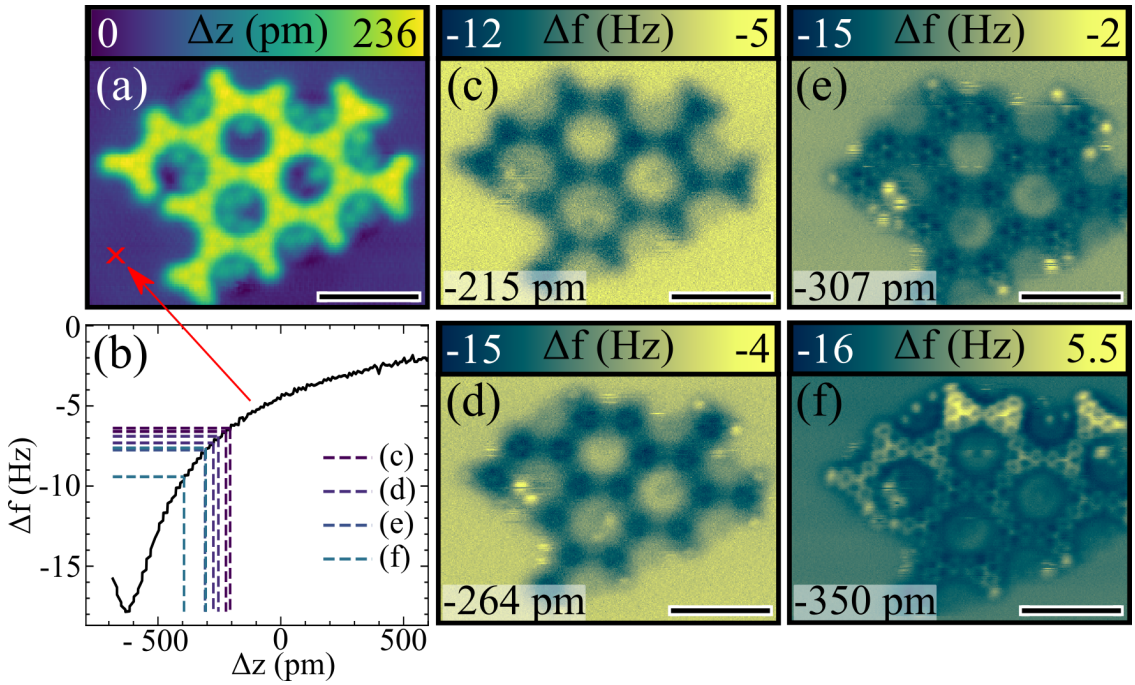

Figure 4.6: P^2(TANG)/Au(1 1 1) Contrast Formation as a function of tip-sample separation. (a) STM Image with CO-decorated tip. (b) Δf spectroscopy above the Au(1 1 1) surface. (c - f): Constant-Height Δf maps at different Δz offsets w.r.t. a sepoint of $\Delta f = -4.5$ Hz defined at the position marked with a red cross in (a). Acquitision of (f) lasted 5 h and was recorded from bottom to top of the scan frame, leading to modified contrast (dark, faint features to bright, well-resolved features) along the slow scan direction. Imaging Parameters: (a) $U = -300$ mV, $I_t = 50$ pA. (b - f) $A = 55$ pm, $Q = 190,000$. Scale Bars: 2 nm.

The topography of a small oligomer of P^2(TANG) on Au(1 1 1) recorded in constant-current STM mode with a CO molecule decorating the tip is shown in Fig. 4.6(a). The three-fold symmetry of the monomer units, as well as round protrusions, clustering inside the pores and around the island can be seen. These protrusions have previously been linked to residual halogens that remain close to the original location of dehalogenation due to a large adhesion energy of the halogens to metal surface atoms [15, 88]. As a consequence they can become trapped inside the pores during ring-closing coupling reactions.

Fig. 4.6(c)-(f) shows a stack of Δf maps at decreasing tip-sample separations with respect to

an arbitrary Δf setpoint of $\Delta f = -4.5$ Hz (measured above the gold surface, indicated by the red arrow). As the tip is moved closer to the molecular plane, the dangling CO molecule relaxes in the local potential energy surface into energetic minima, slipping off saddle point ridges formed by interatomic bonds. This has the effect of sharpening these features in the Δf map [68]. At closer approach distances, strong repulsive forces set in leading to an inversion of contrast due to the non-monotonic nature of the $\Delta f(z)$ curve (see Fig. 4.6 (b)) .

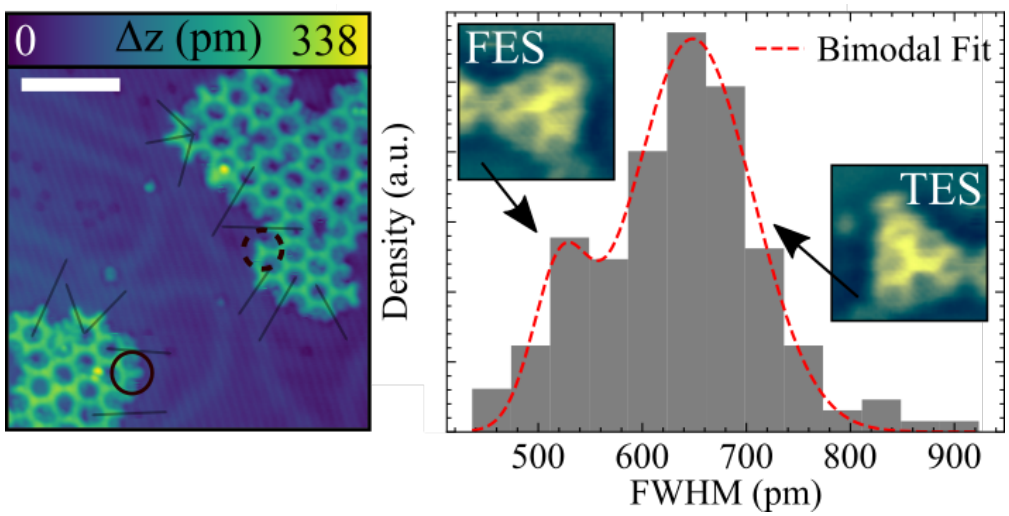

Figure 4.7: Statistical analysis of molecular bond lengths based on 273 measurements from 20 STM images. The histogram on the right shows the distribution of full-width at half-maximum (FWHM) values extracted from line profiles, marked by the opaque lines in the exemplary STM image on the left. For clarity, potential FES, and TES are marked with dashed, and solid circles, respectively. The data were fit with two normal distributions to model the bimodal character of the bond lengths. The extracted ratio of FES to TES is approximately 1:11. Imaging Parameters: $U = -500$ mV, $I_t = 50$ pA. Scale bar: 10 nm.

Strikingly, the monomers that form the boundary of the oligomer seem to exhibit two types of terminations. Most of the exposed edges of the oligomer show a bright feature (in the following referred to as TES (=terminated edge state)), that is well correlated with longer protrusions at corresponding locations in the STM image. Less commonly, the rest of the edges on the boundary of the oligomer show a lack of this feature (FES (=feature-free edge state)). Indeed, a statistical analysis of 273 edge monomers shows that the ratio of FES to TES is approximately 1:11 (see Fig 4.7). Additionally, the Δf maps show round features in the pores, and around the oligomer, as well, however, appearing at different positions than the previously as halogens identified features, in the STM image. The side-by-side comparison of STM, and CO-terminated ncAFM maps implies that indeed the dark halo features inside the pores, and around the cluster should be identified as the halogens remaining on the sample surface, and not the bright, round protrusions. This will be readdressed in the next section.

While the discussed drift in z-piezo extension could in principle compensate for the effect of a bending molecule in Fig. 4.6 (f) at the FESs, the lack of molecular bending towards the surface could also be seen in other constant-height scans, where the edge is perpendicular to the slow scan direction (see Fig. 4.11) with minimal z-piezo drift during the acquisition of the linescans. Furthermore, the oval shape of the protrusions suggests that the TES remained halogenated during the anneal process. Indeed, as was shown by Tschakert et al. [89], halogen atoms exhibit a strong asymmetry in CO-terminated images which is associated with the strongly directional σ bond. However, this represents merely a general rule, and is not strictly true in all situations. To better understand the contrast formation, and to answer the raised questions, density functional theory simulations were performed and are presented in the next section.

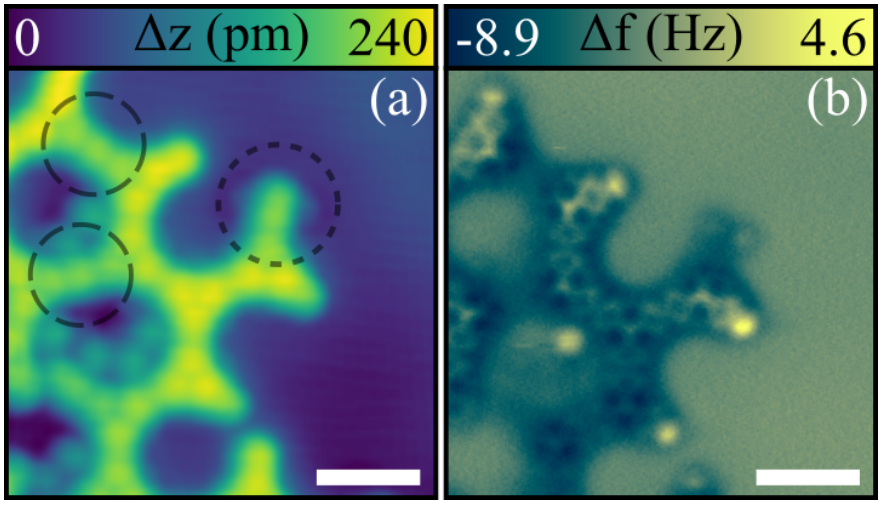

Figure 4.8: Highly defective region of P^2(TANG)/Au(1 1 1). (a) STM Δz map shows elongated bond lengths between some of the units in the network (long-dashed circles) with a bright protrusion in-between indicating an OM linkage. A third termination, unlike the previously described TES, and FES, of an exposed edge monomer is highlighted with a short-dashed circle. (b) CO-terminated ncAFM Δf map reveals significant bending of the metallically coordinated phenyl groups. Likewise, significant bending can be observed at the termination site, accompanied by faintly repulsive round features. Imaging Parameters: (a) $U = -300$ mV, $I_t = 50$ pA. (b) $A = 55$ pm, $Q = 190,000$. Scale bars: 1 nm.

As discussed, OM intermediates are a rare occasion on Au(1 1 1). Due to the intermolecular metal atom, they can, however, readily be identified using STM for their elongated molecular bond length. Fig. 4.8 shows an STM Δz map side-by-side to a CO-terminated ncAFM Δf map of a highly defective region at the edge of an oligomeric cluster. Two C−M−C linkages are indicated by long-dashed circles, showing bright protrusions between the monomers. The ncAFM images exhibit a totally different contrast, where the linkage between the partaking monomers almost disappears completely. Within the monomer units, the phenyl groups neighboring this

linkage appear significantly darker/fainter than their covalently bonded counterparts. Additionally, the TES phenyl groups appear brighter, which matches the observations made in Fig. 4.6. This indicates that the organometalically coordinated phenyl groups experience a tilt towards the surface. The larger, short-dashed circle in (a) highlights another noteworthy observation: The observed termination corresponds to neither the described FES, nor TES states. In STM, the elongated termination presents itself to be slightly asymmetric, with faint features perpendicular to the linkage. In (b), the monomer can again be seen to tilt towards the surface, and furthermore, two slightly repulsive features faintly stand out against the background. This is most likely the proposed dehalogenated/metalically-coordinated termination, since a bending of the molecule is expected for this type of termination. Due to it's similar appearance to TES in STM, CO-terminated ncAFM might be necessary to distinguish between them. It should be noted that around 30 edges were imaged with CO-terminated ncAFM, and this is the only example of this termination.

4.2.2 Comparison with Density Functional Theory (DFT)

In collaboration with Shuaishuai Yuan (McGill University), we have conducted spin-polarized calculations using the Vienna Ab initio Simulation Package (VASP) with the projector-augmented wave (PAW) method and an energy cutoff of 800 eV. The calculations employed the Perdew–Burke–Ernzerhof (PBE) generalized-gradient approximation (GGA). Van der Waals interactions were accounted for using the zero-damping DFT-D3 method of Grimme et al. [90]. The Au$(1\,1\,1)$ surface was modeled using a slab consisting of four atomic layers, each containing 12×12 atoms, with the bottom two layers fixed to mimic bulk conditions. A $3 \times 3 \times 1$ k-mesh was applied for geometry optimizations. We relaxed the geometries of the molecule and the first two layers of the slab using a conjugate-gradient algorithm until the forces were less than 0.02 eV/Å. Total energies were converged better than 10^{-5} eV in self-consistent field (SCF) cycles during geometry optimization.

Single TANG monomers were placed on the top slab with their orientation and adsorption height based on previous DFT simulations of P^2(TANG) polymers on Au$(1\,1\,1)$ conducted by Oliver Maclean [17]. To simulate the influence of a connected polymer cluster, two of the three-fold symmetric precursor's corner C atoms were fixed during relaxation. To model the contrast resulting in TES, a Br atom or an Au-adatom was introduced at typical bond length distances ($a_{\text{Br-C(aromatic)}} = 189$ pm [91], $a_{\text{Au-C(aromatic)}} = 195$pm [92]) to the exposed corner C atom within the molecular plane.

The relaxed geometries are shown in Fig. 4.9. The single-brominated molecule experiences a slight bending of the exposed edge towards the substrate, with the central N atom protrusion a distance $d_{\text{N,Au}} = 346$ pm, the fixed C atoms distances of $d_{\text{C,Au}} = 333$ pm, and the exposed C atom a distance of $d_{\text{C,Au}} = 320$ pm above the first gold layer. The Br is physisorbed at a distance

$d_{\mathrm{Br,Au}} = 310$ pm, resulting in a downward tilt angle between the N center and the Br of $\sim 3.4°$. The slight convexity is also seen in the adsorption of 2D sheets of P^2(TANG)/Au(1 1 1), where N is similarly exposed with $d_{\mathrm{N,Au}} = 345$ pm above the topomost substrate layer [17].

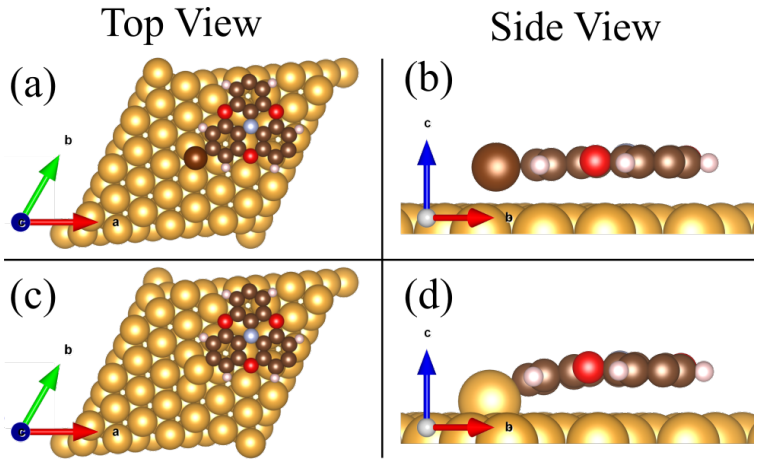

Figure 4.9: DFT Optimized Geometries for two potential candidates of the TES termination identity. (a, b): The edge TANG molecule with a protruding bromine atom on the Au(1 1 1) surface with adsorption geometry based on the LEED pattern in Galeotti et al. [17]. (c, d): The Au adatom-coordinated TANG molecule, exhibiting significant bending, primarily in the protruding phenyl group.

The Au adatom terminated geometry experiences significant bending towards the substrate, particularly of the adjacent phenyl group. The central N atom is predicted to lift up even more strongly due to this bending to $d_{\mathrm{N,Au}} = 352$ pm. The Au adatom relaxed into a hollow site on the surface with an average distance to it's nearest neighbors of 275 pm, which is lower than the Au-Au bulk, and surface bond lengths (295 pm, and 289 pm, respectively). This leads to a strong distortion of the vicinal substrate. The metallically-coordinated C sits a distance of $d_{\mathrm{C,Au}} = 293$ pm from the topmost layer of the substrate, nearly 30 pm closer to the substrate than the same C in the single brominated case. The exposed phenyl group tilts towards the surface with a tilt angle of $\sim 8.93°$ with respect to the substrate normal. A strong bending of dehalogenated molecules is expected, regardless of the termination of the exposed C atom with a surface atom, or metal adatom [39, 75]. To complete the picture, it is important to model a dehalogenated molecule whose exposed C atom coordinates with a surface atom, which is expected to induce even greater bending. Additional DFT simulations are also required to better understand how the geometry of the Au adatom-terminated case changes depending on the adsorption site. Notably, a slight asymmetry in the adsorption heights of the flanking O atoms (350 pm vs. 335 pm) suggests that this distortion results from the chosen adsorption geometry and constraints imposed during relaxation on the two C atoms assumed to form covalent C−C bonds with the rest of the polymer.

Simulations of the contrast formation based on the presented DFT data were done using *Probe-*

Particle AFM (ppafm), a widespread open-source tool developed by Hapala et al. [68, 93, 94]. In the model, a single spherical particle (e.g. the O atom in a CO molecule - the probe particle) attached to the tip by a spring moves in the local tip-sample potential, and relaxes into low energy configurations during the oscillation, thereby effectively sharpening saddlepoints and ridges in the potential energy landscape (see section 3.2.3). In the simplest form, the motion of the probe is primarily calculated with a pairwise Lennard-Jones potential, based on the atomic positions of the sample in 3D space. Despite it's simplicity, this form of the model can already predict the contrast in ncAFM images with astonishing accuracy. A more sophisticated approach is to supply the Hartree electrostatic potential, that can be calculated with DFT from the relaxed geometrical structure, instead of relying on point-charge electrostatics. This approach was followed in the following simulations. The highest degree of accuracy can be obtained using the full-density based model (FDBM), capable of capturing electron density reorganization inside molecules during the motion of the probe particle [94].

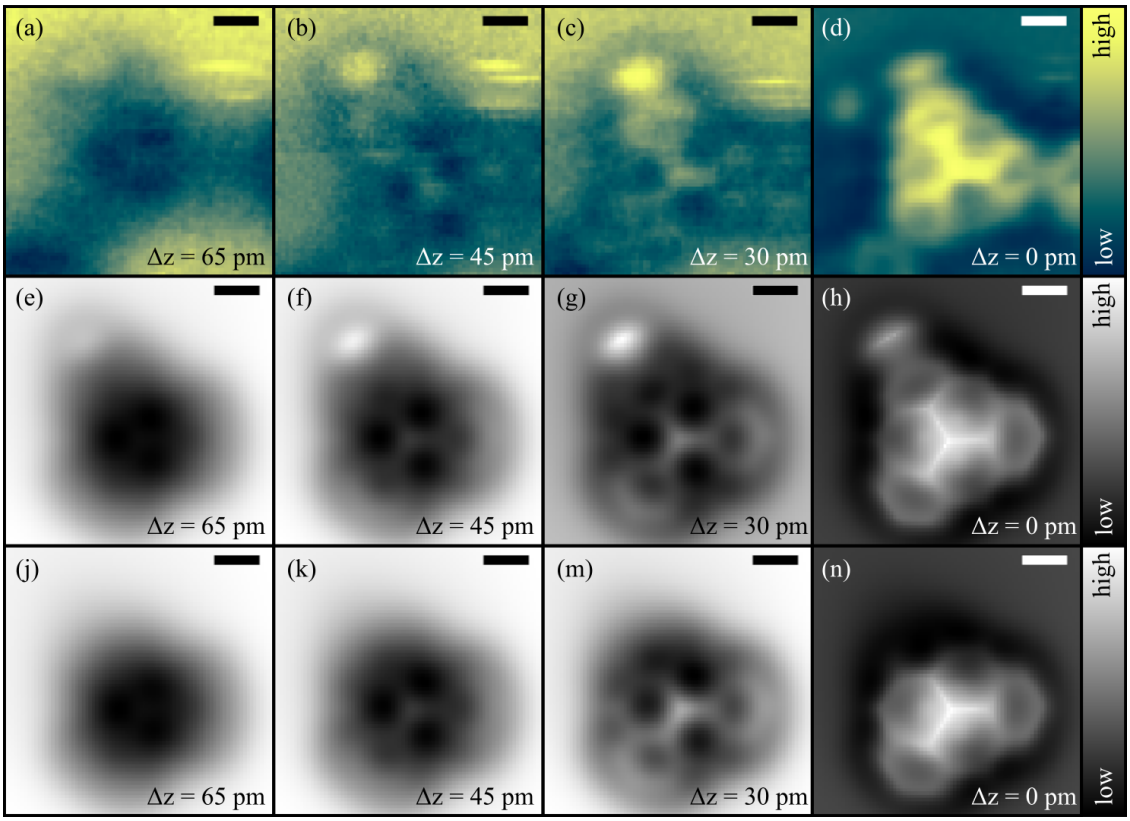

Figure 4.10: Potential identities of terminations of TES. (a-d): Shows a stack of experimental CO-terminated ncAFM images. A 2×2 Gaussian kernel was applied to reduce noise artifacts. (e-h): Contrast Formation modeled for brominated molecules. (j-n): Contrast Formation for molecules coordinated with a Au adatom. The specified height, Δz refers to the lowest approach distance in in each row for clarity. Imaging Parameters: $A = 55$ pm, $Q = 190,000$. Modeling parameters given in text. Scale bars: 200pm.

The probe particle was modeled with typical parameters [94] assuming a quadrupole moment of the CO molecule of -0.1 e $\times$ Å^2, with a probe charge distribution width of 71 pm. Simulated images were obtained by laterally scanning this probe with a step size of 0.2 Å above the sample. At each lateral position, the probe is approached towards the sample in steps of 0.1Å and allowed to relax. Following relaxation at each step, the vertical component of the force exerted on the probe by the sample was calculated and subsequently converted into Δf values, via eq. 3.2. The obtained Δf maps are compared to experimental images in Fig. 4.10. The agreement between the stack of experimental data, and the brominated TANG molecule data is significantly better than for the Au adatom-coordinated molecule. Notably, the evolution of contrast from a spherical to an ellipsoidal shape for the bromine atom closely matches the development of contrast for the protruding termination in the experimental data. Furthermore, the N atom leads to a bright feature in the center of the molecule in both models. This is attributed to it's lifted adsorption geometry, despite the lower van der Waals radius as compared to C [95].

In Fig. 4.10(c), as well as in Fig. 4.8(b), the exposed phenyl group appears slightly brighter than it's coupled counterparts at the bottom of the image. This is reversed to the simulation in Fig. 4.10(g). This discrepancy might imply a lifted geometry, which was not predicted by DFT for either of the two investigated scenarios for TES. This might be rationalized by the following: The DFT model discussed for the TES here has limited applicability with orientation and adsorption position fixed, according to previous studies of P^2(TANG)/Au$(1\,1\,1)$. The adsorption geometry (orientation, position, and height) is not necessarily the same for oligomers. Particularly, the lattices of the polymer network, and the Au surface are not commensurate. Hence, this disagreement could be ironed out once other adsorption geometries for mono-brominated TANG molecules are simulated with DFT. Additionally, the simulations performed here include only a single monomer, and neglect intermolecular interactions with the rest of the polymer. A polymeric sheet with extended π-conjugation might interact very strongly with the d orbitals of the underlying gold surface, and thus adhere much closer to it than the halogenated phenyl groups, which subsequently appear with higher contrast by comparison.

Line profiles extracted along the molecular backbone onto the protrusion for brominated TANG edges, and the experimental data are compared in Fig. 4.11. Peak positions in the line profile corresponding to N, and X termination appear at similar positions in the profile with a small feature on the trailing end corresponding to the bridging O atom. The primary peaks of both Δf maps experience pronounced asymmetries, manifesting as broad shoulders in the experimental map.

The chemical identification for the featureless edge states (FES) is more difficult. Most likely, they are radical sites that are only weakly bending towards the surface, as suggested by Zint et al. [75] for species with similar contrast. It has been suggested that the radical sites could become hydrogenated via residual gases in the UHV environment. However, while gas phase simulations

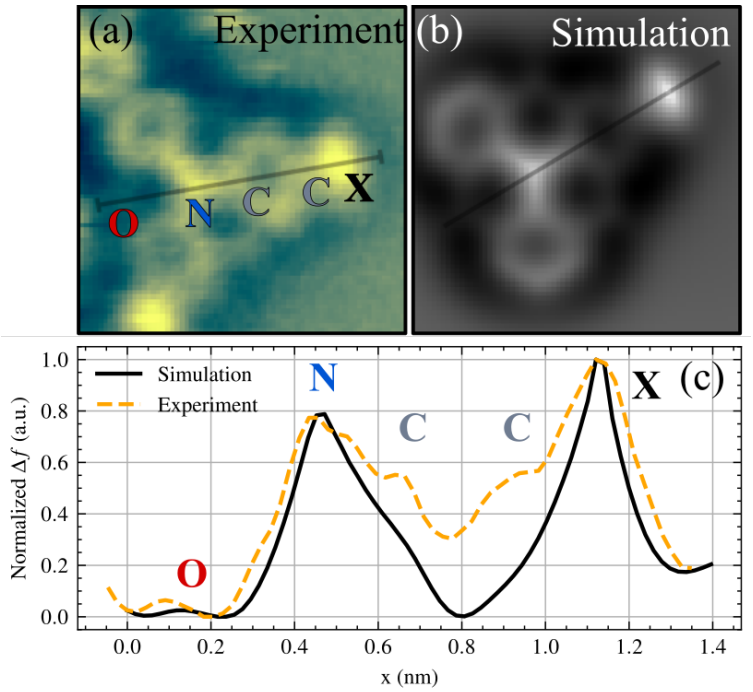

Figure 4.11: Comparison between experimental and simulated contrast of TES for Br-terminated TANG. Imaging Parameters: $A = 55$ pm, $Q = 190,000$.

of hydrogenated TANG molecules do result in similar contrast as experimentally observed (see Fig. 4.12), it is unclear how this reaction should proceed, given that dehydrogenation of hydrocarbons, a common remainder in UHV environments, has a large associated energetic barrier [96].

As previously mentioned, in STM studies of 2DCPs, bright round features in proximity of a network are often identified as residual halogens. However, the presented CO-terminated ncAFM images showed an absence of any features at the corresponding locations. Instead, bright protrusions are observed at seemingly unoccupied sites in STM. DFT simulations of the Br/Au$(1\,1\,1)$ system corroborate this result. It is well-known that Br adsorbs to hollow sites of the Au$(1\,1\,1)$ surface [97]. To verify the contrast formation, further DFT simulations of the Br/Au$(1\,1\,1)$ system were performed and the relaxed geometries fed into ppafm. A detailed force decomposition shows that a competition of short-range, and van der Waals forces is at play for the contrast formation in CO-terminated ncAFM. At close distances, short-range repulsive forces overwhelmingly contribute to the contrast close to the atomic center. This leads to the formation of a dim dark halo around a bright round protrusion (see Fig. 4.13). From chemical arguments, it should indeed be expected that Br stands out against the Au$(1\,1\,1)$ substrate due to it's electronegativity, leading to a local reduction in the density of states (DOS). The DFT calculations for the gas phase TANG dimer, as well as the BrAu$(1\,1\,1)$ system were performed by Manuel Eduardo Gonzalez Lastre (Universidad Autónoma de Madrid).

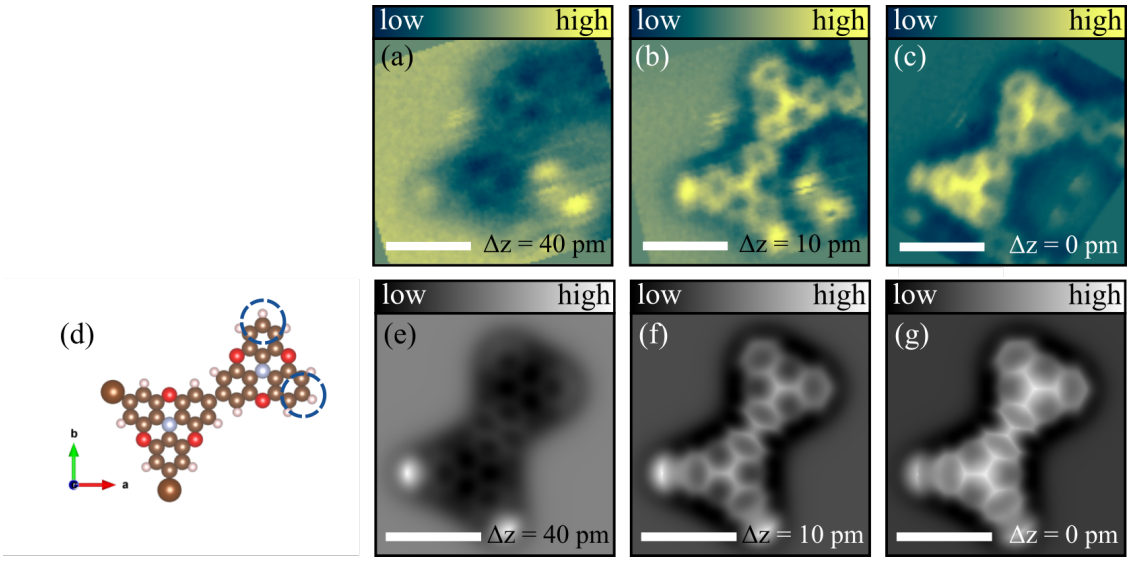

Figure 4.12: Quantitative agreement between FES to gas phase hydrogenated TANG molecules. (a-c) Stack of experimental Δf maps. (d) DFT-optimized geometry of gas phase hydrogenated TANG covalently coupled to brominated TANG molecule. (e-f) Stack of simulated Δf maps. Note that the contrast evolution for the brominated side agrees well with prior simulations of brominated TANG/Au(1 1 1). The specified height, Δz refers to the lowest approach distance in in each row for clarity. Imaging Parameters: $A = 55$ pm, $Q = 190,000$. Modeling parameters given in text. Scale bars: 1 nm.

4.2.3 Conclusion

In this chapter, high-resolution ncAFM images were presented, obtained using a tip terminated with a single CO molecule. The data were discussed and compared to DFT simulations. For the TES, two candidate terminations—Br and Au adatoms—were modeled using ppafm. The observed experimental contrast aligned more closely with simulations for Br-terminations, contrary to initial expectations. Indeed, as discussed, prevailing theories in the literature [15, 14, 39, 20] suggest that the dehalogenated, radical monomer species are stabilized by the metal surface until they undergo homocoupling with other monomers or oligomers. Stabilization via either surface atoms or adatoms induces a significant tilt in the molecule toward the sample surface, as corroborated by DFT simulations. Neither the TES nor FES exhibited a significant amount of puckering toward the sample, however.

A possible explanation for the observations is that the thermocouple employed to measure the sample temperature during deposition had not been calibrated properly, resulting in a higher readout temperature. This could have led to partial dehalogenation, allowing some monomers to form covalent bonds, while partially halogenated precursors were unable to participate in the reaction. Indeed, the quality of the grown network has been reported to be sensitive to the precise

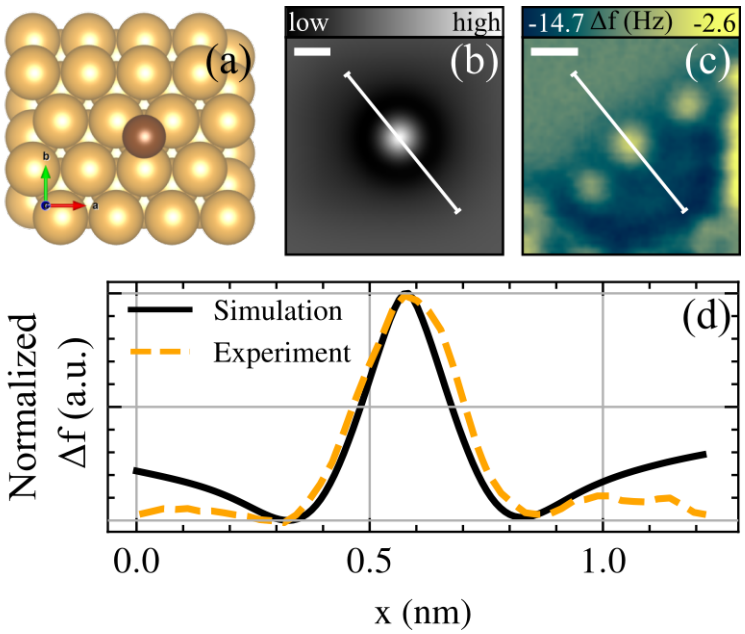

Figure 4.13: Comparison between simulated and experimental contrast of Br/Au(1 1 1) system. (a) DFT-optimized geometry on Au(1 1 1) slab. (b) Simulated contrast in ppafm shows dark halo around bright repulsive center. (c) Three residual bromines at edge of P^2(TANG) oligomer show similar contrast. (d) Extracted surface profiles (white lines) show mexican hat-like shape in both experimental, and simulated images. Scale bars: 250 pm.

sample temperature, with residual C−Br bonds observable by X-Ray Photoelectron Spectroscopy (XPS) up to 180°C, which represents the dehalogenation threshold for TBTANG molecules on Au(1 1 1) [17]. In this case, one might expect fully brominated monomer species to be trapped inside the porous network, adhered close to the edge of existing clusters, or isolated on the surface. While the latter is certainly unlikely due to a presumably low diffusion barrier of single molecules, neither of these scenarios was observed experimentally in this work. However, fully brominated molecules might adhere weakly to the surface, making them prone to desorption.

Given that many of the investigated edges remain halogenated, it is likely that these edges did not undergo dehalogenation, a process controlled by an Arrhenius activation equation:

$$r_{\text{dehal}} = \nu_{0,\text{dehal}} \exp\left(-\frac{E_{\text{dehal}}}{k_B T}\right). \tag{4.4}$$

This partial dehalogenation appears to be rate-limiting for the coupling step and might enhance the diffusion of partially dehalogenated monomers by weakening their interaction with the surface (see Fig. 4.14). As a result, coupling is suppressed, and diffusion dominates, allowing the system to relax into more ordered networks, as discussed in section 4.1. This mechanistic insight may contribute to the observed well-orderedness of P^2(TANG) networks on Au(1 1 1). Additionally,

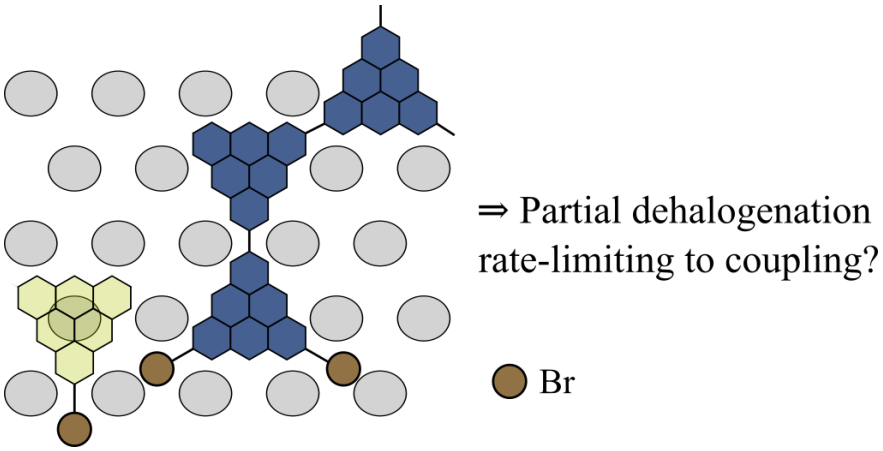

Figure 4.14: Interactions between partially dehalogenated P^2(TANG) cluster and partially dehalogenated single molecule might reduce the coupling rate and enhance network quality.

this mechanism might also aid in the reduction of topological defects, since mono-molecular ring closing reactions of 5-membered pores necessitate a prior dehalogenation of both participating monomers.

Furthermore, the incomplete dehalogenation of the edges might, in fact, provide an opportunity for transferring these 2D polymers from the growth substrate to insulating substrates. Indeed, as demonstrated by Galeotti et al. [17] and Dettmann et al. [42], the core polymer adheres relatively weakly to the metallic substrate. The transfer of these polymers to insulating substrates is primarily hindered by the high C−M bond energies at the grain boundaries. Tuning the termination of oligomers while maintaining network quality could open a promising avenue for sample transfer and future experiments.

To improve our understanding of the limiting factors in polymerization at the grain boundaries of active 2D polymers, we are currently modeling additional termination candidates for both the FES and TES states observed in the experimental data. For this purpose, we have recently started collaborating with the theory group of Ruben Perez (Universidad Autónoma de Madrid).

4.3 Lateral P^2(TANG-TANGO) Heterojunctions

Heterostructures of 2D materials extend their application in materials science. Particularly vertical heterostructures, i.e. out-of-plane stackings of 2D materials have been explored, however, lateral (in-plane) heterostructures have also gained significant interest, particularly in the field of 2D transition metal dichalcogenides (TMDs, MX_2, where M is a transition metal, and X a chalcogen) due to their relatively small lattice mismatch and controllable electronic structure via substitution of M, and X constituents [98], which allows for a seamless integration of two heterogeneous materi-

als. The synthesis of lateral 2D heterostructures is predicated on the principle of *edge epitaxy*, by which a 2D material is synthesized at the edge of a dissimilar 2D material.

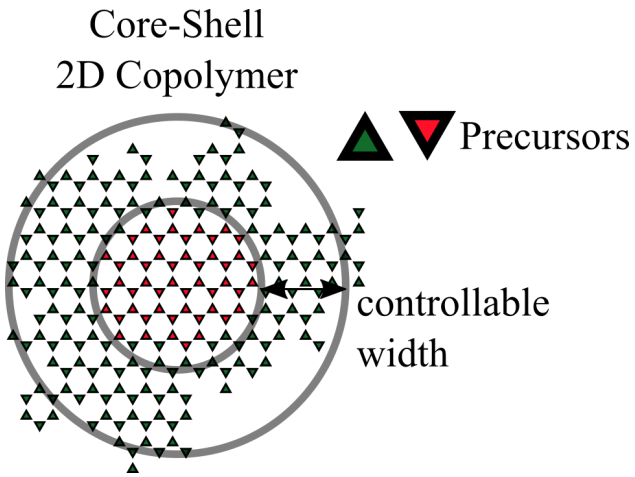

Figure 4.15: Idealized schematic of core-shell geometry of 2D block copolymer via sequential exposure of the surface to molecularly isostructural precursors.

In 1D polymer chemistry, the integration of two or more heterogeneous polymers is generally referred to as copolymerization. One differentiates between random, block, and alternating copolymers, based on the organisation of the fundamental building blocks in the backbone of the chain. The synthesis of 1D copolymers has significantly enhanced the applicability of polymers in technology, and efforts are made to extend copolymers into the second dimension. The synthesis of 1D alternating copolymer nanowires on Au(1 1 1) via Ullmann coupling has been attempted by Urgel et al. [99], however, the synthesis of extended structures with an alternating copolymer backbone was thwarted by the ability of both precursors to undergo homocoupling, making the controlled assembly of 1D alternating copolymers difficult. The on-surface synthesis of 2D block copolymer structures via Ullmann coupling can in principle be achieved by the sequential deposition of the two precursor materials. Depending on the exposure/dosage time, and sequence, of a metal surface by precursor gases, one might envision core-shell, or concentric ring copolymers, provided the reaction temperature for subsequent polymerization does not degrade pre-existing oligomers (see Fig. 4.15).

To synthesize 2D π-conjugated block copolymers (2DCBC), we used isostructural TBTANG, and TBTANGO precursors, which act as electron-donor, and electron-acceptor materials, respectively. Their properties are summarized in Table 4.1. Individually, the polymerization proceeds at similar temperatures on Au(1 1 1), at 210°C for P^2(TANG) [17], and at 265° C for P^2(TANGO) [44]. Due to their high thermal stability up to 400°C [17], the two polymers can be synthesized sequentially without risking their degradation. Moreover, their nearly identical lattice constants, owing to their structural similarity, makes them ideal candidates for the synthesis of 2DCBCs.

	P^2(TANG)/Au(1 1 1)	**P^2(TANGO)/Au**(1 1 1)
Monomer Chemical Structure	Brominated Carbonyl-bridged Triphenylamine	Brominated Oxygen-bridged Triphenylamine
Symmetry	Kagome	Kagome
Lattice Constant	1.75 nm	1.74 nm
Band Gap	1.8 eV*	3.14 eV
HOMO	0 eV*	−1.63 eV
LUMO	1.8 eV*	1.51 eV
Sublimation Temperature	120 ° C	180 ° C
Anneal Temperature	210 ° C	265 ° C

Table 4.1: Overview of Properties of Monopolymer P^2(TANG) and P^2(TANGO) on Au(1 1 1). Based on Galeotti et al. [17] for P^2(TANG), and Steiner et al. [44] for P^2(TANGO). Results from DFT calculations marked with (*).

We began by synthesizing P^2(TANG) oligomers on Au(1 1 1), targeting a coverage of ~ 0.4 ML. In the subsequent step, the surface was exposed to gaseous TBTANGO precursors with a targeted coverage of ~ 0.1 ML, while maintaining the sample at 210°C, although the synthesis of P^2(TANGO) typically requires a higher annealing temperature of 265°C, as reported by Steiner et al. [44]. Consequently, the initial exposure primarily resulted in small clusters of self-assembled, non-covalently bonded dimers and trimers adjacent to fully polymerized P^2(TANG) structures. Following a subsequent annealing step at the temperature required for P^2(TANGO) polymerization, the network quality improved. However, due to partial polymerization of TANGO, occurring during the initial step, the resulting copolymers exhibited a core-dendritic structure with a high defect density in the branches, instead of the targeted core-shell topology.

In any case, due to the close structural match of the precursors, differentiating between the two units in a block copolymer represents a challenge with STM alone. While structural differences can be discerned using CO-terminated ncAFM, we turned to using local density of states (LDOS) mapping, a scanning tunneling spectroscopy (STS) technique, where the density of states at a particular energy can be mapped out topographically by modulating the applied DC bias with an AC signal, and using a lock-in amplifier to filter out the corresponding component in the tunneling current (see section 3.1). Exemplary LDOS maps are shown in Fig. 4.16. Galeotti et al. [17] used angle resolved photoemission spectroscopy (ARPES) to investigate the valence band

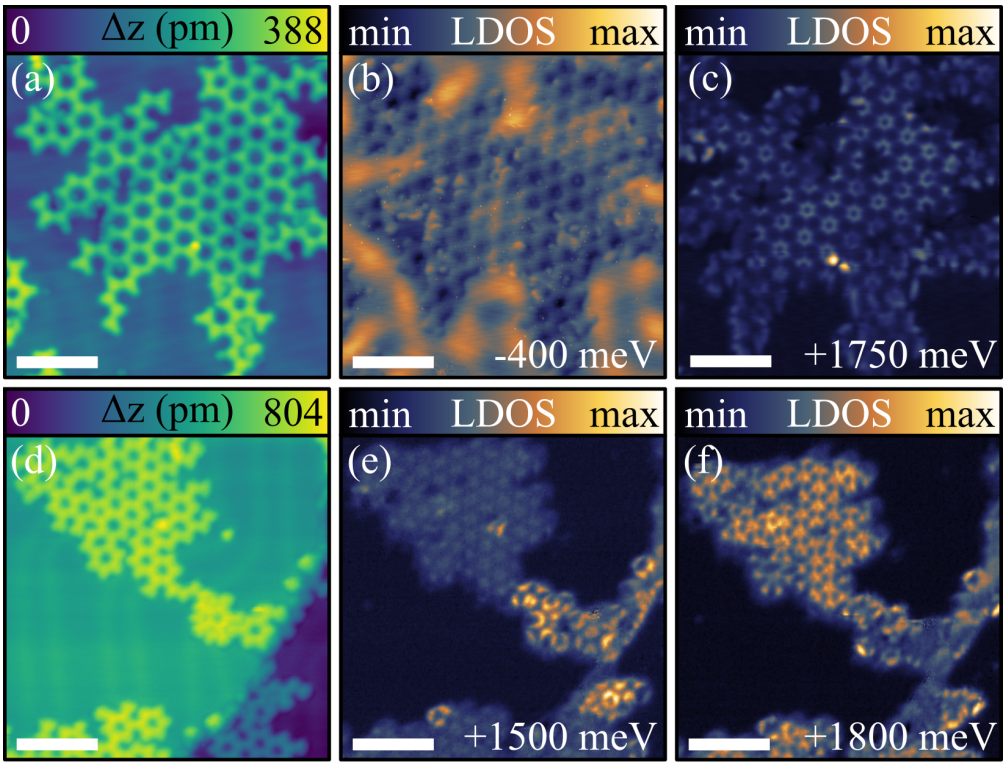

Figure 4.16: P^2(TANG-TANGO) Heterojunctions. (b) LDOS mapping at DOS feature corresponding to Dirac cone crossing below the HOMO level of P^2(TANG) does not show conclusive contrast due to the Au Shockley surface state screening. (c) LDOS map at intermediate energy to LUMO level of both P^2(TANG) and P^2(TANGO). (e, f) LDOS mapping of different copolymer islands at the conduction bands of the respective monopolymers shows visible distinguishable contrast. Imaging Parameters: (a), (c) $U = -500$ mV, $I_t = 50$ pA. (b, c), (e, f) $U_{AC} = 15$ mV, $f_{AC} = 709$ Hz, U (DC) inset in respective images. Scale bars: (a, c): 5 nm, (c, f): 7 nm.

of P^2(TANG)/Au(1 1 1) and experimentally confirmed the presence of a Dirac cone at $E = -400$ meV. Conversely, P^2(TANGO)/Au(1 1 1) is electronically silent at this energy, with valence band at -1.63 eV. An LDOS map of a well-ordered oligomer at this energy showed some contrast variation, but the features are convoluted with the Shockley surface state of the underlying Au substrate. Indeed, due to the presence of the Dirac cone in P^2(TANG)/Au(1 1 1), the DOS is expected to be small, while the presence of flat bands at the conduction band of both monopolymers leads to a large peak in the DOS.

We found that conduction band mapping presents an effective approach for differentiating between the two polymers. By focusing on distinct electronic signatures in the conduction band of both P^2(TANG)/Au(1 1 1) and P^2(TANGO)/Au(1 1 1), we were able to spatially resolve their distribution within the copolymer more clearly. With this approach, the identification of the two components with CO-terminated ncAFM might not be necessary. This will guide future experiments.

Chapter 5

Conclusion and Outlook

In this thesis, the reaction kinetics and edge chemistry, as well as electronic properties of two-dimensional organic nanostructures synthesized via Ullmann coupling has been investigated by integrating high-resolution imaging techniques, such as STM and CO-terminated ncAFM, with theoretical approaches including density functional theory (DFT) and kinetic Monte Carlo (kMC) simulations. This work provides a comprehensive framework for analyzing the growth and structural quality of 2D polymers. The findings address challenges in the field and offer fundamental, mechanistic insights and practical methodologies for advancing the design and synthesis of 2D materials, with reduced defect densities.

Findings

- **Reaction Kinetics and Network Quality:** A kMC model was developed to simulate the synthesis of 2D polymers by accounting for diffusion, rotation, and coupling events. By systematically varying the kinetic parameters, namely, the transitional energetic barriers, the model successfully replicated experimentally observed network structures formed on Au$(1\,1\,1)$. The model demonstrated that the balance between diffusion, rotation, and coupling rates significantly impacts network quality with coupling-limited process yielding more compact, defect-free structures, while diffusion-limited processes lead to highly branched structures.
- **Edge Chemistry of Growing 2D Polymers:** Experimental STM imaging revealed two distinct edge terminations: terminated edge states (TES), and feature-free edge states (FES). Atomic resolution CO-terminated imaging revealed two distinct subdivisions of the TES. DFT simulations suggested that most of the TES likely correspond to halogenated terminations, with one example that likely corresponds to a surface-stabilized radical, identified by

the strong molecular bending of the exposed phenyl group towards the surface. The FES likely correspond to weakly interacting radical, or hydrogenated terminations. The agreement between the experimental and simulated Δf maps supports these interpretations but also highlights unresvolved questions regarding the origin of the FES, should they indeed be hydrogenated.

- **Lateral Heterojunctions in 2D Polymers:** The synthesis of lateral heterojunctions between P^2(TANG) and P^2(TANGO) polymers demonstrated the realizability of forming 2D block copolymers with distinct electronic properties. Local density of states (LDOS) mapping was used to differentiate between the two polymers. This finding overcomes difficulties presented by the strucutral similarity in conventional STM imaging, and provides an efficient method for future explorations of 2D block copolymers.

Challenges and Limitations

- **Simplifications in kMC Modeling:** The discussed kMC model does not currently account for non-covalent interactions, topological defects, or mobile smaller oligomers (dimers, trimers, etc.). These simplifications may limit the model's accuracy. Additionally, the computational complexity of a system with vastly differing transition rates constrains the parameter space that can be explored and compared to experimental networks. Furthermore, the presented CO-terminated data hints at a suppressed coupling of partially dehalogenated monomers and polymers, which is not taken into account in the kMC model.
- **FES Termination Ambiguities:** The TES were well-characterized, but the exact chemical identity of FES remains unclear. Further experimental and computational validation is required to investigate the plausibility of hydrogenated terminations.
- **Experimental Constraints:** The frequency with which the edges of P^2(TANG) islands appear to remain halogenated during the reaction suggest an incomplete dehalogenation due to an insufficient sample temperature during the anneal process. This complicates the interpretation of the edge chemistry determination.

Broader Implications

This thesis highlights the interplay between kinetic parameters and network quality, providing valuable insights into the synthesis of 2D polymers with tailored properties. The methodologies developed here can be applied to other on-surface polymerization systems, enabling:

- **Defect Control**: Understanding how reaction kinetics influence defect formation can guide the design of precursors and substrates to minimize defects.
- **Material Transfer**: Insights into edge terminations suggest potential strategies for transferring 2D polymers from metallic to insulating substrates while preserving network integrity.
- **Electronic Applications**: The successful synthesis and characterization of lateral heterojunctions open avenues for designing 2D materials with tunable electronic properties for applications in optoelectronics and catalysis.

Future Directions

- **Improved kMC Model:** To make vastly different transition rates accessible for computation, a problem known as *timescale disparity*, more sophisticated time-propagation algorithms have to be implemented. Additionally, a physically more meaningful model would have to take non-covalent interactions into account and allow for the formation of topological defects.
- **Expanded DFT Simulations:** Additional simulations need to be performed to explore alternative edge terminations, such as surface-stabilized radicals, or adatom-coordinates species with different epitaxial relationships to the substrate. Simulations of polymeric islands with extended π-conjugation should provide a deeper understanding of polymer + substrate interactions. While this might be computationally difficult for P^2(TANG)/Au$(1\,1\,1)$, smaller systems like tribromobenzene/Au$(1\,1\,1)$ might provide insights by analogy. To interpret the results presented in this thesis, it is additionally crucial to compute the energetic barriers and kinetic transitions involved in the polymerization, particularly for partially debrominated species.
- **Other Experimental Techniques:** Complementary methods, such as X-ray photoelectron spectroscopy (XPS), or infrafred spectroscopy, could provide independent verification of edge terminations and network composition and aid the interpretation of the experimental data. Additionally, fast-XPS studies could help justify assumptions in kMC simulations.

Appendix A

Au$(1\,1\,1)$ Kink Sites as Nucleation Sites for 2DCPs and Observation of new Surface Reconstruction

To investigate the effect of nucleation sites on the quality of the subsequent film, TANG polymer was synthesized on Au$(1\,1\,1)$ at intermediate coverages from $0.1-1$ ML.

An object classification workflow was utilized to categorize polymer islands in experimental STM image using ilastik [100]. Using this workflow, insight into the nucleation can be obtained using statistical methods. For this purpose, around 1,000 individual island positions, readily accessible with this workflow as the centers of mass of each classified island, are extracted. The nearest neighbor of each island is identified, and the distance, as well as angle of the connecting line between two nearest neighbors shown in the histograms in Fig. A.1. From this data, the nucleation of the polymer is seen to be anisotropic. Indeed, the mean distance of nearest neighbor islands, $d_{\text{mean}} = 17.0 \pm 3$ nm, correlates well with the half period length of the herringbone reconstruction of the Au$(1\,1\,1)$ surface, given typically around ~ 32 nm [101]. It is therefore a natural conclusion that the polymers nucleate at the kink sites of the reconstruction. Similar conclusions have been made in the synthesis of other thin films on Au$(1\,1\,1)$, for example by Voigtländer et al. [102], who studied the growth of cobalt thin films. The kink sites are typically observed with a higher surface corrugation ($\Delta z \sim 60-90$ pm) in STM, and are the consequence of a dislocated atom due to the competition between face-centered cubic, and hexagonal close-packing lattice structures at the surface [101, 102]. For this reason, it can be expected that the kink sites are catalytically more active, potentially readily supplying a surface adatom to participate in the polymerization reaction [87]. Furthermore, the presence of the organic monolayer is seen to strongly modify the herringbone reconstruction overall, which has been observed for other conjugated molecules, self-assembled

on Au(1 1 1), like C_{60} [103], or $\alpha-$sexithiophene [104]. This observation is typically interpreted in light of a local relief in surface strain due to the Molecule-Substrate interaction energy.

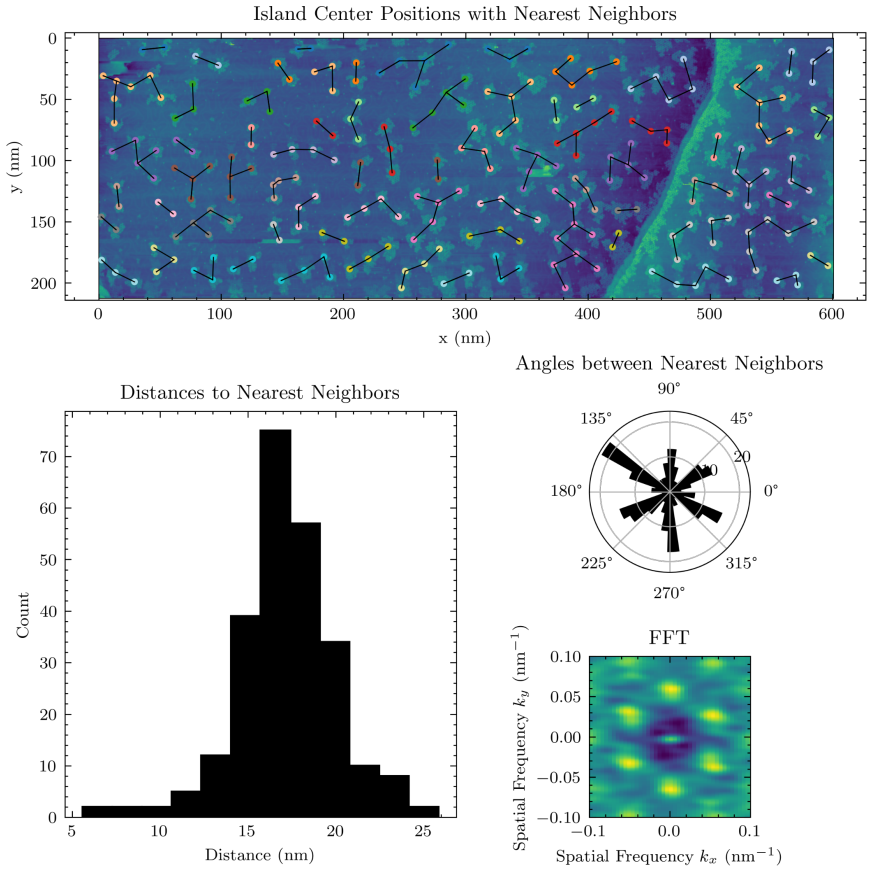

Figure A.1: Object classification analysis of ~ 0.4 ML P^2(TANG) islands on Au(1 1 1) using ilastik. The island center of mass positions are extracted, and nearest neighbors calculated. (Top): Large Scale STM Δz map showcasing the classification using the described workflow. Nearest neighbors positions are indicated through like colors, and connecting lines between. (Bottom, left): Histogram of the computed nearest neighbor distances. The mean value, $d \sim 17 \pm 3$ nm correlates well with the periodicity of kink sites of the Au(1 1 1) herringbone reconstruction. (Bottom, right): Polar histogram of the angles between nearest neighbors, and 2D FFT of the center of mass positions of the islands.

The on-surface Ullmann coupling reaction between monomer species forms an irreversible covalent bond, and due to the lattice mismatch between the P^2(TANG) monolayer and the Au(1 1 1) surface, coalescing domains during the growth can be expected to form grain boundaries. Indeed, in the crystal growth community, it is commonly known that an inverse relationship between nucleation site density and the average grain size exists. To reduce the formation of topological defects, Galeotti et al.[17] implemented the use of rigid precursors with high strain energy penalties. With this approach, they succeeded in extending the achievable domain size of P^2(TANG) to 100 nm in diameter and more. At this length scale, the influence of coalescing domains could be the lim-

iting factor in the synthesis of larger well-ordered domains. To preserve the catalytic activity of the Au$(1\,1\,1)$ surface, while freely modifying the nucleation site density, electrochemical methods could be applied to lift the surface reconstruction reached through thermal annealing in ultra-high vacuum [105].

Appendix B

The Wasserstein Metric of Two Discrete Distributions

The first-order Wasserstein metric of two discrete probability distributions, P, and Q is defined as [85]

$$W_1(P,Q) = \min_{\pi \in \Pi(P,Q)} \sum_{i=1}^{n} \sum_{j=1}^{n} \pi_{ij} \cdot d(x_i, x_j). \tag{B.1}$$

- π_{ij} represents the amount of mass transported from x_i (in P) to x_j (in Q).
- The set $\Pi(P,Q)$ contains all valid transportation plans satisfying:

$$\sum_{j=1}^{n} \pi_{ij} = p_i, \quad \sum_{i=1}^{n} \pi_{ij} = q_j, \quad \pi_{ij} \geq 0$$

- $d(x_i, x_j)$ denotes the euclidian distance between the two discrete points x_i, and x_j.

The Wasserstein metric finds the transportation plan π that minimizes the total cost. This is done computationally using the `wasserstein_distance()` method, implemented in `scipy.stats` [86].

Bibliography

[1] K. S. Novoselov, A. K. Geim, S. V. Morozov, D. Jiang, Y. Zhang, S. V. Dubonos, I. V. Grigorieva, and A. A. Firsov. Electric field effect in atomically thin carbon films. *Science*, 306(5696):666–669, 2004. doi: 10.1126/science.1102896. URL https://www.science.org/doi/abs/10.1126/science.1102896.

[2] N David Mermin. Crystalline order in two dimensions. *Physical review*, 176(1):250, 1968.

[3] Lev Davidovich Landau. Zur theorie der phasenumwandlungen ii. *Phys. Z. Sowjetunion*, 11 (545):26–35, 1937.

[4] Jannik C. Meyer, A. K. Geim, M. I. Katsnelson, K. S. Novoselov, T. J. Booth, and S. Roth. The structure of suspended graphene sheets. *Nature*, 446(7131):60–63, March 2007. ISSN 1476-4687. doi: 10.1038/nature05545. URL https://www.nature.com/articles/nature05545. Publisher: Nature Publishing Group.

[5] Gianluca Galeotti. *On-surface formation of graphene-like materials through Ullmann coupling*. Phd thesis, Université du Québec Institut National de la Recherche Scientifique, 2019. Available at https://espace.inrs.ca/id/eprint/9016/1/Galeotti%2C%20Gianluca.pdf.

[6] K. S. Novoselov, V. I. Falko, L. Colombo, P. R. Gellert, M. G. Schwab, and K. Kim. A roadmap for graphene. *Nature*, 490(7419):192–200, October 2012. ISSN 1476-4687. doi: 10.1038/nature11458. URL https://www.nature.com/articles/nature11458. Number: 7419 Publisher: Nature Publishing Group.

[7] L. Britnell, R. V. Gorbachev, R. Jalil, B. D. Belle, F. Schedin, A. Mishchenko, T. Georgiou, M. I. Katsnelson, L. Eaves, S. V. Morozov, N. M. R. Peres, J. Leist, A. K. Geim, K. S. Novoselov, and L. A. Ponomarenko. Field-effect tunneling transistor based on vertical graphene heterostructures. *Science*, 335(6071):947–950, 2012. doi: 10.1126/science.1218461. URL https://www.science.org/doi/abs/10.1126/science.1218461.

[8] C. R. Dean, A. F. Young, I. Meric, C. Lee, L. Wang, S. Sorgenfrei, K. Watanabe, T. Taniguchi, P. Kim, K. L. Shepard, and J. Hone. Boron nitride substrates for high-quality graphene electronics. *Nature Nanotechnology*, 5(10):722–726, October 2010. ISSN 1748-3395. doi: 10.1038/nnano.2010.172. URL https://www.nature.com/articles/nnano.2010.172. Publisher: Nature Publishing Group.

[9] Alexander S. Mayorov, Roman V. Gorbachev, Sergey V. Morozov, Liam Britnell, Rashid Jalil, Leonid A. Ponomarenko, Peter Blake, Kostya S. Novoselov, Kenji Watanabe, Takashi Taniguchi, and A. K. Geim. Micrometer-Scale Ballistic Transport in Encapsulated Graphene at Room Temperature. *Nano Letters*, 11(6):2396–2399, June 2011. ISSN 1530-6984. doi: 10.1021/nl200758b. URL https://doi.org/10.1021/nl200758b. Publisher: American Chemical Society.

[10] Leonid Levitov and Gregory Falkovich. Electron viscosity, current vortices and negative nonlocal resistance in graphene. *Nature Physics*, 12(7):672–676, July 2016. ISSN 1745-2481. doi: 10.1038/nphys3667. URL https://www.nature.com/articles/nphys3667. Number: 7 Publisher: Nature Publishing Group.

[11] Toyosei Kawasaki, Takashi Ichimura, Hiroshi Kishimoto, Ade Asneil Akbar, Takashi Ogawa, and Chuhei Oshima. Double Atomic Layers of Graphene/Monolayer h-BN on Ni(111) Studied by Scanning Tunneling Microscopy and Scanning Tunneling Spectroscopy. *Surface Review and Letters*, 9(3-04):1459–1464, January 2002. doi: 10.1142/S0218625X02003883.

[12] Deep Jariwala, Anchal Srivastava, and Pulickel M. Ajayan. Graphene synthesis and band gap opening. *Journal of Nanoscience and Nanotechnology*, 11(8):6621–6641, 2011. ISSN 1533-4880. doi: doi:10.1166/jnn.2011.5001. URL https://www.ingentaconnect.com/content/asp/jnn/2011/00000011/00000008/art00001.

[13] Dmitrii F. Perepichka and Federico Rosei. Extending polymer conjugation into the second dimension. *Science*, 323(5911):216–217, 2009. doi: 10.1126/science.1165429. URL https://www.science.org/doi/abs/10.1126/science.1165429.

[14] M. Lackinger. Surface-assisted ullmann coupling. *Chem. Commun.*, 53:7872–7885, 2017. doi: 10.1039/C7CC03402D. URL http://dx.doi.org/10.1039/C7CC03402D.

[15] Marco Bieri, Manh-Thuong Nguyen, Oliver Gröning, Jinming Cai, Matthias Treier, Kamel Aït-Mansour, Pascal Ruffieux, Carlo A. Pignedoli, Daniele Passerone, Marcel Kastler, Klaus Müllen, and Roman Fasel. Two-Dimensional Polymer Formation on Surfaces: Insight into

the Roles of Precursor Mobility and Reactivity. *Journal of the American Chemical Society*, 132(46):16669–16676, November 2010. ISSN 0002-7863. doi: 10.1021/ja107947z. URL https://doi.org/10.1021/ja107947z. Publisher: American Chemical Society.

[16] Marco Bieri, Matthias Treier, Jinming Cai, Kamel Aït-Mansour, Pascal Ruffieux, Oliver Gröning, Pierangelo Gröning, Marcel Kastler, Ralph Rieger, Xinliang Feng, Klaus Müllen, and Roman Fasel. Porous graphenes: two-dimensional polymer synthesis with atomic precision. *Chemical Communications*, 45:6919, 2009. ISSN 1359-7345, 1364-548X. doi: 10.1039/b915190g. URL http://xlink.rsc.org/?DOI=b915190g.

[17] G. Galeotti, F. De Marchi, E. Hamzehpoor, O. MacLean, M. Rajeswara Rao, Y. Chen, L. V. Besteiro, D. Dettmann, L. Ferrari, F. Frezza, P. M. Sheverdyaeva, R. Liu, A. K. Kundu, P. Moras, M. Ebrahimi, M. C. Gallagher, F. Rosei, D. F. Perepichka, and G. Contini. Synthesis of mesoscale ordered two-dimensional pi-conjugated polymers with semiconducting properties. *Nature Materials*, 19(8):874–880, August 2020. ISSN 1476-4660. doi: 10.1038/s41563-020-0682-z. URL https://www.nature.com/articles/s41563-020-0682-z. Number: 8 Publisher: Nature Publishing Group.

[18] Robert Lindner and Angelika Kühnle. On-surface reactions. *ChemPhysChem*, 16(8):1582–1592, 2015. doi: https://doi.org/10.1002/cphc.201500161. URL https://chemistry-europe.onlinelibrary.wiley.com/doi/abs/10.1002/cphc.201500161.

[19] Leonhard Grill and Stefan Hecht. Covalent on-surface polymerization. *Nature Chemistry*, 12(2):115–130, February 2020. ISSN 1755-4349. doi: 10.1038/s41557-019-0392-9. URL https://www.nature.com/articles/s41557-019-0392-9. Number: 2 Publisher: Nature Publishing Group.

[20] Grégory Franc and André Gourdon. Covalent networks through on-surface chemistry in ultra-high vacuum: state-of-the-art and recent developments. *Physical Chemistry Chemical Physics*, 13(32):14283–14292, August 2011. ISSN 1463-9084. doi: 10.1039/C1CP20700H. URL https://pubs.rsc.org/en/content/articlelanding/2011/cp/c1cp20700h. Publisher: The Royal Society of Chemistry.

[21] Junji Sakamoto, Jeroen van Heijst, Oleg Lukin, and A. Dieter Schlüter. Two-Dimensional Polymers: Just a Dream of Synthetic Chemists? *Angewandte Chemie International Edition*, 48(6):1030–1069, 2009. ISSN 1521-3773. doi: 10.1002/anie.200801863. URL https://onlinelibrary.wiley.com/doi/abs/10.1002/anie.200801863. _eprint: https://onlinelibrary.wiley.com/doi/pdf/10.1002/anie.200801863.

[22] Christophe Nacci, Stefan Hecht, and Leonhard Grill. The emergence of covalent on-surface polymerization. In André Gourdon, editor, *On-surface synthesis*, pages 1–21, Cham, 2016. Springer International Publishing. ISBN 978-3-319-26600-8.

[23] John W. Colson and William R. Dichtel. Rationally synthesized two-dimensional polymers. *Nature Chemistry*, 5(6):453–465, June 2013. ISSN 1755-4349. doi: 10.1038/nchem.1628. URL https://www.nature.com/articles/nchem.1628. Publisher: Nature Publishing Group.

[24] Kurt Kolasinski. *Chemisorption, Physisorption and Dynamics*, chapter 3, pages 115–183. John Wiley & Sons, Ltd, 2012. ISBN 9781119941798. doi: https://doi.org/10.1002/9781119941798.ch3. URL https://onlinelibrary.wiley.com/doi/abs/10.1002/9781119941798.ch3.

[25] Richard L. Schwoebel and Edward J. Shipsey. Step Motion on Crystal Surfaces. *Journal of Applied Physics*, 37(10):3682–3686, September 1966. doi: 10.1063/1.1707904.

[26] Marco Di Giovannantonio, Massimo Tomellini, Josh Lipton-Duffin, Gianluca Galeotti, Maryam Ebrahimi, Albano Cossaro, Alberto Verdini, Neerav Kharche, Vincent Meunier, Guillaume Vasseur, Yannick Fagot-Revurat, Dmitrii F. Perepichka, Federico Rosei, and Giorgio Contini. Mechanistic Picture and Kinetic Analysis of Surface-Confined Ullmann Polymerization. *Journal of the American Chemical Society*, 138(51):16696–16702, December 2016. ISSN 0002-7863. doi: 10.1021/jacs.6b09728. URL https://doi.org/10.1021/jacs.6b09728. Publisher: American Chemical Society.

[27] Stefan Schlögl, Wolfgang M. Heckl, and Markus Lackinger. On-surface radical addition of triply iodinated monomers on Au(111)—the influence of monomer size and thermal post-processing. *Surface Science*, 606(13):999–1004, 2012. ISSN 0039-6028. doi: https://doi.org/10.1016/j.susc.2012.02.011. URL https://www.sciencedirect.com/science/article/pii/S0039602812000623.

[28] Rico Gutzler, Hermann Walch, Georg Eder, Stephan Kloft, Wolfgang M. Heckl, and Markus Lackinger. Surface mediated synthesis of 2D covalent organic frameworks: 1,3,5-tris(4-bromophenyl)benzene on graphite(001), Cu(111), and Ag(110). *Chemical Communications*, 29:4456–4458, 2009. doi: 10.1039/B906836H. URL http://dx.doi.org/10.1039/B906836H. Publisher: The Royal Society of Chemistry.

[29] Gianluca Galeotti, Marco Di Giovannantonio, Josh Lipton-Duffin, Maryam Ebrahimi, Stefano Tebi, Alberto Verdini, Luca Floreano, Yannick Fagot-Revurat, Dmitrii F. Perepichka,

Federico Rosei, and Giorgio Contini. The role of halogens in on-surface Ullmann polymerization. *Faraday Discussions*, 204(0):453–469, October 2017. ISSN 1364-5498. doi: 10.1039/C7FD00099E. URL https://pubs.rsc.org/en/content/articlelanding/2017/fd/c7fd00099e. Publisher: The Royal Society of Chemistry.

[30] F. Ullmann and Jean Bielecki. Ueber synthesen in der biphenylreihe. *Berichte der deutschen chemischen Gesellschaft*, 34(2):2174–2185, 1901. doi: https://doi.org/10.1002/cber.190103402141. URL https://chemistry-europe.onlinelibrary.wiley.com/doi/abs/10.1002/cber.190103402141.

[31] Ming Xi and Brian E. Bent. Iodobenzene on cu(111): Formation and coupling of adsorbed phenyl groups. *Surface Science*, 278(1):19–32, 1992. ISSN 0039-6028. doi: https://doi.org/10.1016/0039-6028(92)90580-Y. URL https://www.sciencedirect.com/science/article/pii/003960289290580Y.

[32] Ming Xi and Brian E. Bent. Mechanisms of the ullmann coupling reaction in adsorbed monolayers. *Journal of the American Chemical Society*, 115(16):7426–7433, 1993. doi: 10.1021/ja00069a048. URL https://doi.org/10.1021/ja00069a048.

[33] Saw-Wai Hla, Ludwig Bartels, Gerhard Meyer, and Karl-Heinz Rieder. Inducing All Steps of a Chemical Reaction with the Scanning Tunneling Microscope Tip: Towards Single Molecule Engineering. *Physical Review Letters*, 85(13):2777–2780, September 2000. ISSN 0031-9007, 1079-7114. doi: 10.1103/PhysRevLett.85.2777. URL https://link.aps.org/doi/10.1103/PhysRevLett.85.2777.

[34] D. Sloan, Y.-M. Sun, H. Ihm, and J. M. White. Photochemistry of Iodobenzene Adsorbed on Sapphire(0001). *The Journal of Physical Chemistry B*, 102(35):6825–6830, August 1998. ISSN 1520-6106. doi: 10.1021/jp981537q. URL https://doi.org/10.1021/jp981537q. Publisher: American Chemical Society.

[35] Carlos-Andres Palma, Katharina Diller, Reinhard Berger, Alexander Welle, Jonas Björk, Jose Luis Cabellos, Duncan J. Mowbray, Anthoula C. Papageorgiou, Natalia P. Ivleva, Sonja Matich, Emanuela Margapoti, Reinhard Niessner, Bernhard Menges, Joachim Reichert, Xinliang Feng, Hans Joachim Räder, Florian Klappenberger, Angel Rubio, Klaus Müllen, and Johannes V. Barth. Photoinduced C–C Reactions on Insulators toward Photolithography of Graphene Nanoarchitectures. *Journal of the American Chemical Society*, 136(12):4651–4658, March 2014. ISSN 0002-7863. doi: 10.1021/ja412868w. URL https://doi.org/10.1021/ja412868w. Publisher: American Chemical Society.

[36] Lukas Grossmann, Benjamin T. King, Stefan Reichlmaier, Nicolai Hartmann, Johanna Rosen, Wolfgang M. Heckl, Jonas Björk, and Markus Lackinger. On-surface photopolymerization of two-dimensional polymers ordered on the mesoscale. *Nature Chemistry*, 13 (8):730–736, August 2021. ISSN 1755-4349. doi: 10.1038/s41557-021-00709-y. URL https://www.nature.com/articles/s41557-021-00709-y. Number: 8 Publisher: Nature Publishing Group.

[37] L. Dong, S. Wang, W. Wang, C. Chen, T. Lin, J. Adisoejoso, and N. Lin. Transition metals trigger on-surface ullmann coupling reaction: Intermediate, catalyst and template. In André Gourdon, editor, *On-surface synthesis*, pages 23–42, Cham, 2016. Springer International Publishing. ISBN 978-3-319-26600-8.

[38] Cui-Zhong Guan, Dong Wang, and Li-Jun Wan. Construction and repair of highly ordered 2D covalent networks by chemical equilibrium regulation. *Chemical Communications*, 48 (24):2943–2945, February 2012. ISSN 1364-548X. doi: 10.1039/C2CC16892H. URL https://pubs.rsc.org/en/content/articlelanding/2012/cc/c2cc16892h. Publisher: The Royal Society of Chemistry.

[39] Jonas Björk, Felix Hanke, and Sven Stafström. Mechanisms of Halogen-Based Covalent Self-Assembly on Metal Surfaces. *Journal of the American Chemical Society*, 135(15): 5768–5775, April 2013. ISSN 0002-7863, 1520-5126. doi: 10.1021/ja400304b. URL https://pubs.acs.org/doi/10.1021/ja400304b.

[40] Jonas Björk, Sven Stafström, and Felix Hanke. Zipping Up: Cooperativity Drives the Synthesis of Graphene Nanoribbons. *Journal of the American Chemical Society*, 133 (38):14884–14887, September 2011. ISSN 0002-7863. doi: 10.1021/ja205857a. URL https://doi.org/10.1021/ja205857a. Publisher: American Chemical Society.

[41] Lang Jiang, Tianchao Niu, Xiuqiang Lu, Huanli Dong, Wei Chen, Yunqi Liu, Wenping Hu, and Daoben Zhu. Low-temperature, bottom-up synthesis of graphene via a radical-coupling reaction. *Journal of the American Chemical Society*, 135(24):9050–9054, 2013. doi: 10.1021/ja4031825. URL https://doi.org/10.1021/ja4031825. PMID: 23701398.

[42] Dominik Dettmann, Polina M. Sheverdyaeva, Ehsan Hamzehpoor, Stefano Franchi, Gianluca Galeotti, Paolo Moras, Chiara Ceccarelli, Dmytro F. Perepichka, Federico Rosei, and Giorgio Contini. Electronic Band Engineering of Two-Dimensional Kagomé Polymers. *ACS Nano*, December 2023. ISSN 1936-0851. doi: 10.1021/acsnano.3c09476. URL https://doi.org/10.1021/acsnano.3c09476. Publisher: American Chemical Society.

[43] L. Lafferentz, V. Eberhardt, C. Dri, C. Africh, G. Comelli, F. Esch, S. Hecht, and L. Grill. Controlling on-surface polymerization by hierarchical and substrate-directed growth. *Nature Chemistry*, 4(3):215–220, January 2012. ISSN 1755-4349. doi: 10.1038/nchem.1242.

[44] Christian Steiner, Julian Gebhardt, Maximilian Ammon, Zechao Yang, Alexander Heidenreich, Natalie Hammer, Andreas Görling, Milan Kivala, and Sabine Maier. Hierarchical on-surface synthesis and electronic structure of carbonyl-functionalized one- and two-dimensional covalent nanoarchitectures. *Nature Communications*, 8(1):14765, March 2017. ISSN 2041-1723. doi: 10.1038/ncomms14765. URL https://www.nature.com/articles/ncomms14765. Number: 1 Publisher: Nature Publishing Group.

[45] Leonhard Grill, Matthew Dyer, Leif Lafferentz, Mats Persson, Maike V. Peters, and Stefan Hecht. Nano-architectures by covalent assembly of molecular building blocks. *Nature Nanotechnology*, 2(11):687–691, October 2007. ISSN 1748-3395. doi: 10.1038/nnano.2007.346. URL http://dx.doi.org/10.1038/nnano.2007.346.

[46] Rico Gutzler and Dmitrii F. Perepichka. pi-Electron conjugation in two dimensions. *Journal of the American Chemical Society*, 135(44):16585–16594, November 2013. ISSN 1520-5126. doi: 10.1021/ja408355p.

[47] Simil Thomas, Hong Li, Cheng Zhong, Michio Matsumoto, William R. Dichtel, and Jean-Luc Bredas. Electronic Structure of Two-Dimensional pi-Conjugated Covalent Organic Frameworks. *Chemistry of Materials*, 31(9):3051–3065, May 2019. ISSN 0897-4756. doi: 10.1021/acs.chemmater.8b04986. URL https://doi.org/10.1021/acs.chemmater.8b04986. Publisher: American Chemical Society.

[48] Andres Castellanos-Gomez, Michele Buscema, Rianda Molenaar, Vibhor Singh, Laurens Janssen, Herre S. J. van der Zant, and Gary A. Steele. Deterministic transfer of two-dimensional materials by all-dry viscoelastic stamping. *2D Materials*, 1(1):011002, April 2014. ISSN 2053-1583. doi: 10.1088/2053-1583/1/1/011002. URL https://dx.doi.org/10.1088/2053-1583/1/1/011002. Publisher: IOP Publishing.

[49] Maria B Wieland, Anna G Slater, Barry Mangham, Neil R Champness, and Peter H Beton. Fullerenes as adhesive layers for mechanical peeling of metallic, molecular and polymer thin films. *Beilstein journal of nanotechnology*, 5:394—401, 2014. ISSN 2190-4286. doi: 10.3762/bjnano.5.46. URL https://europepmc.org/articles/PMC3999765.

[50] Christophe Nacci, Alexander Saywell, Cedric Troadec, Jie Deng, Marc Georg Willinger, Christian Joachim, and Leonhard Grill. Toward printing molecular nanostructures from

microstructured samples in ultrahigh vacuum. *Journal of Vacuum Science and Technology B*, 34(1):011801, 2015. ISSN 2166-2746. doi: 10.1116/1.4936886. URL https://nottingham-repository.worktribe.com/output/770151.

[51] Atena Rastgoo-Lahrood, Matthias Lischka, Johanna Eichhorn, Debabrata Samanta, Michael Schmittel, Wolfgang M. Heckl, and Markus Lackinger. Reversible intercalation of iodine monolayers between on-surface synthesised covalent polyphenylene networks and Au(111). *Nanoscale*, 9(15):4995–5001, April 2017. ISSN 2040-3372. doi: 10.1039/C7NR00705A. URL https://pubs.rsc.org/en/content/articlelanding/2017/nr/c7nr00705a. Publisher: The Royal Society of Chemistry.

[52] Fabio Cicoira, Jill A. Miwa, Dmitrii F. Perepichka, and Federico Rosei. Molecular Assembly of Rubrene on a Metal/Metal Oxide Nanotemplate. *The Journal of Physical Chemistry A*, 111(49):12674–12678, December 2007. ISSN 1089-5639. doi: 10.1021/jp076090c. URL https://doi.org/10.1021/jp076090c. Publisher: American Chemical Society.

[53] Markus Kittelmann, Philipp Rahe, Markus Nimmrich, Christopher M. Hauke, André Gourdon, and Angelika Kühnle. On-Surface Covalent Linking of Organic Building Blocks on a Bulk Insulator. *ACS Nano*, 5(10):8420–8425, October 2011. ISSN 1936-0851. doi: 10.1021/nn2033192. URL https://doi.org/10.1021/nn2033192. Publisher: American Chemical Society.

[54] Jinne Adisoejoso, Tao Lin, Xue Song Shang, Ke Ji Shi, Aditi Gupta, Pei Nian Liu, and Nian Lin. A single-molecule-level mechanistic study of pd-catalyzed and cu-catalyzed homocoupling of aryl bromide on an au(111) surface. *Chemistry – A European Journal*, 20(14):4111–4116, 2014. doi: https://doi.org/10.1002/chem.201304443. URL https://chemistry-europe.onlinelibrary.wiley.com/doi/abs/10.1002/chem.201304443.

[55] Wei Zhao, Lei Dong, Chao Huang, Zaw Myo Win, and Nian Lin. Cu- and Pd-catalyzed Ullmann reaction on a hexagonal boron nitride layer. *Chemical Communications*, 52(90):13225–13228, November 2016. ISSN 1364-548X. doi: 10.1039/C6CC05029H. URL https://pubs.rsc.org/en/content/articlelanding/2016/cc/c6cc05029h. Publisher: The Royal Society of Chemistry.

[56] Chengliang Wang, Huanli Dong, Wenping Hu, Yunqi Liu, and Daoben Zhu. Semiconducting pi-Conjugated Systems in Field-Effect Transistors: A Material Odyssey of Organic Electronics. *Chemical Reviews*, 112(4):2208–2267, April 2012. ISSN 0009-2665. doi:

10.1021/cr100380z. URL https://doi.org/10.1021/cr100380z. Publisher: American Chemical Society.

[57] Aaron D. Franklin. Nanomaterials in transistors: From high-performance to thin-film applications. *Science*, 349(6249):aab2750, 2015. doi: 10.1126/science.aab2750. URL https://www.science.org/doi/abs/10.1126/science.aab2750.

[58] Frank Schwierz. Graphene transistors. *Nature Nanotechnology*, 5(7):487–496, July 2010. ISSN 1748-3395. doi: 10.1038/nnano.2010.89.

[59] Yasuhiko Shirota and Hiroshi Kageyama. Charge Carrier Transporting Molecular Materials and Their Applications in Devices. *Chemical Reviews*, 107(4):953–1010, April 2007. ISSN 0009-2665. doi: 10.1021/cr050143+. URL https://doi.org/10.1021/cr050143+. Publisher: American Chemical Society.

[60] José I. Urgel, David Écija, Guoqing Lyu, Ran Zhang, Carlos-Andres Palma, Willi Auwärter, Nian Lin, and Johannes V. Barth. Quasicrystallinity expressed in two-dimensional coordination networks. *Nature Chemistry*, 8(7):657–662, July 2016. ISSN 1755-4349. doi: 10.1038/nchem.2507. URL https://www.nature.com/articles/nchem.2507. Publisher: Nature Publishing Group.

[61] Fabian Mohn. *Probing electronic and structural properties of single molecules on the atomic scale*. Phd thesis, Universität Regensburg, 2012. Available at https://epub.uni-regensburg.de/25245/.

[62] Jascha Repp, Gerhard Meyer, Sladjana M. Stojković, André Gourdon, and Christian Joachim. Molecules on insulating films: Scanning-tunneling microscopy imaging of individual molecular orbitals. *Phys. Rev. Lett.*, 94:026803, Jan 2005. doi: 10.1103/PhysRevLett.94.026803. URL https://link.aps.org/doi/10.1103/PhysRevLett.94.026803.

[63] Leo Gross, Fabian Mohn, Nikolaj Moll, Peter Liljeroth, and Gerhard Meyer. The Chemical Structure of a Molecule Resolved by Atomic Force Microscopy. *Science*, 325(5944):1110–1114, August 2009. doi: 10.1126/science.1176210. URL https://www.science.org/doi/10.1126/science.1176210. Publisher: American Association for the Advancement of Science.

[64] Franz J. Giessibl. Forces and frequency shifts in atomic-resolution dynamic-force microscopy. *Phys. Rev. B*, 56:16010–16015, Dec 1997. doi: 10.1103/PhysRevB.56.16010. URL https://link.aps.org/doi/10.1103/PhysRevB.56.16010.

[65] John E. Sader and Suzanne P. Jarvis. Accurate formulas for interaction force and energy in frequency modulation force spectroscopy. *Applied Physics Letters*, 84(10):1801–1803, 03 2004. ISSN 0003-6951. doi: 10.1063/1.1667267. URL https://doi.org/10.1063/1.1667267.

[66] Megan Cowie. *Charge re-organization timescales and loss tangents at semiconductor surfaces measured by nc-AFM*. Phd thesis, McGill University, 2023. Available at https://escholarship.mcgill.ca/concern/theses/zs25xg239.

[67] Bert Voigtländer. *Scanning Probe Microscopy: Atomic Force Microscopy and Scanning Tunneling Microscopy*. NanoScience and Technology. Springer, Berlin, Heidelberg, 2015. ISBN 978-3-662-45239-4 978-3-662-45240-0. doi: 10.1007/978-3-662-45240-0. URL https://link.springer.com/10.1007/978-3-662-45240-0.

[68] Prokop Hapala, Georgy Kichin, Christian Wagner, F. Stefan Tautz, Ruslan Temirov, and Pavel Jelínek. Mechanism of high-resolution STM/AFM imaging with functionalized tips. *Physical Review B*, 90(8):085421, August 2014. doi: 10.1103/PhysRevB.90.085421. URL https://link.aps.org/doi/10.1103/PhysRevB.90.085421. Publisher: American Physical Society.

[69] Franz J. Giessibl. The qPlus sensor, a powerful core for the atomic force microscope. *Review of Scientific Instruments*, 90(1):011101, 01 2019. ISSN 0034-6748. doi: 10.1063/1.5052264. URL https://doi.org/10.1063/1.5052264.

[70] Franz J. Giessibl, Florian Pielmeier, Toyoaki Eguchi, Toshu An, and Yukio Hasegawa. Comparison of force sensors for atomic force microscopy based on quartz tuning forks and length-extensional resonators. *Phys. Rev. B*, 84:125409, Sep 2011. doi: 10.1103/PhysRevB.84.125409. URL https://link.aps.org/doi/10.1103/PhysRevB.84.125409.

[71] Franz J. Giessibl, Hartmut Bielefeldt, Stefan Hembacher, and Jochen Mannhart. Calculation of the optimal imaging parameters for frequency modulation atomic force microscopy. *Applied Surface Science*, 140(3):352–357, 1999. ISSN 0169-4332. doi: https://doi.org/10.1016/S0169-4332(98)00553-4. URL https://www.sciencedirect.com/science/article/pii/S0169433298005534.

[72] Nikolaj Moll, Leo Gross, Fabian Mohn, Alessandro Curioni, and Gerhard Meyer. The mechanisms underlying the enhanced resolution of atomic force microscopy with functionalized tips. *New Journal of Physics*, 12(12):125020, December 2010. ISSN 1367-2630. doi: 10.1088/1367-2630/12/12/125020. URL https://dx.doi.org/10.1088/1367-2630/12/12/125020.

[73] Leo Gross, Bruno Schuler, Fabian Mohn, Nikolaj Moll, Jascha Repp, and Gerhard Meyer. Atomic resolution on molecules with functionalized tips. *Noncontact Atomic Force Microscopy: Volume 3*, pages 223–246, 2015.

[74] Leo Gross, Fabian Mohn, Nikolaj Moll, Bruno Schuler, Alejandro Criado, Enrique Guitián, Diego Peña, André Gourdon, and Gerhard Meyer. Bond-order discrimination by atomic force microscopy. *Science*, 337(6100):1326–1329, 2012. doi: 10.1126/science.1225621. URL https://www.science.org/doi/abs/10.1126/science.1225621.

[75] Sören Zint, Daniel Ebeling, Tobias Schlöder, Sebastian Ahles, Doreen Mollenhauer, Hermann A. Wegner, and André Schirmeisen. Imaging Successive Intermediate States of the On-Surface Ullmann Reaction on Cu(111): Role of the Metal Coordination. *ACS Nano*, 11 (4):4183–4190, 2017. doi: 10.1021/acsnano.7b01109. URL https://doi.org/10.1021/acsnano.7b01109. PMID: 28346826.

[76] L. Bartels, G. Meyer, and K.-H. Rieder. Controlled vertical manipulation of single CO molecules with the scanning tunneling microscope: A route to chemical contrast. *Applied Physics Letters*, 71(2):213–215, July 1997. ISSN 0003-6951. doi: 10.1063/1.119503. URL https://pubs.aip.org/aip/apl/article/71/2/213/67819/Controlled-vertical-manipulation-of-single-CO. Publisher: AIP Publishing.

[77] Benjamin Alldritt, Fedor Urtev, Niko Oinonen, Markus Aapro, Juho Kannala, Peter Liljeroth, and Adam S. Foster. Automated tip functionalization via machine learning in scanning probe microscopy. *Computer Physics Communications*, 273:108258, April 2022. ISSN 0010-4655. doi: 10.1016/j.cpc.2021.108258. URL https://www.sciencedirect.com/science/article/pii/S0010465521003702.

[78] Edmund Taglauer. Surface cleaning using sputtering. *Applied Physics A*, 51:238–251, 1990.

[79] Oualid Ourdjini, Rémy Pawlak, Mathieu Abel, Sylvain Clair, Liang Chen, Nathalie Bergeon, Michel Sassi, Vincent Oison, Jean-Marc Debierre, Roland Coratger, and Louis Porte. Substrate-mediated ordering and defect analysis of a surface covalent organic framework. *Phys. Rev. B*, 84:125421, Sep 2011. doi: 10.1103/PhysRevB.84.125421. URL https://link.aps.org/doi/10.1103/PhysRevB.84.125421.

[80] Johanna Eichhorn, Damian Nieckarz, Oliver Ochs, Debabrata Samanta, Michael Schmittel, Pawel Jerzy Szabelski, and Markus Lackinger. On-Surface Ullmann Coupling: The Influence of Kinetic Reaction Parameters on the Morphology and Quality of Covalent Networks. *ACS Nano*, 8(8):7880–7889, August 2014. ISSN 1936-0851. doi: 10.1021/nn501567p. URL https://doi.org/10.1021/nn501567p. Publisher: American Chemical Society.

[81] Corbett C. Battaile. The kinetic monte carlo method: Foundation, implementation, and application. *Computer Methods in Applied Mechanics and Engineering*, 197(41):3386–3398, 2008. ISSN 0045-7825. doi: https://doi.org/10.1016/j.cma.2008.03.010. URL https://www.sciencedirect.com/science/article/pii/S0045782508001254. Recent Advances in Computational Study of Nanostructures.

[82] Mie Andersen, Chiara Panosetti, and Karsten Reuter. A practical guide to surface kinetic monte carlo simulations. *Frontiers in Chemistry*, 7, 2019. ISSN 2296-2646. doi: 10.3389/fchem.2019.00202. URL https://www.frontiersin.org/journals/chemistry/articles/10.3389/fchem.2019.00202.

[83] Stéfan van der Walt, Johannes L. Schönberger, Juan Nunez-Iglesias, François Boulogne, Joshua D. Warner, Neil Yager, Emmanuelle Gouillart, Tony Yu, and the scikit-image contributors. scikit-image: image processing in Python. *PeerJ*, 2:e453, 6 2014. ISSN 2167-8359. doi: 10.7717/peerj.453. URL https://doi.org/10.7717/peerj.453.

[84] Aric A. Hagberg, Daniel A. Schult, and Pieter J. Swart. Exploring network structure, dynamics, and function using networkx. In Gaël Varoquaux, Travis Vaught, and Jarrod Millman, editors, *Proceedings of the 7th Python in Science Conference*, pages 11 – 15, Pasadena, CA USA, 2008. URL http://conference.scipy.org/proceedings/SciPy2008/paper_2/.

[85] Aaditya Ramdas, Nicolas Garcia, and Marco Cuturi. On wasserstein two sample testing and related families of nonparametric tests, 2015. URL https://arxiv.org/abs/1509.02237.

[86] Pauli Virtanen, Ralf Gommers, Travis E. Oliphant, Matt Haberland, Tyler Reddy, David Cournapeau, Evgeni Burovski, Pearu Peterson, Warren Weckesser, Jonathan Bright, Stéfan J. van der Walt, Matthew Brett, Joshua Wilson, K. Jarrod Millman, Nikolay Mayorov, Andrew R. J. Nelson, Eric Jones, Robert Kern, Eric Larson, C J Carey, İlhan Polat, Yu Feng, Eric W. Moore, Jake VanderPlas, Denis Laxalde, Josef Perktold, Robert Cimrman, Ian Henriksen, E. A. Quintero, Charles R. Harris, Anne M. Archibald, Antônio H. Ribeiro, Fabian Pedregosa, Paul van Mulbregt, and SciPy 1.0 Contributors. SciPy 1.0: Fundamental Algorithms for Scientific Computing in Python. *Nature Methods*, 17:261–272, 2020. doi: 10.1038/s41592-019-0686-2.

[87] Zhenzhe Zhang, Dmitrii F. Perepichka, and Rustam Z. Khaliullin. Adatoms in the surface-confined ullmann coupling of phenyl groups. *The Journal of Physical Chemistry Letters*, 12

(45):11061–11069, 2021. doi: 10.1021/acs.jpclett.1c02914. URL https://doi.org/10.1021/acs.jpclett.1c02914. PMID: 34747624.

[88] Shigeki Kawai, Ali Sadeghi, Toshihiro Okamoto, Chikahiko Mitsui, Rémy Pawlak, Tobias Meier, Jun Takeya, Stefan Goedecker, and Ernst Meyer. Organometallic bonding in an ullmann-type on-surface chemical reaction studied by high-resolution atomic force microscopy. *Small*, 12(38):5303–5311, 2016. doi: https://doi.org/10.1002/smll.201601216. URL https://onlinelibrary.wiley.com/doi/abs/10.1002/smll.201601216.

[89] Jalmar Tschakert, Qigang Zhong, Daniel Martin-Jimenez, Jaime Carracedo-Cosme, Carlos Romero-Muñiz, Pascal Henkel, Tobias Schlöder, Sebastian Ahles, Doreen Mollenhauer, Hermann A. Wegner, Pablo Pou, Rubén Pérez, André Schirmeisen, and Daniel Ebeling. Surface-controlled reversal of the selectivity of halogen bonds. *Nature Comm.*, 11, 2020. doi: 10.1038/s41467-020-19379-4. URL https://doi.org/10.1038/s41467-020-19379-4.

[90] Stefan Grimme, Jens Antony, Stephan Ehrlich, and Helge Krieg. A consistent and accurate ab initio parametrization of density functional dispersion correction (dft-d) for the 94 elements h-pu. *The Journal of Chemical Physics*, 132(15):154104, 04 2010. ISSN 0021-9606. doi: 10.1063/1.3382344. URL https://doi.org/10.1063/1.3382344.

[91] MNG James and GJB Williams. On the bond distance between bromine and aromatic carbon atoms. *Acta Crystallographica Section B: Structural Crystallography and Crystal Chemistry*, 29(5):1172–1174, 1973.

[92] Hong-Tao Liu, Xiao-Gen Xiong, Phuong Diem Dau, Yi-Lei Wang, Dao-Ling Huang, Jun Li, and Lai-Sheng Wang. Probing the nature of gold–carbon bonding in gold–alkynyl complexes. *Nature Communications*, 4(1):2223, July 2013. ISSN 2041-1723. doi: 10.1038/ncomms3223. URL https://www.nature.com/articles/ncomms3223. Publisher: Nature Publishing Group.

[93] Prokop Hapala, Ruslan Temirov, F. Stefan Tautz, and Pavel Jelínek. Origin of High-Resolution IETS-STM Images of Organic Molecules with Functionalized Tips. *Physical Review Letters*, 113(22):226101, November 2014. doi: 10.1103/PhysRevLett.113.226101. URL https://link.aps.org/doi/10.1103/PhysRevLett.113.226101. Publisher: American Physical Society.

[94] Niko Oinonen, Aliaksandr V. Yakutovich, Aurelio Gallardo, Martin Ondráček, Prokop Hapala, and Ondřej Krejčí. Advancing scanning probe microscopy simulations: A decade of

development in probe-particle models. *Computer Physics Communications*, 305:109341, 2024. ISSN 0010-4655. doi: https://doi.org/10.1016/j.cpc.2024.109341. URL https://www.sciencedirect.com/science/article/pii/S0010465524002649.

[95] Percy Zahl and Yunlong Zhang. Guide for atomic force microscopy image analysis to discriminate heteroatoms in aromatic molecules [a guide for afm image analysis to discriminate heteroatoms in aromatic molecules]. *Energy and Fuels*, 33(6), 4 2019. doi: 10.1021/acs.energyfuels.9b00165.

[96] Lin Chen, Johanna Rosen, and Jonas Björk. A density functional benchmark for dehydrogenation and dehalogenation reactions on coinage metal surfaces. *ChemPhysChem*, n/a(n/a):e202400865, 2024. doi: https://doi.org/10.1002/cphc.202400865. URL https://chemistry-europe.onlinelibrary.wiley.com/doi/abs/10.1002/cphc.202400865.

[97] Igor A. Pašti and Slavko V. Mentus. Halogen adsorption on crystallographic (111) planes of pt, pd, cu and au, and on pd-monolayer catalyst surfaces: First-principles study. *Electrochimica Acta*, 55(6):1995–2003, 2010. ISSN 0013-4686. doi: https://doi.org/10.1016/j.electacta.2009.11.021. URL https://www.sciencedirect.com/science/article/pii/S0013468609013826.

[98] Hossein Taghinejad, Ali A. Eftekhar, and Ali Adibi. Lateral and vertical heterostructures in two-dimensional transition-metal dichalcogenides. *Opt. Mater. Express*, 9(4):1590–1607, Apr 2019. doi: 10.1364/OME.9.001590. URL https://opg.optica.org/ome/abstract.cfm?URI=ome-9-4-1590.

[99] José I. Urgel, Marco Di Giovannantonio, Guido Gandus, Qiang Chen, Xunshan Liu, Hironobu Hayashi, Pascal Ruffieux, Silvio Decurtins, Akimitsu Narita, Daniele Passerone, Hiroko Yamada, Shi-Xia Liu, Klaus Müllen, Carlo A. Pignedoli, and Roman Fasel. Overcoming steric hindrance in aryl-aryl homocoupling via on-surface copolymerization. *ChemPhysChem*, 20(18):2360–2366, 2019. doi: https://doi.org/10.1002/cphc.201900283. URL https://chemistry-europe.onlinelibrary.wiley.com/doi/abs/10.1002/cphc.201900283.

[100] Stuart Berg, Dominik Kutra, Thorben Kroeger, Christoph N. Straehle, Bernhard X. Kausler, Carsten Haubold, Martin Schiegg, Janez Ales, Thorsten Beier, Markus Rudy, Kemal Eren, Jaime I. Cervantes, Buote Xu, Fynn Beuttenmueller, Adrian Wolny, Chong Zhang, Ullrich Koethe, Fred A. Hamprecht, and Anna Kreshuk. ilastik: interactive machine learning for

(bio)image analysis. *Nature Methods*, 16(12):1226–1232, December 2019. ISSN 1548-7105. doi: 10.1038/s41592-019-0582-9. URL https://www.nature.com/articles/s41592-019-0582-9. Publisher: Nature Publishing Group.

[101] A. R. Sandy, S. G. J. Mochrie, D. M. Zehner, K. G. Huang, and Doon Gibbs. Structure and phases of the au(111) surface: X-ray-scattering measurements. *Phys. Rev. B*, 43:4667–4687, Feb 1991. doi: 10.1103/PhysRevB.43.4667. URL https://link.aps.org/doi/10.1103/PhysRevB.43.4667.

[102] Bert Voigtländer, Gerhard Meyer, and Nabil M. Amer. Epitaxial growth of thin magnetic cobalt films on au(111) studied by scanning tunneling microscopy. *Phys. Rev. B*, 44:10354–10357, Nov 1991. doi: 10.1103/PhysRevB.44.10354. URL https://link.aps.org/doi/10.1103/PhysRevB.44.10354.

[103] J.K. Gimzewski, S. Modesti, Ch. Gerber, and R.R. Schlittler. Observation of a new au (111) reconstruction at the interface of an adsorbed c60 overlayer. *Chemical Physics Letters*, 213 (3):401–406, 1993. ISSN 0009-2614. doi: https://doi.org/10.1016/0009-2614(93)85153-F. URL https://www.sciencedirect.com/science/article/pii/000926149385153F.

[104] Mario Kiel, Klaus Duncker, Christian Hagendorf, and Wolf Widdra. Molecular structure and chiral separation in α-sexithiophene ultrathin films on au(111): Low-energy electron diffraction and scanning tunneling microscopy. *Phys. Rev. B*, 75:195439, May 2007. doi: 10.1103/PhysRevB.75.195439. URL https://link.aps.org/doi/10.1103/PhysRevB.75.195439.

[105] AS Dakkouri and DM Kolb. *Reconstruction of gold surfaces*. Marcel Dekker: New York, 1999.